Exciton Dynamics in InP Quantum Dots

Fine Structure and Radiative Recombination Processes

Annalisa Brodu

Cover: Annalisa Brodu || Trusanne Bos
Lay-out and printing: Proefschriftmaken || Proefschriftmaken.nl
ISBN: 978-94-6380-468-4

Exciton Dynamics in InP Quantum Dots

Fine Structure and Radiative Recombination Processes

Exciton Dynamica in InP halfgeleider nanokristallen

Fijnstructuur en stralende recombinatie processen

(met een samenvatting in het nederlands)

Proefschrift

ter verkrijging van de graad van doctor aan de Universiteit Utrecht
op gezag van de rector magnificus, prof.dr. H.R.B.M. Kummeling,
ingevolge het besluit van het college voor promoties
in het openbaar te verdedigen op

maandag 16 september 2019 des middags te 4.15 uur

door

Annalisa Brodu
geboren te Iglesias, Italië

Promotoren
Prof. Dr. D.A.M. Vanmaekelbergh
Prof. Dr. Z. Hens

Copromotor
Dr. C. De Mello-Donega

This thesis was accomplished with financial support from the Marie Skłodowska Curie Action Innovative Training Network PHONSI- Nanophotonics by Nanocrystals and from the European Research Council under the European Union's Seventh Framework Programme (Horizon 2020)/ERC advanced grant agreement "First step" under grant number 692691.

Table of contents

Chapter 1

Introduction

Abstract

This chapter gives a general introduction on nanomaterials, with a particular focus on colloidal semiconductor nanocrystals, which have advantages in terms of easier and cheaper processability. Nanocrystals stand out for the high tunability of their properties, making them particularly functional and versatile, and therefore promising for several technological applications. This chapter presents a brief introduction to the optical properties of colloidal InP nanocrystals and an outline of this thesis.

1.1 Colloidal semiconductor nanocrystals

Nowadays, many electronic devices are based on nanotechnology. In fact, since the beginning of the computer era, the request to make technological components as small as possible has increased enormously. Devices need to be small, fast and cheap. For these reasons, there is a strong interest among the scientific community to push the size of materials to the smallest possible. Over the last few decades, nanoscale structures, and in particular semiconductor nanocrystals (NCs) have been studied extensively as a central topic in nanoscience and nanotechnology. Nanocrystals have one or more of the x,y,z dimensions in the order of a few nanometres. Semiconductor nanocrystals with all three dimensions sufficiently small to confine the electron (hole) wavefunctions are also known as quantum dots (QDs). Colloidal NCs are obtained by bottom-up wet chemical synthesis, using appropriate precursors in solution, and the processes are rather inexpensive. The nanocrystals are composed of an inorganic core, with organic ligands attached to the surface (figure 1.1a). The ligands result in stable dispersions of the nanocrystals in apolar solvents. Hence, different from epitaxially grown quantum dots, colloidal NCs are not in contact with a solid state substrate. Therefore, colloidal semiconductor nanocrystals are rather easy to make in large quantities, and in general their size and shape can be tailored by controlling the growth conditions.

The main characteristic that differentiates semiconductor nanocrystals from macroscopic crystals is the dependence of their electronic structure – and therefore their optical properties – on the nanocrystal size and shape. In fact, when their dimensions are comparable to the spatial extension of excitons (characteristic of the material), a quantum confinement effect occurs. It results in a variation of the electronic structure: from a band structure, typical for bulk materials, to a system with discrete electronic levels, where the energy gap between the unoccupied and occupied levels increases with a decrease of the nanocrystal size. This quantum confinement effect will be discussed in more detail in chapter 2. Therefore, by only varying the NCs dimensions, it is possible to significantly modify the light emission properties, without a change of the chemical composition (Figure 1.1b).

a)

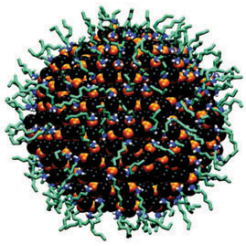

b)

Figure 1.1. a) Molecular simulation image of a colloidal CdSe quantum dot. Color legend: black, Se; orange, Cd; light blue, ligands. Reproduced from ref. 1. b) Suspensions of colloidal CdSe/CdS core/shell quantum dots of different sizes, from 1.7 nm (left) to 6 nm (right), under UV excitation. Reproduced from ref. 2.

The availability of these high-quality colloidal NCs opens up many possibilities in various applications such as light emitting diodes,[3–6] optoelectronic devices,[7–9] solar cells,[10,11] and biomedical imaging[12–14] (Figure 1.2). To date, Cd-chalcogenide NCs (*e.g.* CdSe based QDs) have been the workhorse in the field of nanomaterial optical devices. However, the implementation of QDs in commercial optoelectronic devices requires non-toxic materials. Therefore, due to the high toxicity of Cd, it is necessary to find substitute materials to replace these QDs.[7] InP nanocrystals are a good alternative and have been receiving attention due to their lower toxicity and large absorption cross-sections across a broad spectral range, high photoluminescence quantum yields, and size-tunability with photoluminescence emission in the visible range.[7,15–18] Nowadays, considerable control over the synthesis of high-quality InP QDs has been achieved. Bare InP QDs have low photoluminescence (PL) quantum yields (typically below 5%).[19–27] Therefore, to improve their efficiency shelling procedures with different semiconductor materials (*e.g.* ZnS or ZnSe) have been developed, allowing PL quantum yields as high as 60-70% to be obtained.[15,16] Besides, synthesis protocols using safer and inexpensive precursors have been designed, making InP-based QDs even more competitive.[15,18] However, despite the fundamental scientific relevance and importance in opto-electronics of InP-based QDs, a detailed understanding of their exciton structure and optical properties is still lacking. The exciton fine-structure of zinc blende QDs has been theoretically investigated by both effective-mass[28] and atomistic methods.[29,30] Experimentally, the temperature dependence of the PL decay times in InP/ZnS core/shell QDs has been studied,[31] as well as the blinking mechanism in single InP-based QDs[32,33] and the effect of the interfacial strain induced by heteroepitaxial shells on the optical properties of InP-based core/shell QDs.[34] Nevertheless, up to now, not much attention has been devoted to the exciton fine-structure and the radiative emission processes in InP-based QDs, which are the central topic of this thesis.

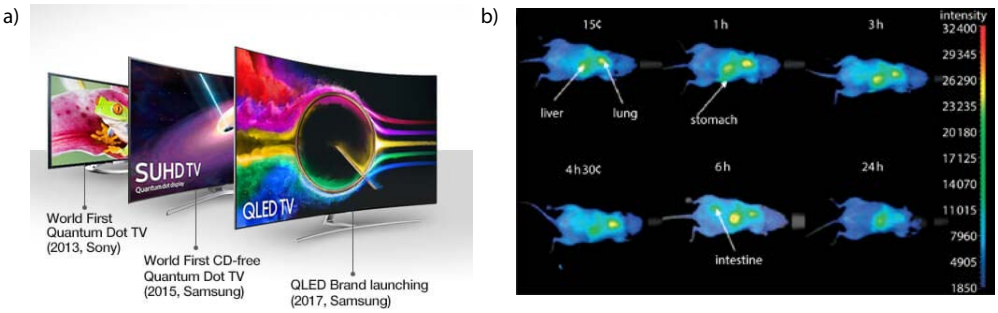

Figure 1.2. a) Quantum dot televisions, based on semiconductor nanocrystals, present in the market. Reproduced from ref. 35. b) Fluorescence images (excitation wavelength 633 nm) showing the temporal evolution of the bio-distribution of $CuInS_2$/ZnS nanocrystals injected intravenously into the tail of a healthy nude mouse. Reproduced from ref. 13.

1.2 Outline of the thesis

The research described in this thesis was driven both by fundamental interest in InP based QDs and by the promise that they hold in optical and opto-electronic applications. In order to impede non-radiative recombination, InP quantum dots have been foreseen with an inorganic shell of a higher band gap material, *e.g.* ZnS or ZnSe. The scope of this thesis is to investigate the exciton fine-structure and the exciton recombination processes in InP core\shell QDs.

Before results are presented in chapters 3-6, **chapter 2** will give a theoretical background of light-matter interaction in QDs, with a particular focus on the description of the quantum confinement effect, the resulting exciton structure of the lowest excited state (exciton fine-structure) and its interaction with an external magnetic field. The exciton localization in a core/shell QD system is also described, as well as the contribution of the different phonons in such systems.

Chapter 3 presents a study of the exciton fine structure of InP/ZnSe core/shell QDs with various InP core diameters. Time-resolved luminescence, Raman and circularly polarized fluorescence line-narrowing (FLN) spectroscopy at different temperatures and under magnetic fields up to 30 tesla were used. We demonstrated that the lowest exciton fine structure level is a dark state from which radiative decay to the ground state becomes possible by coupling to optical and confined acoustic phonons, both from the InP core and the ZnSe shell. We also observed that the highest-intensity FLN peak is an acoustic phonon replica rather than a zero-phonon line.

Chapter 4 reports a detailed study of the exciton dynamics and fine structure of InP/ZnS core/shell QDs, probed at the ensemble level. Through FLN and time-resolved luminescence spectroscopy and measurements of the degree of circular polarization – at 4 K and under magnetic fields up to 30 tesla – we found that the lowest exciton fine-structure level is also in this case a dark state that radiatively decays predominantly through phonon-assisted processes. Furthermore, we observe that mixing of this dark state with the nearest upper bright state in a magnetic field does not occur, and that the spin dynamics in InP QDs substantially deviates from that in II-VI QDs.

Chapter 5 presents a study of the exciton recombination dynamics in InP QDs with shells of various compositions: ZnS, ZnSe and (Zn,Cd)Se with different amounts of Cd (≤ 12%). Through the comparison of the phonon energies extracted from Raman spectra and the multiple emission features seen in fluorescence line narrowing (FLN) spectra, we studied the recombination dynamics from the lowest dark state, involving exciton-phonon coupling. Moreover, we found that there is an enhancement of the electron delocalization into the shell by increasing Cd content and this reinforces the exciton-phonon coupling via the Fröhlich interaction.

Chapter 6 provides a detailed model of the exciton fine structure of InP QDs with ZnSe shells with variable amounts of Cd (≤ 9%), which were added to reduce the heterointerfacial strain between core and shell. We use FLN spectroscopy at 4 K to reduce the spectral broadening in the QDs ensemble and magnetic fields from 0 to 30 T in order to induce a Zeeman splitting in the different types of spin states. We found that the different amounts of Cd (0 - 9%) incorporated in the ZnSe shell do not significantly influence the exciton fine-structure.

Finally, **Chapter 7** summarizes the main results achieved in this thesis with an English, Dutch and Italian summaries.

1.3 References

1 Donegá, C. D. M. Synthesis and Properties of Colloidal Heteronanocrystals. *Chem. Soc. Rev.* **2011**, *40*, 1512–1546.

2 Roduner, E. Size Matters: Why Nanomaterials Are Different. *Chem. Soc. Rev.* **2006**, *35*, 583–592.

3 Ippen, C.; Greco, T.; Wedel, A. InP/ZnSe/ZnS: A Novel Multishell System for InP Quantum Dots for Improved Luminescence Efficiency and Its Application in a Light-Emitting Device. *J. Inf. Disp.* **2012**, *13*, 91–95.

4 Wood, V.; Panzer, M. J.; Chen, J.; Bradley, M. S.; Halpert, J. E.; Bawendi, M. C.; Bulović, V. Inkjet-Printed Quantum Dot-Polymer Composites for Full-Color AC-Driven Displays. *Adv. Mater.* **2009**, *21*, 2151–2155.

5 Shirasaki, Y.; Supran, G. J.; Bawendi, M. G.; Bulović, V. Emergence of Colloidal Quantum-Dot Light-Emitting Technologies. *Nat. Photonics* **2013**, *7*, 13–23.

6 Lim, J.; Jun, S.; Jang, E.; Baik, H.; Kim, H.; Cho, J. Preparation of Highly Luminescent Nanocrystals and Their Application to Light-Emitting Diodes. *Adv. Mater.* **2007**, *19*, 1927–1932.

7 Grim, J. Q.; Manna, L.; Moreels, I. A Sustainable Future for Photonic Colloidal Nanocrystals. *Chem. Soc. Rev.* **2015**, *44*, 5897–5914.

8 Deng, Z.; Jeong, K. S.; Guyot-Sionnest, P. Colloidal Quantum Dots Intraband Photodetectors. *ACS Nano* **2014**, *8*, 11707–11714.

9 Foucher, C.; Guilhabert, B.; Laurand, N.; Dawson, M. D. Wavelength-Tunable Colloidal Quantum Dot Laser on Ultra-Thin Flexible Glass. *Appl. Phys. Lett.* **2014**, *104*, 1–5.

10 Kim, M. R.; Ma, D. Quantum-Dot-Based Solar Cells: Recent Advances, Strategies, and Challenges. *J. Phys. Chem. Lett.* **2015**, *6*, 85–99.

11 Taylor, R. A.; Ramasamy, K. Colloidal Quantum Dots Solar Cells. *SPR Nanosci.* **2017**, *4*, 142–168.

12 Zhou, J.; Liu, Y.; Tang, J.; Tang, W. Surface Ligands Engineering of Semiconductor Quantum Dots for Chemosensory and Biological Applications. *Mater. Today* **2017**, *20*, 360–376.

13 Lacroix, L.-M.; Delpech, F.; Nayral, C.; Lachaize, S.; Chaudret, B. New Generation of Magnetic and Luminescent Nanoparticles for in Vivo Real-Time Imaging. *Interface Focus* **2013**, *3*, 1–19.

14 Walling, M.; Novak, J.; Shepard, J. R. E. Quantum Dots for Live Cell and In Vivo Imaging. *Int. J. Mol. Sci.* **2009**, *10*, 441–491.

15 Tessier, M. D.; Dupont, D.; De Nolf, K.; De Roo, J.; Hens, Z. Economic and Size-Tunable Synthesis of InP/ZnE (E = S, Se) Colloidal Quantum Dots. *Chem. Mater.* **2015**, *27*, 4893–4898.

16 Pietra, F.; De Trizio, L.; Hoekstra, A. W.; Renaud, N.; Prato, M.; Grozema, F. C.; Baesjou, P. J.; Koole, R.; Manna, L.; Houtepen, A. J. Tuning the Lattice Parameter of InxZnyP for Highly Luminescent Lattice-Matched Core/Shell Quantum Dots. *ACS Nano* **2016**, *10*, 4754–4762.

17 Mićić, O. I.; Sprague, J.; Lu, Z.; Nozik, A. J. Highly Efficient Band-Edge Emission from InP Quantum Dots. *Appl. Phys. Lett.* **1996**, *68*, 3150–3152.

18 Dupont, D.; Tessier, M. D.; Smet, P. F.; Hens, Z. Indium Phosphide-Based Quantum Dots with Shell-Enhanced Absorption for Luminescent Down-Conversion. *Adv. Mater.* **2017**, *29*, 1700686.

19 Micic, O. I.; Curtis, C. J.; Jones, K. M.; Sprague, J. R.; Nozik, A. J. Synthesis and Characterization of InP Quantum Dots. *J. Phys. Chem.* **1994**, *98*, 4966–4969.

20 Micic, O. I.; Sprague, J. R.; Curtis, C. J.; Jones, K. M.; Machol, J. L.; Nozik, A. J.; Giessen, H.; Fluegel, B.; Mohs, G.; Peyghambarian, N. Synthesis and Characterization of InP, GaP, and GaInP2 Quantum Dots. *J. Phys. Chem.* **1995**, *99*, 7754–7759.

21 Mićić, O. I.; Ahrenkiel, S. P.; Nozik, A. J. Synthesis of Extremely Small InP Quantum Dots and Electronic Coupling in Their Disordered Solid Films. *Appl. Phys. Lett.* **2001**, *78*, 4022–4024.

22 Guzelian, A. A.; Katari, J. E. B.; Kadavanich, A. V.; Banin, U.; Hamad, K.; Juban, E.; Alivisatos, A. P.; Wolters, R. H.; Arnold, C. C.; Heath, J. R. Synthesis of Size-Selected, Surface-Passivated InP Nanocrystals. *J. Phys. Chem.* **1996**, *100*, 7212–7219.

23 Lucey, D. W.; MacRae, D. J.; Furis, M.; Sahoo, Y.; Cartwright, A. N.; Prasad, P. N. Monodispersed InP Quantum Dots Prepared by Colloidal Chemistry in a Noncoordinating Solvent. *Chem. Mater.* **2005**, *17*, 3754–3762.

24 Battaglia, D.; Peng, X. Formation of High Quality InP and InAs Nanocrystals in a Noncoordinating Solvent. *Nano Lett.* **2002**, *2*, 1027–1030.

25 Nozik, A. J.; Mićić, O. I. Colloidal Quantum Dots of III-V Semiconductors. *MRS Bull.* **1998**, *23*, 24–30.

26 Xie, R.; Battaglia, D.; Peng, X. Colloidal InP Nanocrystals as Efficient Emitters Covering Blue to Near-Infrared. *J. Am. Chem. Soc.* **2007**, *129*, 15432–15433.

27 Joung, S.; Yoon, S.; Han, C.-S.; Kim, Y.; Jeong, S. Facile Synthesis of Uniform Large-Sized InP Nanocrystal Quantum Dots Using Tris(Tert-Butyldimethylsilyl)Phosphine. *Nanoscale Res. Lett.* **2012**, *7*, 93.

28 Efros, A.; Rosen, M.; Kuno, M.; Nirmal, M.; Norris, D.; Bawendi, M. Band-Edge Exciton in Quantum Dots of Semiconductors with a Degenerate Valence Band: Dark and Bright Exciton States. *Phys. Rev. B* **1996**, *54*, 4843–4856.

29 Fu, H.; Zunger, A. InP Quantum Dots: Electronic Structure, Surface Effects, and the Redshifted Emission. *Phys. Rev. B* **1997**, *56*, 1496.

30 Fu, H.; Wang, L.-W.; Zunger, A. Excitonic Exchange Splitting in Bulk Semiconductors. *Phys. Rev. B* **1999**, *59*, 5568–5574.

31 Biadala, L.; Siebers, B.; Beyazit, Y.; Tessier, M. D.; Dupont, D.; Hens, Z.; Yakovlev, D. R.; Bayer, M. Band-Edge Exciton Fine Structure and Recombination Dynamics in InP/ZnS Colloidal Nanocrystals. *ACS Nano* **2016**, *10*, 3356–3364.

32 Kuno, M.; Fromm, D. P.; Gallagher, A.; Nesbitt, D. J.; Micic, O. I.; Nozik, A. J. Fluorescence Intermittency in Single InP Quantum Dots. *Nano Lett.* **2001**, *1*, 557–564.

33 Chandrasekaran, V.; Tessier, M. D.; Dupont, D.; Geiregat, P.; Hens, Z.; Brainis, E. Nearly Blinking-Free, High-Purity Single-Photon Emission by Colloidal InP/ZnSe Quantum Dots. *Nano Lett.* **2017**, *17*, 6104–6109.

34 Rafipoor, M.; Dupont, D.; Tornatzky, H.; Tessier, M. D.; Maultzsch, J.; Hens, Z.; Lange, H. Strain Engineering in InP/(Zn,Cd)Se Core/Shell Quantum Dots. *Chem. Mater.* **2018**, *30*, 4393–4400.

35 Https://Pid.Samsungdisplay.Com/En/Learning-Center/White-Papers/Evolution-of-Quantum-Dot-Technologies.

Chapter 2

Theoretical background

Abstract

Semiconductor nanocrystals hold promise for opto-electronic applications due to their bright emission and size-tunable electronic and optical properties, arising from quantum mechanical size-confinement effects. This thesis reports on the optical properties of InP core/shell nanocrystals, which show radiative exciton decay in the visible region. In this region, InP core/shell nanocrystals form a less toxic alternative for the well-studied family of Cd-chalcogenide nanocrystals. We will address the basic theoretical concepts needed to understand the experimental results presented in the next chapters. Using the effective mass approximation, we will describe the size- and shape-dependence of the ($1S_h$,$1S_e$) exciton fine-structure states and the optical transitions between these states and the ground state. This will be followed by a discussion on the interaction of these exciton states with an external magnetic field. Moreover, the optical characteristics of nanocrystals consisting of a core and an epitaxial shell will be discussed. The chapter ends with a brief discussion of the interaction between excitons and lattice vibrations – phonons - and the role of phonons in exciton decay to the ground state.

2.1 Semiconductor nanocrystals (quantum dots)

Semiconductor nanocrystals (NCs) have optical properties which depend not only on their chemical composition but also on their shape and size. In contrast, in bulk semiconductors, the fundamental energy band gap (which separates the empty conduction band from the filled valence band) is a fixed parameter, determined by the type of material. If a photon of energy equal to the band gap is absorbed, an electron is promoted from the valence to the conduction band, creating an electron-hole pair (ehp). If, in a bulk crystal, the electron and hole are bound by Coulomb attraction, the excited state is called an exciton. In nanocrystals, the electron and hole can, roughly speaking, always be considered as an exciton, since the electron and hole wavefunctions are both confined in the limited volume of the nanocrystal and thus overlap. This phenomenon is known as quantum confinement and explains the size-dependent emission spectrum, and the fact that semiconductor quantum dots have a number of discrete optical transitions.

An important length scale that estimates the degree of confinement is the exciton Bohr radius compared to the radius of the nanocrystal. The exciton Bohr radius is defined as:[1]

$$a_{exc} = \varepsilon \frac{m}{m^*} a_0 \tag{2.1}$$

where ε is the dielectric constant of the material, m the rest mass of the electron, m^* the reduced mass of the electron-hole pair and a_0 the Bohr radius of the hydrogen atom.

We focus on spherical nanocrystals. If their radius (R) is smaller than a_{exc}, strong confinement holds, and the nanocrystals are called 'quantum dots' (QDs).[2] For InP nanocrystals, the exciton Bohr radius is about 10 nm. The work described in this thesis deals with InP nanocrystals in the strong confinement regime.

2.2 Electronic structure of nanocrystals

2.2.1 Particle in a spherical potential well model

At an atomic level, the nanocrystalline material is structurally identical to a macroscopic crystal. For this reason, we start by considering a bulk material. According to Bloch's theorem, for a non-interacting electron system, the single-electron wave functions in an ideal and infinite crystal can be written as:

$$\Psi_{nk}(\vec{r}) = u_{nk}(\vec{r})\, e^{(i\vec{k}\cdot\vec{r})} \tag{2.2}$$

where u_{nk} is a function with the periodicity of the crystal lattice, n is the band index and $\vec{k}$ the wave vector. It is possible to describe the energies of these wave functions with a band diagram, where the energies are represented as a function of the wave vector $\vec{k}$. Considering the *effective mass approximation*, the electronic bands can be assumed as parabolic near the fundamental band gap, namely at k close to zero, around the top of the valence band and the bottom of the conduction band.

CdSe and InP semiconductors have a direct gap: the maximum of the valence and the minimum of the conduction band are located at $k = 0$ (called the Γ point) in the Brillouin zone. The *effective mass approximation*, allows to neglect the contribution of the atoms of the semiconductor lattice and to treat electrons and holes as free particles, but with a mass different from the rest electron and hole mass, *i.e. effective mass* (m_{eff}). The conduction band (E_k^c) and valence band (E_k^v) energies, are approximated to:[2]

$$E_k^c = \frac{\hbar^2 k^2}{2m_{eff}^c} + E_g \tag{2.3}$$

$$E_k^v = -\frac{\hbar^2 k^2}{2m_{eff}^v} \tag{2.4}$$

where E_g is the energy gap of the semiconductor material. The k-values are closely spaced and form a quasi-continuum. The effective mass determines the shape of the parabola, see Figure 2.1.

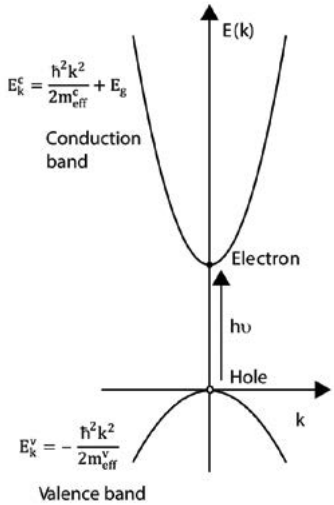

Figure 2.1. Diagram for a simple two-parabolic-band model of a direct-gap semiconductor. The k values are so closely spaced that they form a quasi-continuum. Adapted from ref. 2.

To determine the electronic levels in a nanocrystal we assume that the single-particle wavefunctions (electrons or holes) can be still written in terms of Bloch functions (Eq. 2.2) and that the concept of the effective mass is valid in quantum dots. This approximation is plausible since the diameter of the nanoparticle is ten or more times the crystal unit cell.

This model is called the *envelope function approximation*. The single particle wavefunctions can then be written as a linear combination of Bloch functions:

$$\Psi_p^n(\vec{r}) = \sum_k C_{nk} u_{nk}(\vec{r})\, e^{(i\vec{k}\cdot\vec{r})} \tag{2.5}$$

where C_{nk} are the expansion coefficients that allow to satisfy the boundary conditions related to the shape of the nanocrystal. If we assume that the u_{nk} function has a weak dependence on k, which can be neglected, the previous equation can be rewritten in the form:

$$\Psi_p^n(\vec{r}) = u_n(\vec{r}) \sum_k C_{nk}\, e^{(i\vec{k}\cdot\vec{r})} \tag{2.6}$$

Now we can define a function $f_p^n(\vec{r})$, named *envelope function* of the single particle, given by:

$$f_p^n(\vec{r}) = \sum_k C_{nk}\, e^{(i\vec{k}\cdot\vec{r})} \tag{2.7}$$

The eq. (2.6) then becomes:

$$\Psi_p^n(\vec{r}) = u_n(\vec{r})\, f_p^n(\vec{r}) \tag{2.8}$$

where the function $u_n(\vec{r})$ can be estimated by various analytical or numerical methods. The problem is therefore reduced to the determination of the *envelope function* $f_p^n(\vec{r})$, that for spherically shaped nanocrystals is described by the solutions of a particle inside a sphere of radius 'r' and with a potential barrier approximated as infinitely high:[2]

$$V(r) = \begin{cases} 0 & r < R \\ \infty & r > R \end{cases} \tag{2.9}$$

By solving the Schrödinger equation for this potential well, we obtain wave functions given by:

$$\Phi_{n,l,m}(r,\theta,\phi) = C\, j_l\left(k_{n,l} r\right) Y_l^m(\theta,\phi) \tag{2.10}$$

where C is a normalization constant,

$Y_l^m(\theta,\phi)$ a spherical harmonic,

$j_l\left(k_{n,l} r\right)$ the lth order spherical Bessel function

and

$$k_{n,l} = \frac{\alpha_{n,l}}{R} \tag{2.11}$$

with $\alpha_{n,1}$ the nth zero of the j_1 function.

The energies of the particles are given by:

$$E_{n,l} = \frac{\hbar^2 k_{n,l}^2}{2m_{eff}} = \frac{\hbar^2 \alpha_{n,l}^2}{2m_{eff}R^2} \tag{2.12}$$

We can see that, due to the symmetry of the problem, the eigenfunctions, given in equation 2.10 are in the form of atomic-like orbitals, characterized by quantum numbers n (1,2,3 ...), l (s, p, d, ...) and ml (–l, ..., l). Moreover, the energies (Eq. 2.12) are almost identical to the kinetic energies of the free particle, except for the wavevector $k_{n,l}$ which is now quantized due to the spherical boundary conditions. The number of allowed discrete k values in the x,y, and z directions in the first Brillouin zone is equal to the number of unit cells in that direction. We show the band diagram with some discrete electronic states according to Eq. (2.12) in figure 2.2, together with an allowed optical transition, resulting in an exciton.

So far, the Coulombic attraction between electron and hole has not been discussed. Obviously, this attraction is present also in a nanocrystal as the electrons and holes occupy the same space. In the strong confinement regime, the (kinetic) confinement energy of the electron (hole) scales with $1/R^2$ (Eq. 2.12), and it dominates on the Coulomb attraction, which scales as $1/R$. Usually, the Coulomb attraction energy gives only a small contribution to the total energy of the exciton.

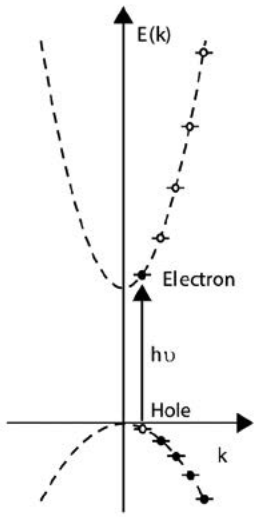

Figure 2.2. Energy-wave vector diagram for a semiconductor nanocrystal showing discrete electron and hole energy levels and an allowed optical transition. Adapted from ref. 2.

It is therefore possible to use the so-called *strong confinement approximation*, in which the electron and the hole can be treated independently, each of which described by a particle in a sphere, as described above. The Coulomb term (E_c) can then be added as correction energy to first order. The exciton wavefunction in a nanocrystal can therefore be written as:

$$\Psi_{ehp}(\vec{r}_e, \vec{r}_h) = \Psi_e^c(\overrightarrow{r_e})\Psi_h^v(\overrightarrow{r_h}) \tag{2.13}$$

where c stands for the conduction band and v for the valence band.

From Eq. 2.8 we find:

$$\Psi_{ehp}(\vec{r}) = u_c(\vec{r})\, f_e^c(\overrightarrow{r_e})u_v(\vec{r})\, f_h^v(\overrightarrow{r_h}) \tag{2.14}$$

Using eq. 2.10 we can explicitly write:

$$\Psi_{ehp}(\vec{r}) = C\left(u_c j_{L_e}\left(k_{n_e,L_e} r_e\right)Y_{L_e}^{m_e}(\theta,\phi)\right)\left(u_v j_{L_h}\left(k_{n_h,L_h} r_h\right)Y_h^{m_h}(\theta,\phi)\right) \tag{2.15}$$

Energies can be derived from eq. 2.12 and adding the Coulomb correction energy term $(E_c > 0)$ we find:

$$E_{ehp}(n_e L_e n_h L_h) = E_g + \frac{\hbar^2}{2R^2}\left\{\frac{\alpha_{n_e,L_e}^2}{m_{eff}^c} + \frac{\alpha_{n_h,L_h}^2}{m_{eff}^v}\right\} - E_c \tag{2.16}$$

whereby states are indicated by quantum numbers $n_e L_e n_h L_h$.

If we consider the fundamental state of the exciton, indicated as $1S_e 1S_h$, the Coulomb correction at the first order (E_c) is equal to $1.8e^2/\varepsilon R$ and for sufficiently small QDs can also be neglected. Furthermore considering the potential described by eq. 2.9, the first zero of the Bessel function at zero order $(\alpha_{1,0})$, for the electron and the hole, is equal to π.

The energy of the $1S_e 1S_h$ state can therefore be approximated to:

$$E_{ehp}(1S_e 1S_h) \approx E_g + \frac{\hbar^2\pi^2}{2m_{eh}R^2} \tag{2.17}$$

where $\frac{m_{eff}^c m_{eff}^v}{m_{eff}^v + m_{eff}^c} = m_{eh}$ is the effective reduced mass of the hole-electron pair.

This expression provides a first approximation for the size-dependence of the excitonic state $(1S_e 1S_h)$ in a QD. The discrete nature of the electron and hole energy levels and the size-dependent electron-hole separation energy is presented in Figure 2.3.

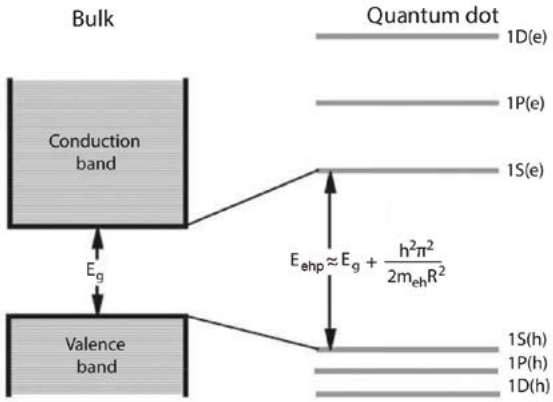

Figure 2.3. Comparison between the continuous valence and conduction bands separated by a fixed gap energy (E_g) in a 'bulk' compared to discrete states, atomic-like, with energy fixed by the radius in a quantum dot. Adapted from ref. 2.

2.2.2 Electronic band structures

The valence and conduction bands described in the 'particle in a spherical potential well model' are approximated by simple parabolic bands (Figure 2.1). However, real structures are typically much more complicated. For the semiconductor InP, which is the focus of this thesis, we will describe the band structure in more detail. Figure 2.4a and b show respectively the band structure of InP with a cubic zinc blende crystal structure and the corresponding Brillouin zone for this cubic structure. At Γ (centre zone at k = 0) the direct gap between the valence and conduction bands is clearly visible. Furthermore, it is noteworthy that the conduction band (which is derived from the s orbitals of the In atoms and therefore only doubly degenerate in Γ) can be well approximated by a parabola of appropriate curvature. This is not valid for the valence bands which originate from the p orbitals of P atoms, thus six-fold degenerate in Γ. The valence bands can be approximated by three different parabolas with distinct curvatures depending on the effective mass. These bands are characterized by their total angular momentum $\mathrm{J} = \mathrm{L}+\mathrm{S}$ where L is the orbital angular momentum and S the spin. The total angular momentum of the conduction band is $\mathrm{J_e} = 1/2$ ($\mathrm{L_e} = 0$, $\mathrm{S_e} = 1/2$) with z-projections $m_{\mathrm{J_e}} = \pm\, 1/2$. In the same way, the valence band has one state with total angular momentum $\mathrm{J_h} = 3/2$ and z-projections $m_{\mathrm{J_h}} = \pm\, 3/2$, commonly known as the heavy-hole (hh) sub-band, one with $\mathrm{J_h} = 3/2$ and z-projections $m_{\mathrm{J_h}} = \pm\, 1/2$, known as the light-hole (lh) sub-band and a third one with $\mathrm{J_h} = 1/2$ and $m_{\mathrm{J_h}} = \pm\, 1/2$, named the split-off (so) sub-band. The degeneracy of the valence bands at k = 0 is split by the spin-orbit interaction. This is an interaction of relativistic nature between the spin of the electron and the magnetic field generated by its orbital motion. This interaction separates the set of degenerate bands by reducing the energy of the low total angular momentum state $\mathrm{J_h} = 1/2$ (so), compared to the states with total high angular momentum $\mathrm{J_h} = 3/2$ $(\mathrm{hh}$ and $\mathrm{lh})$, as shown in figure 4c with the

spin-orbit coupling separation 'Δ'. The 'so' band thus becomes much lower in energy and can be left out of the argumentation below.

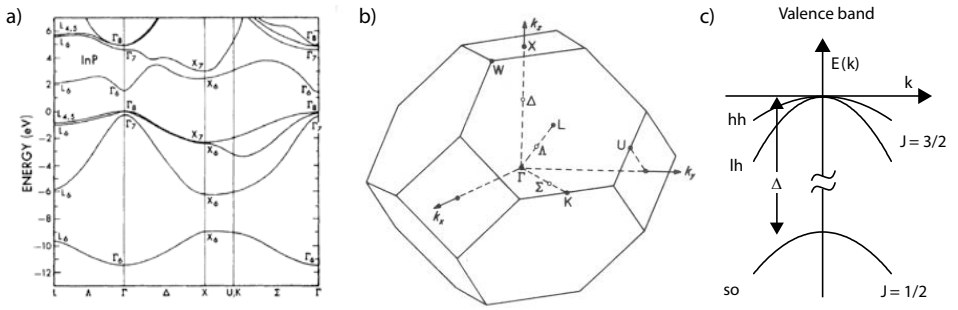

Figure 2.4. a) Band structure of the bulk zincblende InP structure. Reproduced from ref. 3. b) Corresponding Brillouin zone for the face centered cubic structure. Reproduced from ref. 4. c) Structure of the valence band near k = 0 for a diamond-like semiconductor. Adapted from ref. 2.

2.2.3 Exciton fine structure levels

According to the effective mass approximation model, the lowest nanocrystal exciton level $(1S_{h,\,3/2}\ 1S_e)$ is eight-fold degenerate, since it is constructed from the $(1S_e)$ level in the conduction band, which is two-fold degenerate (due to the electron spin projection) and the four-fold degenerate $(1S_{h,\,3/2})$ states in the two upper valence sub-bands (hh and lh). The eight-fold degeneracy of the lowest exciton level $(1S_{h,\,3/2}\ 1S_e)$ is lifted by the crystal field splitting due to anisotropy of the crystal structure (*e.g.* hexagonal lattice in wurtzite phase) or/and an asymmetry in the QD shape (*e.g.* non-spherical QDs), by which the hh and lh bands split also at k = 0 (left side of Figure 2.5). Furthermore, the eight-fold degeneracy is also lifted by the electron-hole exchange interaction, which splits the lowest exciton into a five-fold degenerate optically passive state and a 3-fold degenerate optically active state, with total angular momenta of $F = 2$ and $F = 1$ respectively, as illustrated in the right side of Figure 2.5. Combining the two effects mentioned above (electron-hole exchange interaction and crystal/shape asymmetry), the energy level structure develops into what is known as the *exciton fine structure* of QDs. This picture holds for wurtzite and cubic zinc blende nanocrystals, such as CdSe and InP. A schematic energy diagram of the exciton fine-structure is illustrated in the central panel of Figure 2.5. The fine structure consists of five distinct states, characterized by their exciton total angular momentum projection $(F_m = m_{J_h} + S_z)$ along the nanocrystal main symmetry-axis. In the electric dipole approximation, direct radiative recombination from the $F_m = \pm 2$ and $F_m = 0^L$ states is forbidden, thus the states are optically dark (dashed lines in Fig. 2.5), while radiative recombination from the $F_m = \pm 1^L$, $F_m = \pm 1^U$ and $F_m = \pm 0^U$ states is electric dipole allowed, thus the states are optically bright (solid lines in the central panel of Figure 2.5). The superscripts U and L denote respectively the upper and the lower levels with the same quantum number F_m but different energies.

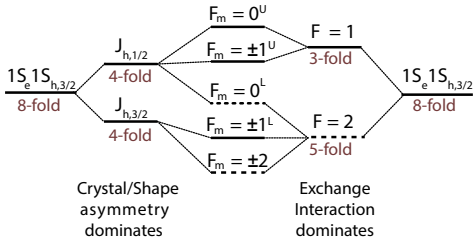

Figure 2.5. Energy level diagram of the exciton fine structure of a semiconductor quantum dot. The exciton energy levels are split by the crystal/shape asymmetry and the electron-hole exchange interaction. Adapted from ref. 2.

The level energies ($\varepsilon_{|F|}$) are determined by solving the secular equation $\det(\hat{E} - \varepsilon_{|F|})$ where $\hat{E}$ is the perturbation matrix that combines the asymmetry perturbations and the exchange interaction, taken between the exciton wave functions $\Psi_{\alpha,\ m}(r_e,r_h) = \psi_\alpha(r_e)\psi_m(r_h)$, where $\alpha=\uparrow(\downarrow)$ is the projection of the electron spin $S_z = +(-)1/2$, and m is the total angular momentum projection of the hole $(m_{Jh} = 3/2, 1/2, -1/2, -3/2)$.

The perturbation matrix derived by Efros et al., which allow a description of the energy levels as a function of the nanocrystal size and shape is given below:[2,5]

$(\alpha\ ,m)$	$\uparrow 3/2$	$\uparrow 1/2$	$\uparrow -1/2$	$\uparrow -3/2$	$\downarrow 3/2$	$\downarrow 1/2$	$\downarrow -1/2$	$\downarrow -3/2$
$\uparrow 3/2$	$-\frac{3\eta+\Delta}{2}$	0	0	0	0	0	0	0
$\uparrow 1/2$	0	$\frac{-\eta+\Delta}{2}$	0	0	$-i\sqrt{3}\eta$	0	0	0
$\uparrow -1/2$	0	0	$\frac{\eta+\Delta}{2}$	0	0	$-i2\eta$	0	0
$\uparrow -3/2$	0	0	0	$\frac{3\eta-\Delta}{2}$	0	0	$-i\sqrt{3}\eta$	0
$\downarrow 3/2$	0	$i\sqrt{3}\eta$	0	0	$\frac{3\eta-\Delta}{2}$	0	0	0
$\downarrow 1/2$	0	0	$i2\eta$	0	0	$\frac{\eta+\Delta}{2}$	0	0
$\downarrow -1/2$	0	0	0	$i\sqrt{3}\eta$	0	0	$\frac{-\eta+\Delta}{2}$	0
$\downarrow -3/2$	0	0	0	0	0	0	0	$-\frac{3\eta+\Delta}{2}$
$F_m = \alpha+m$	+2	$+1^U$	0^U	-1^L	$+1^L$	0^L	-1^U	-2

Here, η represents the exchange interaction term and is given by:

$$\eta = \left(\frac{a_{exc}}{a}\right)^3 \hbar\omega_{ST}\, \chi(\beta) \tag{2.18}$$

where a_{exc} is the exciton Bohr radius, a the effective radius, $\hbar\omega_{ST}$ the electron-hole exchange interaction splitting in bulk, and $\chi(\beta)$ is a dimensionless scaling function that depends only on the light to heavy hole effective mass ratio β.

The term Δ represents the sum of the internal crystal field and shape (ellipticity) splitting:

$$\begin{aligned}\Delta(a,\beta,\mu) &= \Delta_{crystal} + \Delta_{shape} \\ &= \Delta_{cf}\, v(\beta) + 2\mu u(\beta) E_{3/2}(\beta)\end{aligned} \tag{2.19}$$

where Δ_{cf} is the internal crystal field splitting for a hexagonal lattice in wurtzite phase (zero for a cubic lattice), $v(\beta)$ and $u(\beta)$ are dimensionless scaling factors depending on β, and $\mu=(c/b-1)$ is the ellipticity of the nanocrystal, which is determined by the ratio of the major (c) and the minor (b) axes, and $E_{3/2}$ is the $1S_{3/2}$ ground state hole energy for spherical nanocrystals of radius a.

With this model, the energy of each exciton fine structure F_m state can be calculated as a function of size and shape (ellipticity). Figure 2.6 presents examples of the exciton energy levels F_m as a function of QD radius in cubic phase zinc blende CdTe QDs with a spherical, oblate and prolate shape, respectively. The crystal shape asymmetry completely determines the relative order of the exciton fine structure states.

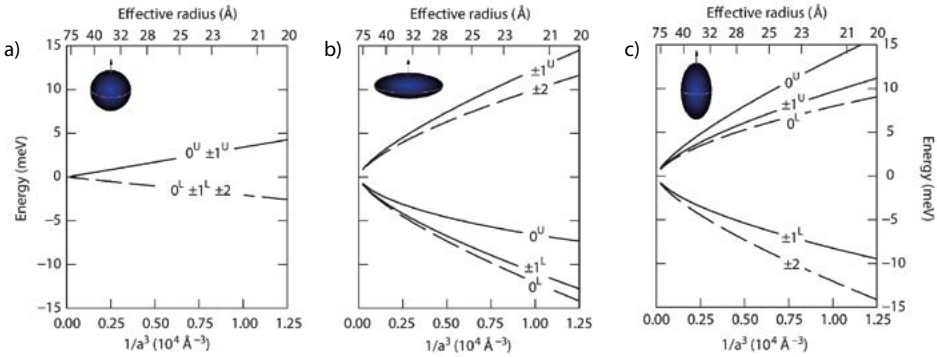

Figure 2.6. The size and shape dependence of the exciton fine structure in cubic phase CdTe quantum dots: a) in spherical QDs (ellipticity $\mu = 0$), b) oblate QDs ($\mu = 0.28$); c) prolate QDs ($\mu = 0.28$); Solid lines indicate optically active (bright) states and dashed lines passive (dark) states. Adapted from ref. 5.

2.2.4 Optical transition probabilities

The optical transition probabilities of the exciton states are strongly affected by the electron-hole exchange interaction. The exciton states with total angular momentum projection $F_m = \pm 2$ are optically passive because emitted or absorbed photons cannot have an angular momentum of ± 2. The probability of optical transition (excitation or radiative recombination) of an exciton state F_m is proportional to the square of the matrix element of the polarization vector of the emitted or absorbed light $\boldsymbol{e}$ and the electric dipole momentum operator $\hat{\boldsymbol{p}}$, between the F_m state and the final state:

$$P_{\boldsymbol{F_m}}^{\boldsymbol{U,L}} = \left|\left\langle 0 \middle| \boldsymbol{e}\hat{\boldsymbol{p}} \middle| \boldsymbol{\Psi}_{F_m}^{U,L} \right\rangle\right|^2 \tag{2.20}$$

For the $F_m = 0$ and $F_m \pm 1$ states this results in:

$$P_{\mathbf{0}}^{\boldsymbol{U,L}} = \left|\langle 0|\boldsymbol{e}\widehat{\boldsymbol{p}}|\boldsymbol{\Psi}_0^{U,L}\rangle\right|^{\mathbf{2}} = \frac{(1\pm1)^2}{3} KP^2 \cos^2(\theta) \tag{2.21}$$

$$P_{\mathbf{1}}^{\boldsymbol{U,L}} = \left|\langle 0|\boldsymbol{e}\widehat{\boldsymbol{p}}|\boldsymbol{\Psi}_1^{U,L}\rangle\right|^{\mathbf{2}} = \frac{1}{3}\left(\frac{2\sqrt{f^2+d}\pm f\pm\sqrt{3d}}{2\sqrt{f^2+d}}\right) KP^2 \sin^2(\theta) \tag{2.22}$$

In which P is the Kane inter-band matrix element, θ is the angle between the light polarization vector (emitted or absorbed photons) and the main symmetry axis of the crystal, and K is the square of the overlap integral.[6]

Equations (2.21) and (2.22) show that the excitation probabilities of the $F = 0^{\mathrm{U}}$ and $F = \pm 1^{\mathrm{U,L}}$ exciton states differ in their dependence on the angle θ. The $F = 0^{\mathrm{L}}$ state is always optically passive. If the QDs are aligned with the crystal main symmetry axis perpendicular to the excitation light direction, only the $F = 0^{\mathrm{U}}$ states will be excited. Whereas, when the QDs are aligned along the light propagation direction, only the $F = 1^{\mathrm{U,L}}$ states can absorb photons. Accordingly, in an ensemble of randomly oriented QDs, a polarized excitation resonant with one of these exciton states selectively excites suitably oriented crystals, leading to polarized luminescence.[2,5]

2.3 Perturbation in magnetic field

The effect of an external magnetic field **B** can be well described by the Zeeman Hamiltonian:

$$H_B = g\mu_B \boldsymbol{J}\cdot\boldsymbol{B} = g\mu_B \boldsymbol{J}\cdot\hat{\boldsymbol{z}}B \tag{2.23}$$

where g is the Landé gyromagnetic factor (g-factor), μ_B is the Bohr magneton ($\mu_B = 5.79 \times 10^{-2}\, meV\, T^{-1}$), and $\mathbf{J} = \mathbf{L} + \mathbf{S}$ is the total angular momentum with $\mathbf{L}$ the orbital angular momentum and $\mathbf{S}$ the intrinsic spin (angular) momentum and $\hat{\boldsymbol{z}}$ is the unit vector to represent the external magnetic field (**B**) direction. Hence, the external magnet field splits the momentum-degenerate state. The energy of each sublevel can be written as:

$$E_z = g\mu_B\, m_J B \tag{2.24}$$

where m_J represents the eigenvalues of the total angular momentum projection along the magnetic field direction $\hat{\boldsymbol{z}}$.

In semiconductor QDs, the exciton Zeeman splitting is the sum of the splitting of the electron and hole levels:[5]

$$H_B = \frac{1}{2} g_e\mu_B\, \boldsymbol{\sigma}\cdot\boldsymbol{B} - g_h\mu_B\, \boldsymbol{K}\cdot\boldsymbol{B} \tag{2.25}$$

where g_e and g_h are the g-factors for the electron and the hole, $\boldsymbol{\sigma}$ and $\mathbf{K}$ are Pauli matrices representing the electron and hole momenta. The perturbation matrix H_B, shown below, has been derived by Efros *et al*. for wurtzite nanocrystal and allows the description of the exciton energy levels in an external magnetic field:[5]

(α , m)	↑3/2	↑1/2	↑−1/2	↑−3/2	↓3/2	↓1/2	↓−1/2	↓−3/2
↑ 3/2	H_{11}	H_{12}	0	0	H_{51}	0	0	0
↑ 1/2	H_{21}	H_{22}	H_{23}	0	0	H_{51}	0	0
↑−1/2	0	H_{32}	H_{33}	H_{12}	0	0	H_{51}	0
↑−3/2	0	0	H_{21}	H_{44}	0	0	0	H_{51}
↓ 3/2	H_{51}	0	0	0	$-H_{44}$	H_{12}	0	0
↓ 1/2	0	H_{51}	0	0	H_{21}	$-H_{33}$	H_{23}	0
↓−1/2	0	0	H_{51}	0	0	H_{32}	$-H_{22}$	H_{12}
↓−3/2	0	0	0	H_{51}	0	0	H_{21}	$-H_{11}$
$F_m = \alpha + m$	+2	$+1^U$	0^U	-1^L	$+1^L$	0^L	-1^U	-2

where the matrix elements H_{ij} are given by:

$$H_{11} = \frac{\mu_B\,(g_e - 3g_h)B_z}{2} \qquad H_{12} = H_{21}^* = \frac{-i\sqrt{3}\mu_B\, g_h B_-}{2}$$

$$H_{22} = \frac{\mu_B\,(g_e - g_h)B_z}{2} \qquad H_{23} = H_{32}^* = \frac{-i\mu_B\, g_h B_-}{2}$$

$$H_{33} = \frac{\mu_B\,(g_e + g_h)B_z}{2} \qquad H_{15} = H_{51}^* = \frac{\mu_B\, g_h B_-}{2}$$

$$H_{44} = \frac{\mu_B\,(g_e + 3g_h)B_z}{2}$$

Where $B_Z = B\ cos\ \theta$ is the magnetic field projection along the hexagonal axis, θ is the angle between the magnetic field direction $(\hat{\boldsymbol{z}})$ and the hexagonal axis, and $B_\pm = B_x \pm iB_y$ are the field components perpendicular to the hexagonal axis. The symbol * denotes complex conjugates (*i.e.*, $B_+ = B_x + iB_y \rightarrow B_+^* = B_x - iB_y = B_-$). The perturbation matrix H_B shows that the B components perpendicular to the $(\hat{\boldsymbol{z}})$ direction (B_z), present in the off-diagonal terms of the matrix, mix the optically passive $F_m = +2$ $(F_m = -2)$ states with the optically active $F_m = +1^{L,U}(F_m = -1^{L,U})$ states, whereas the dark $F_m = 0^{L,U}$ states mix with both $F = \pm 1^{L,U}$ exciton levels.[5,7] Experimental examples of this magnetic field induced bright-dark mixing are shown in Figure 2.7.[8–10] Furthermore, the B component along the $\hat{\boldsymbol{z}}$ direction, in the diagonal terms of the matrix, leads to a Zeeman splitting of the $F_m = \pm 2$ and $F_m = \pm 1^{L,U}$ exciton states that are doubly-degenerate at zero field (see experimental results in chapters 3 and 6).[11,12] The combined effect of the Zeeman splitting and optical selection rules gives rise to circularly polarized photoluminescence, which can be detected if the detected photons are along the magnetic field direction $\hat{\boldsymbol{z}}$ (Faraday geometry).

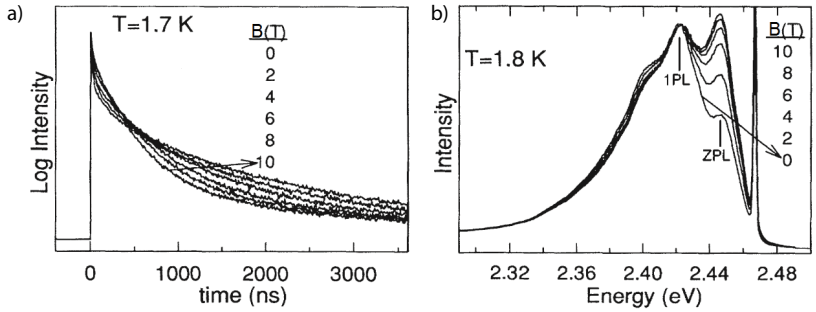

Figure 2.7. Experimental observation of the magnetic field induced bright-dark mixing in CdSe QDs. a) PL decay measurements recorded at the peak maximum of the luminescence (2.436 eV) with a pump energy of 2.736 eV. We observe a shortening of the luminescence lifetime with increasing magnetic field, due to the mixing of the lower forbidden exciton state with the upper bright state. b) Fluorescence line narrowing (FLN) spectra excited at the band edge (2.467 eV) and normalized to their one phonon line. A small amount of the excitation laser is included to mark the pump position. Experiments were carried out in the Faraday geometry ($\vec{B} \parallel \vec{k}$). The spectra show an increase of the intensity of the zero phonon line of the dark state with increasing field due to mixing with a bright state. Reproduced from ref. 7.

2.4 Excitons in heterostructured QDs

In order to passivate the QDs surface, thereby preventing non-radiative recombination and increasing photochemical stability, hetero-structured core-shell nanocrystals (HNC) were developed. HNCs consist of a core nanocrystal passivated by a shell of a different semiconductor which is heteroepitaxially grown on the core. The choice of the shell material is important for several reasons: (a) the shell material determines the lattice mismatch and strain at the core-shell interface,[13,14] and (b) the shell material determines the relative position of the core and shell valence and conduction band edges, thus the spatial extension of the exciton wavefunction over the core-shell.[15,16] Depending on the relative energy offsets, three limiting types of charge carrier localization regimes can be identified: type-I, type-I$^{1/2}$ (or quasi-type-II) and type-II.[15,16] These three regimes are schematically presented in Figure 2.8a. Examples of the energy band alignments of the semiconductors used in this thesis are shown in Figure 2.8b.

The Type-I regime is characterized by a core band gap that lies entirely within the shell band gap. In this regime, the electron and hole are primarily confined in the core of the heterostructure, resulting in a spatially direct exciton. Typical examples of these type of structures are CdSe/ZnS[17] or InP/ZnS[18] core/shell QDs.

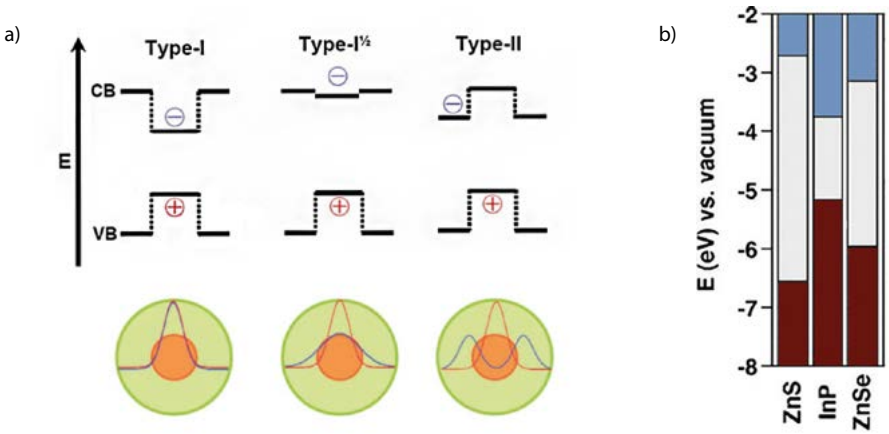

Figure 2.8. a) Schematic representation of three limiting types of charge carrier localization regimes (Type I, Type $I^{1/2}$ and Type II), in core/shell QDs. CB and VB stand for the conduction and valence band, respectively. The spatial extension of the electron (blue) and hole (red) wavefunction into the core/shell QDs is schematized in the bottom of the panel. Adapted from ref. 15. b) Energy band alignments of ZnS, InP, ZnSe bulk semiconductor materials. The gray spaces between the valence band bars (red) and the conduction band bars (blue) represent the band gap of the semiconductor materials. Adapted from ref. 19.

In Type-II HNCs, one charge carrier is confined in the core while the other is in the shell, resulting in a spatially indirect exciton. Typical examples of type-II systems are CdTe/CdSe,[20,21] CdSe/ZnTe[20] or CdS/ZnSe[22] core/shell QDs. In the type-$I^{1/2}$ system, one charge carrier wave function is delocalized over the entire core-shell structure while the other charge carrier is confined in the core. Typical examples of these type-$I^{1/2}$ systems are CdTe/CdSe[21] or InP/ZnSe[11] QDs.

In order to reduce the lattice mismatch and produce robust QDs with high photoluminescence quantum yield (PLQY), multi-shell,[23] graded[24] and alloyed[25] heterostructure QDs have been developed.

2.5 Phonon dispersion

Exciton-phonon interactions strongly influence the emission processes of semiconductor materials.[26] Each semiconductor crystal is characterized by distinctive phonon modes that might interfere with the exciton recombination dynamics. In Figure 2.9 we show as example the phonon dispersion curves and the relative phonon density of states (DOS) of bulk InP.[27] The phonon dispersion curves and DOS for ZnSe and ZnS (semiconductor materials used in the shell of the QDs studied in this thesis) can be found in Refs. (28 - 29).

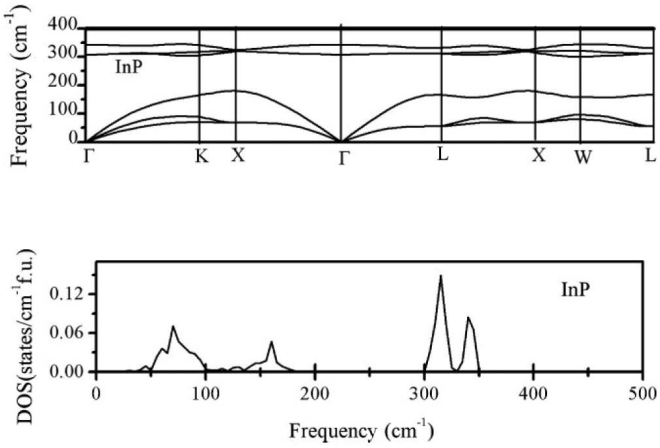

Figure 2.9. a) Phonon dispersion curves along high-symmetry axes in bulk InP at zero temperature and zero pressure. b) Phonon density of states (DOS) for the same material and conditions. Adapted from ref. 27.

Also for quantum confined NCs, exciton-phonon interactions are important in the exciton decay dynamics. My thesis will report on this in Chapters 3-5. Exciton-phonon coupling determines the absorption and emission linewidths, the luminescence Stokes shift, and enhance the decay of forbidden dark states to the ground state. Several aspects of the interaction between excitons and phonons are still under investigation. We will just mention some aspects, relevant for the following chapters. First, the coupling of excitons to confined acoustic-phonon modes in QDs, often discussed in literature with Lamb's theory,[30] in which the nanocrystal is treated as a stress-free isotropic hard sphere. The vibrations of such elastic isotropic spheres can be described in terms of torsional and spheroidal modes, characterized by the angular momentum l and the z-component m numbers, as a function of the nanocrystal radius, following the calculations of Takagahara.[31] Secondly, the coupling of the exciton to optical phonons can best be described by the Fröhlich model. In a polar semiconductor, an excited electron (or hole) together with its own self-induced polarization field behaves as a quasiparticle, known as a polaron. When the exciton decays to the ground state, the polarization energy of the surrounding medium is released through coupling with optical phonon modes that are released in the lattice.

2.6 References

1 Sergey V. Gaponenko. *Introduction to Nanophotonics*; Cambridge University Press: Cambridge, 2010.

2 Klimov, V. I. *Nanocrystal Quantum Dots*; 2nd ed.; CRC Press: Boca Raton, 2010.

3 Chelikowsky, J. R.; Cohen, M. L. Nonlocal Pseudopotential Calculations for the Elctronic Structure of Eleven. *Phys. Rev. B* **1976**, *14*, 556–582.

4 Koole, R. *Fundamentals and Applications of Semiconductor Nanocrystals. Ph.D. Thesis, Utrecht University, Utrecht*; 2008.

5 Efros, A.; Rosen, M.; Kuno, M.; Nirmal, M.; Norris, D.; Bawendi, M. Band-Edge Exciton in Quantum Dots of Semiconductors with a Degenerate Valence Band: Dark and Bright Exciton States. *Phys. Rev. B* **1996**, *54*, 4843–4856.

6 Efros, A. L. Luminescence Polarization of CdSe Microcrystals. *Phys. Rev. B* **1992**, *46*, 7448–7458.

7 Nirmal, M.; Norris, D. J.; Kuno, M.; Bawendi, M. G.; Efros, A. L.; Rosen, M. Observation of the "Dark Exciton" in CdSe Quantum Dots. *Phys. Rev. Lett.* **1995**, *75*, 3728–3731.

8 Biadala, L.; Louyer, Y.; Tamarat, P.; Lounis, B. Band-Edge Exciton Fine Structure of Single CdSe/ZnS Nanocrystals in External Magnetic Fields. *Phys. Rev. Lett.* **2010**, *105*, 1–4.

9 Louyer, Y.; Biadala, L.; Trebbia, J.-B.; Fernée, M. J.; Tamarat, P.; Lounis, B. Efficient Biexciton Emission in Elongated Cdse/Zns Nanocrystals. *Nano Lett.* **2011**, *11*, 4370–4375.

10 Wijnen, F. J. P.; Blokland, J. H.; Chin, P. T. K.; Christianen, P. C. M.; Maan, J. C. Competition between Zero-Phonon and Phonon-Assisted Luminescence in Colloidal CdSe Quantum Dots. *Phys. Rev. B* **2008**, *78*, 235318.

11 Brodu, A.; Ballottin, M. V.; Buhot, J.; Van Harten, E. J.; Dupont, D.; La Porta, A.; Prins, P. T.; Tessier, M. D.; Versteegh, M. A. M.; Zwiller, V.; *et al.* Exciton Fine Structure and Lattice Dynamics in InP/ZnSe Core/Shell Quantum Dots. *ACS Photonics* **2018**, *5*, 3353–3362.

12 Granados Del Águila, A.; Jha, B.; Pietra, F.; Groeneveld, E.; De Mello Donegá, C.; Maan, J. C.; Vanmaekelbergh, D.; Christianen, P. C. M. Observation of the Full Exciton and Phonon Fine Structure in CdSe/CdS Dot-in-Rod Heteronanocrystals. *ACS Nano* **2014**, *8*, 5921–5931.

13 Rafipoor, M.; Dupont, D.; Tornatzky, H.; Tessier, M. D.; Maultzsch, J.; Hens, Z.; Lange, H. Strain Engineering in InP/(Zn,Cd)Se Core/Shell Quantum Dots. *Chem. Mater.* **2018**, *30*, 4393–4400.

14 Pietra, F.; De Trizio, L.; Hoekstra, A. W.; Renaud, N.; Prato, M.; Grozema, F. C.; Baesjou, P. J.; Koole, R.; Manna, L.; Houtepen, A. J. Tuning the Lattice Parameter of In xZnyP for Highly Luminescent Lattice-Matched Core/Shell Quantum Dots. *ACS Nano* **2016**, *10*, 4754–4762.

15 Donegá, C. D. M. Synthesis and Properties of Colloidal Heteronanocrystals. *Chem. Soc. Rev.* **2011**, *40*, 1512–1546.

16 de Mello Donegá, C. *Nanoparticles*; de Mello Donegá, C., Ed.; Springer Berlin Heidelberg: Berlin, Heidelberg, 2014.

17 Dabbousi, B. O.; Rodriguez-Viejo, J.; Mikulec, F. V.; Heine, J. R.; Mattoussi, H.; Ober, R.; Jensen, K. F.; Bawendi, M. G. (CdSe)ZnS Core–Shell Quantum Dots: Synthesis and Characterization of a Size Series of Highly Luminescent Nanocrystallites. *J. Phys. Chem. B* **1997**, *101*, 9463–9475.

18 Tessier, M. D.; Dupont, D.; De Nolf, K.; De Roo, J.; Hens, Z. Economic and Size-Tunable Synthesis of InP/ZnE (E = S, Se) Colloidal Quantum Dots. *Chem. Mater.* **2015**, *27*, 4893–4898.

19 Norris, D. J.; Efros, A. L.; Erwin, S. C. Doped Nanocrystals. *Science.* **2008**, *319*, 1776–1779.

20 Kim, S.; Fisher, B.; Eisler, H.-J.; Bawendi, M. Type-II Quantum Dots: CdTe/CdSe(Core/Shell) and CdSe/ZnTe(Core/Shell) Heterostructures. *J. Am. Chem. Soc.* **2003**, *125*, 11466–11467.

21 de Mello Donegá, C. Formation of Nanoscale Spatially Indirect Excitons: Evolution of the Type-II Optical Character of CdTe/CdSe Heteronanocrystals. *Phys. Rev. B* **2010**, *81*, 165303.

22 Ivanov, S. A.; Piryatinski, A.; Nanda, J.; Tretiak, S.; Zavadil, K. R.; Wallace, W. O.; Werder, D.; Klimov, V. I. Type-II Core/Shell CdS/ZnSe Nanocrystals: Synthesis, Electronic Structures, and Spectroscopic Properties. *J. Am. Chem. Soc.* **2007**, *129*, 11708–11719.

23 Lim, J.; Jun, S.; Jang, E.; Baik, H.; Kim, H.; Cho, J. Preparation of Highly Luminescent Nanocrystals and Their Application to Light-Emitting Diodes. *Adv. Mater.* **2007**, *19*, 1927–1932.

24 Hadar, I.; Philbin, J. P.; Panfil, Y. E.; Neyshtadt, S.; Lieberman, I.; Eshet, H.; Lazar, S.; Rabani, E.; Banin, U. Semiconductor Seeded Nanorods with Graded Composition Exhibiting High Quantum-Yield, High Polarization, and Minimal Blinking. *Nano Lett.* **2017**, *17*, 2524–2531.

25 Bae, W. K.; Padilha, L. A.; Park, Y. S.; McDaniel, H.; Robel, I.; Pietryga, J. M.; Klimov, V. I. Controlled Alloying of the Core-Shell Interface in CdSe/CdS Quantum Dots for Suppression of Auger Recombination. *ACS Nano* **2013**, *7*, 3411–3419.

26 Gaponenko, S. V. *Optical Properties of Semiconductor Nanocrystals*; Cambridge University Press: Cambridge, 1998.

27 Hou, H. J.; Kong, F. J. Theoretical Investigation on the Structural, Dynamical, and Thermodynamic Properties of the Zinc-Blende InX (X = P, As, Sb). *Phys. status solidi* **2011**, *248*, 1399–1404.

28 Rössler, U. *New Data and Updates for Several Semiconductors with Chalcopyrite Structure, for Several II-VI Compounds and Diluted Magnetic IV-VI Compounds*; Springer: Berlin, Heidelberg, 2013.

29 Vagelatos, N.; Wehe, D.; King, J. S.; Vagelatos, N.; Wehe, D.; King, J. S. Phonon Dispersion and Phonon Densities of States for ZnS and ZnTe *. **1999**, *3613*.

30 Lamb, H. On the Vibrations of a Spherical Shell. *Proc. London Math. Soc.* **1882**, *13*, 187.

31 Takagahara, T. Electron—phonon Interactions in Semiconductor Nanocrystals. *J. Lumin.* **1996**, *70*, 129–143.

Chapter 3

Exciton fine structure and lattice dynamics in InP/ZnSe core/shell quantum dots

Based on:
Exciton Fine Structure and Lattice Dynamics in InP/ZnSe Core/Shell Quantum Dots.
Annalisa Brodu, Mariana V. Ballottin, Jonathan Buhot, Elleke J. van Harten, Dorian Dupont, Andrea La Porta, P. Tim Prins, Mickael D. Tessier, Marijn A. M. Versteegh, Val Zwiller, Sara Bals, Zeger Hens, Freddy T. Rabouw, Peter C. M. Christianen, Celso de Mello Donega, and Daniel Vanmaekelbergh.
ACS Photonics 2018, 5 (8), 3353–3362

Nanocrystalline InP quantum dots (QDs) hold promise for heavy-metal free opto-electronic applications due to their bright and size-tunable emission in the visible range. Photochemical stability and high photoluminescence (PL) quantum yield are obtained by a diversity of epitaxial shells around the InP core. To understand and optimize the emission line shapes, the exciton fine structure of InP core/shell QD systems needs to be investigated. Here, we study the exciton fine structure of InP/ZnSe core/shell QDs with core diameters ranging from 2.9 to 3.6 nm (PL peak from 2.3 to 1.95 eV at 4 K). PL decay measurements as a function of temperature in the 10 mK to 300 K range show that the lowest exciton fine structure state is a dark state, from which radiative recombination is assisted by coupling to confined acoustic phonons with energies ranging from 4 to 7 meV, depending on the core diameter. Circularly polarized fluorescence line-narrowing (FLN) spectroscopy at 4 K under high magnetic fields (up to 30 T) demonstrates that radiative recombination from the dark $\mathrm{F} = \pm 2$ state involves acoustic and optical phonons, both from the InP core and the ZnSe shell. Our data indicate that the highest-intensity FLN peak is an acoustic phonon replica rather than a zero-phonon line, implying that the energy separation observed between the $\mathrm{F} = \pm 1$ state and the highest-intensity peak in the FLN spectra (6 to 16 meV, depending on the InP core size) is larger than the splitting between the dark and bright fine structure exciton states.

Abstract

3.1 Introduction

After nearly three decades of research, colloidal nanocrystalline quantum dots (QDs), especially from the Cd-chalcogenide and Pb-chalcogenide families, have reached a high level of maturity. Core/shell QDs that are based on a CdSe core and a variety of shells are already applied in LEDs for monitors and TV screens.[1–5] However, there is a strong desire in society to replace these systems by Cd-free QDs that, ideally, should show the same performance. In the visible spectral range for which CdSe QDs are the most famous, InP QDs form one of the most promising heavy-metal free alternatives. The optical properties, though, are not yet optimal for opto-electrical applications. First of all, bare InP cores have a low PL quantum efficiency.[6–14] To solve this problem, shells of ZnS, ZnSe, and (Zn,Cd)Se have been developed for InP-based core/shell systems with promising photoluminescence (PL) quantum efficiencies up to 70%.[13–21] Secondly, optical absorption and luminescence spectroscopy showed that InP QDs have a broader PL peak than their CdSe analogues.[21–23] The emission linewidth of an ensemble of InP QDs is mostly related to inhomogeneous broadening,[24,25] but also to the exciton fine structure that fractionates the eightfold degenerate $1S_h1S_e$ exciton into several states and to the phonon contribution. Finally, InP QDs also show a considerable global Stokes shift (in the order of 100–300 meV)[10–13,19–21,26–32] between the absorption peak related to the band-edge exciton ($1S_h1S_e$) and the corresponding PL peak of QD ensembles. Although the global Stokes shift in other QD systems (PbS, CdSe, CdTe) has been shown to be largely determined by inter-QD energy transfer within the ensemble and the size dependence of the oscillator strengths,[33,34] the nature of the global Stokes shift of InP QDs is as yet unclear, and may be (partially) related to the exciton fine structure.

Both the synthesis of InP QDs from inexpensive precursors[21] and the characterization of the opto-electronic properties are currently under rapid development. However, up to now, not much attention has been devoted to the exciton fine structure of InP QDs, despite its fundamental scientific relevance and importance in InP-based opto-electronics. Theoretically, the exciton fine structure of zinc blende QDs has been investigated on the basis of effective-mass[35] and atomistic theories.[36,37] The exciton fine structure is determined by a combination of the electron-hole exchange, the crystal field splitting, and the possible shape anisotropy of the nanocrystals (*e.g.* prolate or oblate). For prolate-shaped zinc blende nanocrystals, the fine structure consists of five levels where the magnitude of the energy splitting between the levels increases fast with decreasing size, reaching tens of meV for sufficiently small QDs (on the order of 3 nm diameter).[35,38] The lowest-energy state has a total angular momentum projection along the nanocrystal axis $F = +2$ or -2, which means that its optical generation from the ground state and radiative decay back to the ground state are forbidden within the electric-dipole approximation (*i.e.*, it is a "dark" state). The next higher-energy state has $F = +1$ or -1, and thus there is an allowed electric-dipole optical transition between this state and the ground state (*i.e.*, it is a "bright" state). Furthermore, in the core/shell geometry, which in the end will be the geometry of practical importance, asymmetric strain induced by the shell heteroepitaxy[15,39] may also affect the fine structure energy levels.[40] Experimentally, the fine structure of InP/ZnS core/shell QD systems has only been studied by time-resolved PL spectroscopy.[41] It was found

that there were two bright states above the dark state, and that the energy separation between the dark $F = \pm 2$ state and the lowest bright $F = \pm 1$ state was in the 5–10 meV range, increasing with decreasing InP core size. The latter effect is directly related to the size-dependence of the electron–hole exchange energy.[35,36]

Here, we present a thorough study of the exciton fine structure of InP/ZnSe core/shell QD systems. We focus on thick ZnSe shells because they lead to QDs with high photochemical stability and high photoluminescence quantum yields. These systems were synthesized using inexpensive precursors and their production is amenable to upscaling.[21] The QDs, with InP core size ranging from 3.6 to 2.9 nm, emit in the visible range (1.8–2.3 eV) with a PL quantum yield around 40%. We study their exciton fine structure with several techniques. PL decay at varying temperatures reveals an energy separation between the dark $F = \pm 2$ state and a higher-energy brighter state of about 4–7 meV, depending on the core diameter, with the energy difference increasing with decreasing core size. The Raman spectra of the InP/ZnSe core/shell QDs show longitudinal-optical (LO) and transverse-optical (TO) phonons from both the InP core and the ZnSe shell. These phonon modes are involved in the radiative recombination of the dark $F = \pm 2$ exciton state, as we show using fluorescence line-narrowing (FLN) spectroscopy at 4 K under high magnetic fields (up to 30 T) and circularly polarized excitation and detection. In fact, our results indicate that the most intense FLN peak is an acoustic phonon replica rather than a zero-phonon line. This implies that the energy separation observed between the $F = \pm 1$ state and the highest-intensity peak in the FLN spectra (6–16 meV, depending on the InP core size) is larger than the splitting between the dark and bright fine structure exciton states.

3.2 Results and discussion

3.2.1 Structural and chemical characterization

The InP/ZnSe core/shell QDs were synthesized as described in reference 21. Most of the results discussed below were obtained on three samples with different InP core diameters (sample 1 with 2.9 nm, sample 2 with 3.1 nm, and sample 3 with 3.6 nm mean core diameter). Four other InP/ZnSe QD samples (referred to as samples 4–7) with different core diameters and a sample of bare InP QDs (referred to in the remainder of this chapter as "core-only") were used for complementary measurements. The core-only QDs were passivated with Cd-oleate to improve their chemical stability and thereby prevent surface oxidation. The core sizes were estimated from the lowest-energy exciton peak position in the absorption and emission spectra (see below for a discussion of the optical spectra).[42] Individual core/shell QDs were structurally characterized by High Angle Annular Dark Field Scanning Transmission Electron Microscopy (HAADF-STEM) and Energy Dispersive X-Ray Spectroscopy (EDX), as shown in Figure 3.1. The InP/ZnSe core/shell QDs are fairly monodisperse in size and shape. The zinc blende ZnSe shell grows around the InP core yielding a truncated tetrahedral shape of 3–4 nm edge length. The EDX maps confirm that In and P form the core, and Zn and Se the shell. However, alloying of the core/shell interface cannot be excluded. Chemical-element analysis yields an estimated elemental ratio of In:P:Zn:Se=3:4:49:44 (Figure 3.1c,d).

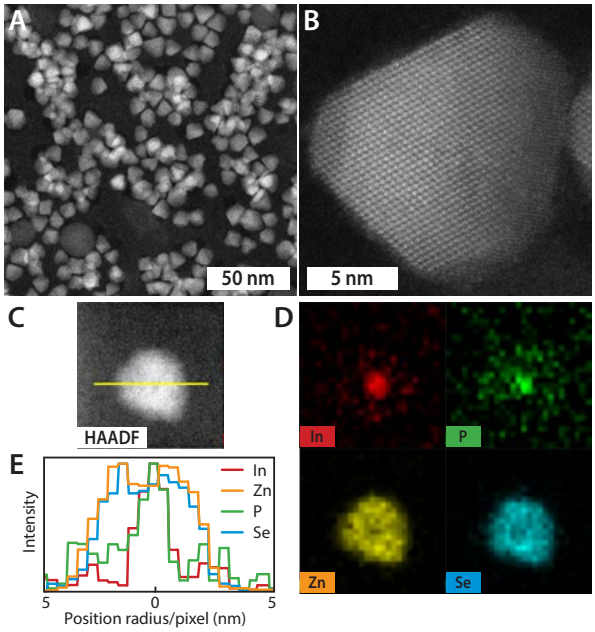

Figure 3.1. Chemical and structural characterization of InP/ZnSe core/shell QDs. a) and b) HAADF-STEM images of a InP/ZnSe core/shell QDs, with an average InP core diameter of 2.9 nm and a total core/shell diameter of 9.6 ± 1.1 nm (mean ± standard deviation), at (a) low and (b) high magnification. The high magnification depicts the ZnSe crystal along the [110] direction. c) and d) HAADF-STEM image of a single InP/ZnSe QD and corresponding EDX maps providing evidence for an InP core diameter of approximately 3 nm and a ZnSe shell of 3–4 nm. e) Elemental line scan along the yellow line through the InP/ZnSe QD shown in panel c. The core/shell structure of the QD is clearly resolved, since In and P are present primarily in the center of the nanocrystal, while Zn and Se are distributed throughout the QD. The diffuse and weaker background signal of P is ascribed to trioctylphosphine (TOP), which acts as a ligand. Measurements performed at the Electron Microscopy for Materials Research group (EMAT - University of Antwerp), by A. La Porta.

3.2.2 Basic optical characterization

The samples were characterized by their absorption and PL spectra (Appendix, Figures A3.1 and A3.2). The absorption spectrum at room temperature of sample 1 shows a defined peak at 2.18 eV due to the $1S_h$–$1S_e$ transition. The $1S_h$–$1S_e$ PL peak is red-shifted by 120 meV with respect to the $1S_h$–$1S_e$ absorption transition and has a full width at half maximum of 170 meV. The PL peak of our InP-based QDs is considerably broader than for instance that of CdSe QDs emitting in the same spectral region (100 meV at the ensemble level).[23,43] The PL peak of sample 1 (Appendix, Figure A3.1b) shows a considerable redshift when the temperature is increased from 4 K (peak maximum at 2.14 eV) to room temperature (peak maximum at 2.06 eV), due to expansion of the crystal lattice with increasing temperature.[44] Figure A3.1c shows the PL spectra for the three samples investigated in this work with a redshift of the $1S_h$–$1S_e$ exciton transition with increasing InP core size due to reduced quantum confinement. We

have measured the fine structure of the $1S_h$–$1S_e$ exciton for the three different core sizes. In the following, we will show the results obtained with the smallest core size (sample 1), of which the structural characterization was shown in Figure 3.1. Additional data for the other core sizes will be provided in the Appendix (Figures A3.2 – A3.11).

3.2.3 Study of the exciton fine structure by PL decay measurements at variable T

Previous studies on the PL decay dynamics of the $1S_h1S_e$ exciton in InP QDs showed that the PL decay becomes faster with increasing temperature.[41] This thermally activated PL decay reflects the presence of a lowest-energy dark state that dominates radiative decay at low temperatures, and a higher-energy brighter state that is thermally populated at elevated temperatures. To better understand the energy level structure involved in this thermally activated PL we performed a detailed study of the PL decay dynamics of the three InP/ZnSe core/shell QDs as a function of the temperature.

Figure 3.2a shows the PL decay transients for sample 1 (the full data set of the PL decay can be found in the Appendix, Figures A3.2–A3.5). At low temperatures (<10 K), the decay is bi-exponential with a slower lifetime component that becomes considerably faster with increasing temperature (from 190 ns at T≤ 9 K to ~30 ns at 300 K, Fig. 3.2b). Similar results are obtained for the larger core diameters (Figure A3.2). We propose here that the long lifetime component in our measurements reflects radiative recombination from a thermal equilibrium between a thermally activated brighter state $|d,1\rangle$ and the lowest dark state $|d\rangle$. In this model the initial fast lifetime component (at $t < 10$ ns) of the biexponential PL decay is ascribed to emission from higher-energy levels shortly after the laser pulse and prior to thermalization. The decay rate of the system at thermal equilibrium Γ_{tot} as a function of temperature is given by:

$$\Gamma_{tot} = \frac{1}{\tau_{tot}} = \frac{1}{\tau_D}\left(\frac{1}{1+e^{[+\Delta E_T/k_B T]}}\right) + \frac{1}{\tau_A}\left(\frac{1}{1+e^{[-\Delta E_T/k_B T]}}\right) \quad (3.1)$$

where k_B is the Boltzmann constant, ΔE_T is the energy difference between the dark state $|d\rangle$ and the brighter state $|d,1\rangle$ and τ_D and τ_A are the lifetimes of the lower-energy dark and the higher-energy 'brighter' state, respectively (see inset Figure 3.2b).

Figure 3.2b shows the evolution of the long lifetime component as a function of temperature. From 10 mK to 8 K (Figure A3.5) the lifetime stays constant (similar behavior in samples 2 and 3; Figures A3.3–A3.5). The lifetime becomes gradually shorter as the temperature is increased above 8 K until a plateau is reached at around 100 K (Figure 3.2b). The results were fitted with Eq. (3.1), with ΔE_T, τ_D and τ_A as fitting parameters (red line in Figure 3.2b, see Methods section below for details on the fitting procedure). The results are well described by Eq. (3.1), yielding an energy difference ΔE_T between the optically active state $|d,1\rangle$ and the dark state $|d\rangle$ of 5.5 meV. The PL decay dynamics of the samples 2 and 3 are also well described by Eq. (3.1), with energy separations between the dark and thermally activated 'brighter' state of respectively 4.9 and 4.3 meV (Appendix, Figure A3.4). These energies are slightly smaller than the 5–7 meV found in ref. 41 for InP/ZnS of similar core size.

This analysis was repeated with four extra samples with different core sizes (samples 4–7). The results clearly show that the energy difference ΔE_T between the $|d\rangle$ and $|d,1\rangle$ excited levels increases with decreasing QD size (Appendix, Figure A3.6). The energy separation ΔE_T between the $|d\rangle$ and $|d,1\rangle$ levels obtained from the temperature dependence (*T*-dependence) of the PL decays and the microscopic nature of these levels will be discussed in more detail in the final section of this chapter.

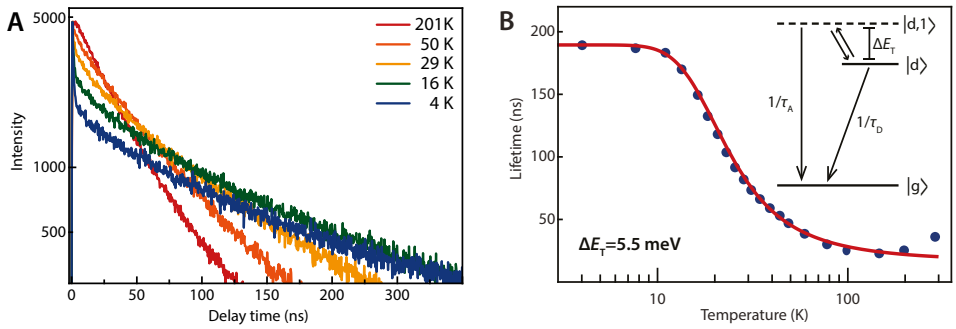

Figure 3.2. Thermally activated PL decay at zero magnetic field for the InP/ZnSe core/shell QDs (Sample 1). a) PL decay measured at the PL peak maximum (which depends on temperature; see Figure A3.1b), at various temperatures from 4 K (blue) to 200 K (dark red). b) A plot of the lifetime of the long component of the decay curves *versus* the temperature. The fitting (red line) is based on the thermal-occupation model (Eq. 3.1) with a thermal activation energy ΔE_T between the dark state $|d\rangle$ and an optically active state $|d,1\rangle$ of 5.5 meV. Inset: Schematic representation of the three-level scheme, with the dark state and thermally activated state with a higher oscillator strength.

3.2.4 Fluorescence Line-Narrowing spectroscopy

We performed size-selective spectroscopy using Fluorescence Line-Narrowing (FLN) experiments at 4 K to reduce the inhomogeneous line broadening of the observed nanocrystals. Using monochromatic laser light with photon energy matching the low-energy side of the lowest-energy absorption peak, a small sub-ensemble of the sample, with a certain core size, is excited. The optical transition is from the ground state to a fine structure state of the $1S_e1S_h$ exciton with high oscillator strength, thus necessarily the bright $F = \pm 1$ state. By applying an external high magnetic field between 0 and 30 T, it is possible to induce a sizable Zeeman splitting of spin-degenerate states, that, combined with circularly polarized excitation, allows us to predominantly excite either the $F = -1$ or $+1$ states and therefore to resolve unambiguously the nature of the states.

Figure 3.3 presents the results obtained for excitation with σ^+ circularly polarized light, predominantly exciting the upper $F = +1$ state (marked in red in the scheme shown in Figure 3.3), and detection of the σ^- circularly polarized emission. Figure 3.3a shows the FLN spectra, excited at 590 nm (2.1 eV). The FLN spectra are referenced to the energy of the laser excitation, or in other words, the bright $F = +1$ state is set at energy zero. At 0 T, three intense peaks are resolved, red-shifted with respect to this reference: the first at –11 meV, the second at –34 meV, and the third at –49 meV. Upon applying the magnetic field, the three peaks gradually shift to lower energies with respect to the reference. Interestingly, the magnitude of the shift is the same for all three peaks (*viz.*, 3 meV at 30 T), which implies that they are due to optical transitions from the same $F = -2$ state (Figure 3.3c). We conclude that these three peaks differ in terms of coupling to different phonons. This assignment is corroborated by our Raman spectroscopic study presented below (section Raman spectroscopy).

In essence, the temperature dependence of the exciton PL decay time and the magnetic field dependence of both the FLN and the degree of circular polarization (DCP) of the PL (Appendix, Figure A3.7) are similar to those of CdSe QDs[35,45–47] that have a $F = \pm 2$ ground state, which indicates that the InP/ZnSe QDs studied here also have a $F = \pm 2$ ground state.

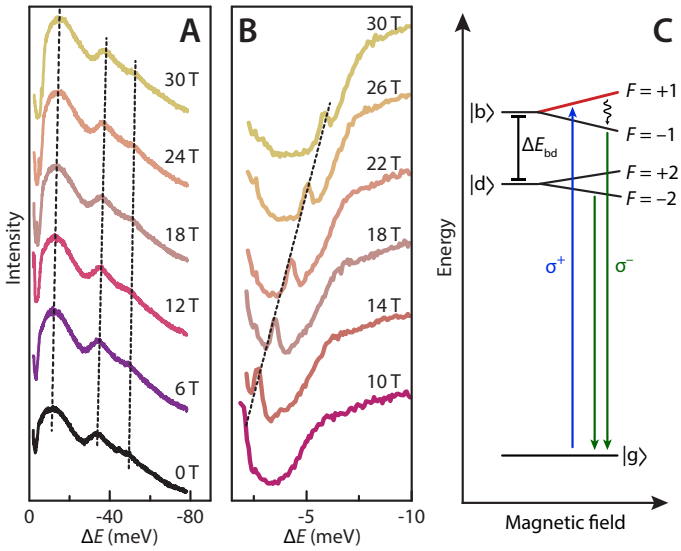

Figure 3.3. Fluorescence line-narrowing (FLN) spectroscopy at 4 K upon excitation of the bright $F = +1$ state with σ^+ light of 2.1 eV. a) FLN spectra showing the σ^- emission at variable magnetic fields. The excited state at 2.1 eV (the excitation laser energy) is taken as reference and set to 0 meV. The highest-intensity peak is related to emission from the dark state coupled to an acoustic phonon, the lower-energy peaks are related to optical phonon replicas. b) Zoom-in of the spectra at small ΔE, showing σ^- emission from the $F = -1$ bright state, shifting to lower energy due to the Zeeman effect (panel c). All spectra are vertically shifted for clarity. c) Energy level scheme showing the bright $F = +1$ state (marked in red) that is excited (blue arrow), and the σ^- emissions from the bright $F = -1$ and dark $F = -2$ states (green arrows). The phonon states are omitted for clarity.

A second feature becomes evident from 10 T and up: a sharp optical transition that originates from zero ΔE shifts rapidly to lower energies with respect to the $F = +1$ state (the reference) with increasing field (Figure 3.3b). This optical transition must reflect emission from the bright $F = -1$ state (as has been observed for CdSe QDs),[45,46] shifting to lower energy with respect to the reference because of the Zeeman splitting, $\Delta E = g\mu_B \mathbf{J} \cdot \mathbf{B}$, where g is the Landé gyromagnetic factor (g-factor), μ_B is the Bohr magneton ($\mu_B = 5.79\times10^{-2}$ meV T^{-1}) and $\mathbf{J} = \mathbf{L} + \mathbf{S}$ is the total angular momentum with $\mathbf{L}$ the orbital angular momentum and $\mathbf{S}$ the intrinsic spin (angular) momentum. From this linear Zeeman splitting, we deduce a Landé gyromagnetic factor g = 3.48 for the $F = \pm1$ state. Similar results are obtained for the other two samples (Appendix, Figure A3.8–A3.10).

To understand the linewidths of the bright and dark exciton emission in our FLN measurements, we note that the bright exciton emission in our FLN measurements in magnetic fields is shifted with respect to excitation due to the Zeeman effect. The splitting energy is only dependent on the g-factor, which is not strongly dependent on QD size (see Figures A3.8–A3.10). The bright exciton FLN peak is therefore sharp. The dark exciton, on the other hand, emits by coupling to acoustic phonons, as we will show in more detail below. The acoustic phonon energy depends on QD size. The FLN peak from the dark exciton is therefore inhomogeneously broadened.

Figure 3.4 presents the results obtained for excitation of the bright state with σ^- circularly polarized light, and detection of the σ^+ circularly polarized emission. In this case, the $F = -1$ level is predominantly excited and it will therefore be the reference state in the spectra (marked in red in scheme of Figure 3.4b). In Figure 3.4a, again three broad peaks are observed. Note that in this configuration, with increasing magnetic field, the Zeeman splitting between the $F = +1$ state to the $F = -1$ cannot be observed since with this polarization the $F = +1$ state cannot be excited. Instead, the first intense peak (–11 meV at 0 T) shows the presence of two components, one at almost constant energy with respect to the reference ($F = -1$ state) and a second smaller component (a shoulder of the highest-energy peak, emphasized in Figure 3.4a with the black arrow in the 30 T spectrum) shifting to higher energy with increasing magnetic field. This smaller component is related to the relaxation (after the photo-excitation into the optically bright $F = -1$ state) and the subsequent recombination from the dark $F = +2$ state, that occurs prior to the total relaxation of the system to the lowest $F = -2$ state. The component at constant ΔE is instead related to the recombination from the lowest-energy dark level $F = -2$. This level only emits purely σ^- polarized light for QDs with their anisotropic axis parallel to the field, whereas QDs aligned perpendicularly to the field emit unpolarized light.[47] As a result, within an ensemble of randomly oriented QDs the $F = -2$ levels also partly emit σ^+-polarized light. This explains why the integrated emission intensity in this experiment (detecting σ^+ polarized light; Figure 3.4) is lower by a factor 2 than when detecting σ^- polarized light (Figure 3.3).

In Figure 3.4a it is also evident that the second (34 meV at 0 T) and the third peak (49 meV at 0 T) become broader with increasing magnetic field, following the same trend as the highest-energy peak. We conclude again that the three peaks are emissions from the same exciton fine structure states ($F = \pm 2$) but involving coupling to different phonons. We will provide evidence below that the highest-intensity peak is in fact an acoustic phonon replica originating from the coupling of the dark exciton state with a confined acoustic phonon mode.

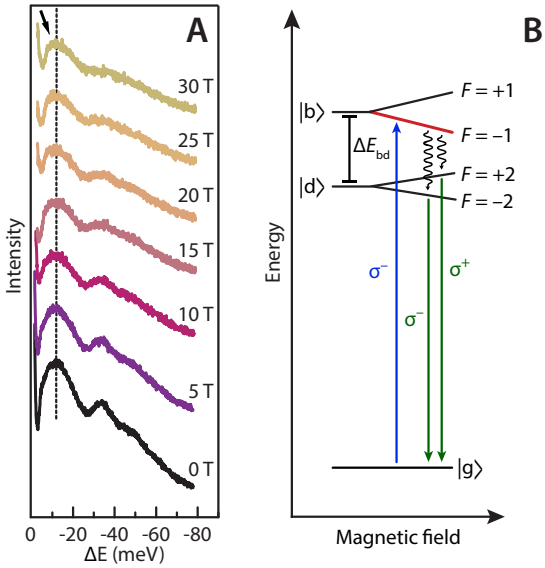

Figure 3.4. Fluorescence line-narrowing (FLN) spectroscopy at 4 K upon excitation of the bright $F = -1$ state with σ^- light of 2.1 eV. a) FLN spectra showing the σ^+ emission peaks at variable magnetic field. The state at 2.1 eV (the excitation laser energy) is taken as reference and set to 0 meV. The main peak (marked by the dashed line) is due to emission from the $F = \pm 2$ state coupled to an acoustic phonon, the other two peaks are related to optical phonon replicas. b) Energy level scheme showing the bright $F = -1$ state (marked in red) that is excited (blue arrow) and the emissions from the dark $F = \pm 2$ states (green arrows).

3.2.5 Raman spectroscopy

In order to study the phonon modes involved in the FLN process we carried out Raman scattering measurements on both InP/ZnSe QDs (sample 1) and core-only InP QDs of comparable size. Figure 3.5a presents the Raman spectra of both InP/ZnSe and core-only InP QD samples. For both samples, the sharp peak at approximately 520 cm^{-1} originates from the crystalline silicon substrate.[48] The Raman spectrum of the core-only InP QDs (in blue) shows two well-defined peaks at 311 cm^{-1} and 342 cm^{-1} (fitting in Figure 3.5b), which can be assigned to the transverse-optical (TO) and longitudinal-optical (LO) phonon modes of InP, as reported for bulk InP[49] and InP core-only QDs.[50]

In the Raman spectrum of the InP/ZnSe core/shell QDs (in red), we identify directly the LO and TO phonon modes of the InP lattice (315–380 cm^{-1}), which are shifted to higher energy due to the compressive strain imposed by the ZnSe heteroepitaxial shell (the lattice parameter of zinc-blende ZnSe is smaller than that of InP, *viz*., 5.668 and 5.869 Å, respectively). A second intense group of peaks is found between 190 and 260 cm^{-1}. These peaks are present only in the Raman spectrum of the InP/ZnSe core/shell QDs, we therefore assign them to ZnSe phonons. According to the literature, two of these peaks are the LO and TO phonon modes of bulk ZnSe[51]. This multiple-peak structure around 220 cm^{-1} in the ZnSe Raman spectrum might originate from a splitting of the LO and TO modes due to the strain. Double Raman processes of the InP and ZnSe phonons are also visible at higher energy in the Raman spectra (>400 cm^{-1}).

The zoom-in of the first two groups of peaks of the InP cores and InP core/shell QDs (respectively Figure 3.5b and Figure 3.5c) highlights the complex shape of the Raman peaks, rather broad likely due to the complexity of the QDs. Indeed defects in the crystal structure of InP and ZnSe can introduce perturbations in the system, resulting in a back-folding of the dispersion curve towards Γ and a concomitant increase of the density of phonon states.[52] The broadening can also be enhanced by double-phonon processes, more likely around 100 cm^{-1} in ZnSe and 100–200 cm^{-1} in InP due to the high density of the states at these energies at the edge of the Brillouin zone.[49,51,53] Another contribution to broadening of the Raman peaks is a distribution of phonon energies in the QD ensemble. Indeed, phonon energies can be influenced by interfacial strain and possible alloying in the InP–ZnSe core/shell heterointerface and also by the shape[54] and size[50] of the QDs.

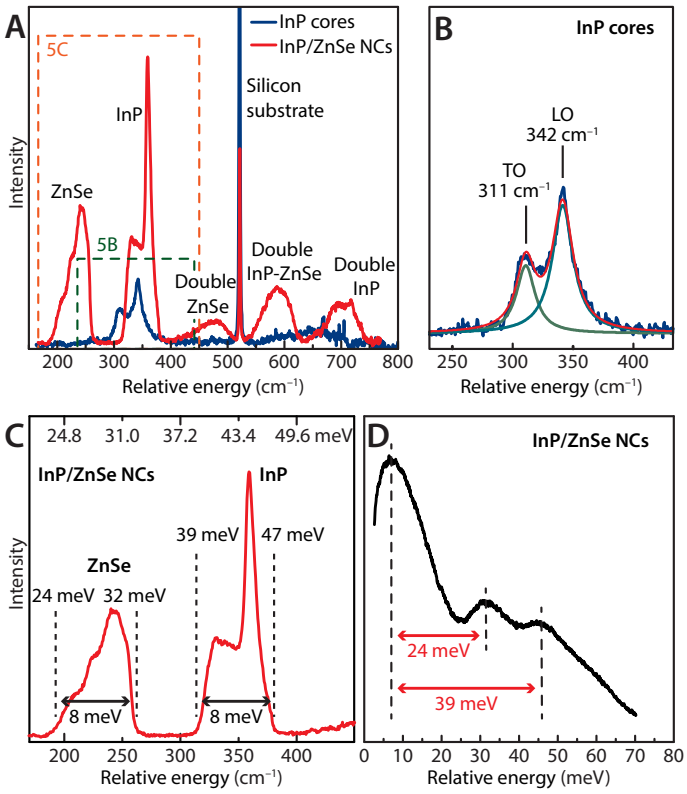

Figure 3.5. Raman and FLN spectra recorded at 4 K for InP cores and InP core/shell QDs with a mean core diameter of 2.9 nm. a) Raman spectra, obtained with a 488 nm laser line, of InP QDs (blue) and InP/ZnSe core/shell QDs (red). The peaks in the 315–380 cm^{-1} range are assigned to the LO and TO phonon modes of the InP QDs and the InP core in the InP/ZnSe core/shell QDs. The group of peaks around 190–260 cm^{-1} is assigned to the ZnSe phonon modes. Two of them are LO and TO modes. b) Lorentzian fits of the LO and TO phonons of the InP QDs. c) Zoom-in of the first two Raman peaks related to the ZnSe and InP optical phonons of the InP/ZnSe core/shell QDs sample. The dashed lines indicate energies that are relevant for comparison with the FLN spectra. d) FLN spectrum of the same InP/ZnSe core/shell QDs sample.

3.2.6 Role of the phonons in the radiative recombination of excitons in InP QDs

In Figure 3.6, we compare the energy splittings obtained from the T-dependent PL decay measurements (see also Figure 3.2) with those obtained from the FLN spectra. The former experiments provide a thermal activation energy ΔE_T, which is plotted in Figure 3.6a as a function of the PL peak emission energy. The latter experiments give the energy difference ΔE_{FLN} between the excitation energy (*i.e.*, the position of the bright $F = \pm 1$ state) and the highest-intensity peak in the FLN spectra, which we plot also as a function of the FLN peak emission energy. ΔE_{FLN} would correspond to the dark–bright splitting ΔE_{bd} under the assumption that the highest-intensity FLN peak is a zero-phonon line. However, we will show below that this assumption is inconsistent with our observations and that this transition is in fact an acoustic phonon replica.

The energy splitting ΔE_{FLN} from FLN measurements decreases from 16 to 6 meV with decreasing absolute peak emission energy, hence with increasing size of the InP core. The energy separation ΔE_T obtained from the T-dependent decay measurements also decreases with increasing size of the InP core, but over a much smaller range from 7 to 4 meV. This remarked difference implies that these two energy scales have different origins, which will be discussed in detail below. The energy ΔE_T is ascribed to coupling of the dark state $|d\rangle$ with thermally activated confined acoustic phonon modes (state $|d,1\rangle$).[55] We calculated the energy of the confined acoustic phonon modes as a function of the InP QD radius using Lamb theory,[56,57] and found an agreement with our experimental ΔE_T values (Appendix, Figure A3.11). This is in line with recent work on other QDs (CdSe, CdTe, PbSe, InAs,[55,58] ZnSe[59] and CdTe/CdSe core/shell heteronanocrystals[60]). We note that acoustic phonon replicas have also been directly observed recently in the FLN spectra of self-assembled, vertically aligned arrays of CdSe/CdS dot-in-rod nanorods.[61] Nevertheless, the mechanism behind the acoustic phonon-mediated brightening of the dark exciton state is not yet well-understood. A possible mechanism is that the deformation potential arising from coherent confined acoustic phonon modes elastically distorts the nanocrystals, resulting in a transient mixing between bright and dark states, which enhances the radiative recombination rates.[59,60,62,63]

To understand the nature of the ΔE_{FLN} splitting, it is necessary to consider the phonon modes available in the InP/ZnSe core/shell QDs studied here and their role in promoting optical transitions. Figures 3.5c and 3.5d above show that the phonon modes of the ZnSe shell (24–32 meV) and InP core (39–47 meV), observed in the Raman spectra, nearly agree with the phonon energies obtained from the phonon replicas observed in FLN spectra (respectively 24 meV and 39 meV, mean value). Clearly, the phonon energies observed in the FLN spectra are slightly smaller (by 3–4 meV) than the mean value of the peaks in the Raman spectra. We explain these small energy differences in terms of the confined acoustic phonon modes observed also in the T-dependent PL decay. The complete process involved in the radiative recombination monitored in the FLN spectra (Figure 3.5d) can be understood assuming an energy scheme as shown in Figure 3.6b. The scheme is composed of a ground state $|g\rangle$ and the two lowest excited states: a lowest-energy dark state $|d\rangle$ with projection of total angular momentum $F = \pm 2$, followed by a higher-energy bright state $|b\rangle$ with projection of total angular momentum $F = \pm 1$. Several phonon modes involved in the transitions are also represented in the scheme: ZnSe optical phonons (centered at 27 meV), InP optical phonons (centered at 42 meV), and confined acoustic phonon modes of the QDs having an estimated energy of 4–7 meV, depending on the core diameter.

In our FLN experiment, the resonant excitation brings the QDs in the bright state $|b\rangle$ with $F = \pm 1$. Since the experiment is performed at 4 K (equivalent to 0.3 meV) the recombination of excitons that have decayed to the dark state $F = \pm 2$ should take place only from this dark state. All possible recombination processes are labeled in Figure 3.6b with the dark-red numbers. Transition (1) from the dark state is formally forbidden within the effective mass and the electric-dipole approximations,[35] but can be activated by coupling with phonon modes. Transition (2) corresponds to a transition assisted by coupling to a confined acoustic phonon mode (*i.e.*, an acoustic phonon replica), which appears as the highest-

intensity line in the FLN spectra. This interpretation implies that ΔE_{FLN} corresponds to ΔE_{bd} plus the energy of the acoustic phonon mode that is coupled to the dark $F = \pm 2$ state. We assume that this phonon mode is the same responsible for the thermal activation involved in the temperature *T*-dependence of the PL decay dynamics. The difference between the two processes is that the acoustic phonon replica observed in the FLN spectra is due to a Stokes process in which a phonon is created, while the *T*-dependence of the PL decay is due to an anti-Stokes process, in which phonons are annihilated.

The first allowed transition (2) occurs at an energy of $-\Delta E_T$ with respect to the energy of the dark $F = \pm 2$ state. Other possible transitions involve the excitation of optical phonons, either as a single-phonon process or with additional coupling to confined acoustic phonon modes: transition (3) and (4) involve ZnSe optical modes, while (5) and (6) involve InP optical modes. The transitions (3) and (4) occur at energies $-\Delta E_{ZnSe}$ and $-(\Delta E_{ZnSe} + \Delta E_T)$, while (5) and (6) occur at $-\Delta E_{InP}$ and $-(\Delta E_{InP} + \Delta E_T)$ (where ΔE_{ZnSe} and ΔE_{InP} are the optical-phonon energies in ZnSe and InP). Transitions (3) and (4) are separated by only ΔE_T, so they appear in the FLN experiment as a single broad peak with center energy $-(\Delta E_{ZnSe} + \Delta E_T/2)$ with respect to the dark $F = \pm 2$ state. The same holds for transitions (5) and (6) that constitute an FLN peak at $-(\Delta E_{InP} + \Delta E_T/2)$. Hence, with respect to the highest-intensity FLN peak [transition (2)], coupling to optical phonons in ZnSe [transitions (3) and (4)] results in a peak shifted by $-(\Delta E_{ZnSe} - \Delta E_T/2)$ and coupling to InP phonons [transitions (5) and (6)] in a peak shifted by $-(\Delta E_{InP} - \Delta E_T/2)$.

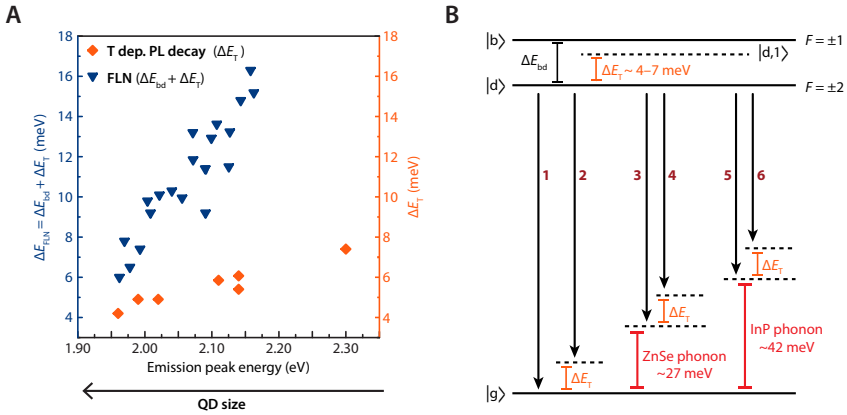

Figure 3.6. Comparison of the thermal activation energies obtained from PL decay measurements and the energy splitting obtained from the FLN spectra. a) Comparison of the results of the activation energy obtained from the time-resolved PL decay at varying *T* (orange diamonds), and the energy splitting obtained from the fluorescence line-narrowing (blue triangles). The *x*-axis displays the monitored PL emission peak energy or the emission energy in FLN, both at 4 K. b) An overview of all possible recombination processes in InP/ZnSe QDs.

3.3 Conclusion

In conclusion, we presented a detailed study of the fine structure of InP/ZnSe core/shell QDs using FLN experiments in a varying magnetic field, combined with *T*-dependent PL decay and Raman spectroscopic analysis. We observe that the lowest-energy fine structure exciton state is a $\mathrm{F} = \pm 2$ dark state, from which radiative recombination is assisted by coupling to confined acoustic phonons with energy ranging from 4 to 7 meV, depending on the core diameter. The FLN spectra are explained by coupling of the dark exciton state to LO, TO, and confined acoustic phonon modes of the core/shell QDs. Our data indicate that the highest-intensity FLN peak is an acoustic phonon replica rather than a zero-phonon line, implying that the splitting between the dark and bright fine structure exciton states is smaller than the energy separation observed between the $\mathrm{F} = \pm 1$ state and the highest-intensity peak in the FLN spectra (6–16 meV).

3.4 Methods

Sample preparation. InP/ZnSe QDs with different core diameters were synthesized, following the method reported in ref. 21. Core-only InP QDs were synthesized following the method of ref. 64. The QD samples were washed by precipitation with methanol, isolated by centrifugation and redispersed in toluene and 1-dodecanethiol. To achieve a QDs film the solution was deposited using a *drop-cast* method on crystalline silicon substrate.

HAADF-STEM and Energy Dispersive X-ray Spectroscopy. High-resolution high-angle annular dark field scanning transmission electron microscopy (HAADF-STEM) measurements were performed using an aberration corrected cubed FEI Titan 60–300 electron microscope operated at 120 kV. EDS measurements were performed on an FEI Osiris electron microscope operated at 200 kV. Acquisition time for EDS measurements was ~500 s. To avoid contamination growth during the experiment, the TEM grid was kept at 80 degrees for 4 hours and then transferred directly inside the microscope. In order to check whether the heat treatment changed the internal structure or not, diffraction patterns have been acquired before and after the treatment.

Temperature dependence of the Time-resolved Photoluminescence (PL). The Time-resolved PL measurements were performed on a set of QD ensemble samples. The excitation was provided by a pulsed diode laser, operating at 375 nm with a repetition rate of 100 kHz for all samples.

The Time-resolved PL decay curves were obtained by a time-correlated single photon counting detector where the average count rate was kept at 3% of the laser repetition rate. This low excitation fluence was used in order to maintain single photon statistics and avoid multiexciton formation.

The Time-resolved PL measurements were performed monitoring the PL peak wavelength. The PL peak wavelength was selected, at each temperature, based on PL measurements, and the signal was dispersed by a monochromator (1200 grooves/mm grating, blazed at 500 nm) and detected by a fast photomultiplier tube (PMT). For both PL and Time-resolved PL measurements, the PL was filtered through a 460 nm long-pass filter to eliminate scattered laser light. The QDs solutions were contained in a quartz cuvette and mounted in a continuous He-flow cryostat allowing for measurements down to 4 K. In addition, measurements down to 10 mK were performed on QD films (see sample preparation) using a Bluefors dilution refrigerator at KTH in Stockholm.

Magneto-optical measurements in high magnetic fields. Optical experiments at low temperatures and high magnetic fields were performed at the High Field Magnet Laboratory (Radboud University), using two spectroscopic techniques: polarized PL and Fluorescence Line-Narrowing (FLN) spectroscopy. For these experiments the samples used were QD films (see sample preparation above). The samples were mounted in a titanium sample holder on top of a three-axis piezo-positioner. The laser beam was focused on the sample by a singlet lens (10 mm focal length). The same lens was used to collect the PL emission and direct it to the detection setup (Backscattering geometry). The samples and optical probe were mounted inside a liquid-helium bath cryostat (4.2 K) inserted in a 50 mm bore Florida-Bitter electro-magnet with a maximum field strength of 30 T. All optical experiments were performed in Faraday geometry, *i.e.* with both incident and scattered lights parallel to the magnetic field direction.

Polarized PL measurements were performed in time-integrated and time-resolved configuration, using the same excitation source, in continuous or pulsed excitation mode. The excitation was circularly polarized with the use of a linear polarizer and a Babinet Soleil compensator. The PL light was guided through a 0.3 m long single grating spectrometer (300 grooves/mm grating) and detected by a liquid nitrogen cooled charge couple device (CCD) for time-integrated measurements and by an avalanche photo diode connected to a single-photon counter (time-correlated single photon counting) in the time-resolved configuration. The emitted photons were detected in crossed and co-polarization relative to the laser polarization by using a linear polarizer and a lambda-quarter wave plate. Cut-off optical filters were used in excitation and detection.

The FLN measurements were performed using a narrow excitation source, achieved by using a tunable jet-stream dye (Rhodamine 6G) laser and a 0.3 m long single grating spectrometer (1200 grooves/mm grating). This monochromatic laser beam was circularly polarized by means of a linear polarizer and a Babinet-Soleil compensator.

High resolution FLN emission was detected in crossed polarization mode relative to the laser polarization by using a linear polarizer and a lambda-quarter wave plate. The resonant-PL emission was analyzed by a 0.5 m long triple-grating spectrometer (three 1800 grooves/mm holographic gratings) in subtractive mode, equipped with a liquid nitrogen cooled CCD camera (Symphony-Horiba).

Raman spectroscopy measurements. Raman scattering measurements on InP core and InP/ZnSe core/shell samples (see sample preparation above) have been performed at High Field Magnet Laboratory (Radboud University). To achieve low temperatures, samples were placed in high vacuum (10^{-6} mbar) inside an optical ^{4}He cryostat (Microstat Oxford). Samples were probed in backscattering geometry with an incident laser line at 488 nm from a solid-state laser. To prevent both excessive laser heating and sample damage, a low laser power of 30 μW was used. The scattered light was filtered by a RazorEdge ultrasteep long-pass edge filter and analyzed by a 1 m long single grating (1200 grooves/mm) FHR-1000 Horiba spectrometer equipped with a nitrogen-cooled PyLoN CCD camera (Princeton Instruments). The resolution of our measurements was 1 cm^{-1}.

Fitting procedure of the exciton PL decay curves at variable temperatures (*T*). The fitting procedure is outlined in the Appendix Figures A3.3–A3.5. If the long component of the PL decay curve is fitted with a bi-exponential (Figure A3.3, blue points), we observe that the slowest time constant decreases with the increasing of *T* from 4 K to 20 K. At higher *T* the time constant starts to increase again as a function of *T*. This is attributed to *T*-activated multiple trapping/detrapping resulting in 'delayed' emission.[65] For this reason, we decided to use only a limited part of the PL decay curves, which should describe unperturbed exciton emission. This is shown in Figure A3.4, where we fitted single exponential decay to the time range dominated by direct radiative decay. This time range, however, varies with temperature. The exact time range taken in consideration for each temperature, and the criterion used to determine it, are described in the Appendix (Figure A3.4).

ACKNOWLEDGMENT: We acknowledge the support of the HFML-RU/FOM, member of the European Magnetic Field Laboratory (EMFL).

3.5 References

1 Jang, E.; Jun, S.; Jang, H.; Lim, J.; Kim, B.; Kim, Y. White-Light-Emitting Diodes with Quantum Dot Color Converters for Display Backlights. *Adv. Mater*. **2010**, 22, 3076–3080.

2 Kim, T.-H.; Jun, S.; Cho, K.-S.; Choi, B. L.; Jang, E. Bright and Stable Quantum Dots and Their Applications in Full-Color Displays. *MRS Bull.* **2013**, 38, 712–720.

3 Talapin, D. V.; Steckel, J. Quantum Dot Light-Emitting Devices. *MRS Bull.* **2013**, 38, 685–691.

4 Supran, G. J.; Shirasaki, Y.; Song, K. W.; Caruge, J.-M.; Kazlas, P. T.; Coe-Sullivan, S.; Andrew, T. L.; Bawendi, M. G.; Bulović, V. QLEDs for Displays and Solid-State Lighting. *MRS Bull*. **2013**, 38, 703–711.

5 Steckel, J. S.; Ho, J.; Coe-Sullivan, S. QDs Generate Light for Next-Generation Displays. *Photonics Spectra* **2014**, 48, 55–61.

6 Micic, O. I.; Curtis, C. J.; Jones, K. M.; Sprague, J. R.; Nozik, A. J. Synthesis and Characterization of InP Quantum Dots. *J. Phys. Chem*. **1994**, 98, 4966–4969.

7 Micic, O. I.; Sprague, J. R.; Curtis, C. J.; Jones, K. M.; Machol, J. L.; Nozik, A. J.; Giessen, H.; Fluegel, B.; Mohs, G.; Peyghambarian, N. Synthesis and Characterization of InP, GaP, and GaInP2 Quantum Dots. *J. Phys. Chem*. **1995**, 99, 7754–7759.

8 Mićić, O. I.; Ahrenkiel, S. P.; Nozik, A. J. Synthesis of Extremely Small InP Quantum Dots and Electronic Coupling in Their Disordered Solid Films. *Appl. Phys. Lett*. **2001**, 78, 4022–4024.

9 Guzelian, A. A.; Katari, J. E. B.; Kadavanich, A. V.; Banin, U.; Hamad, K.; Juban, E.; Alivisatos, A. P.; Wolters, R. H.; Arnold, C. C.; Heath, J. R. Synthesis of Size-Selected, Surface-Passivated InP Nanocrystals. *J. Phys. Chem*. **1996**, 100, 7212–7219.

10 Lucey, D. W.; MacRae, D. J.; Furis, M.; Sahoo, Y.; Cartwright, A. N.; Prasad, P. N. Monodispersed InP Quantum Dots Prepared by Colloidal Chemistry in a Noncoordinating Solvent. *Chem. Mater.* **2005**, 17, 3754–3762.

11 Battaglia, D.; Peng, X. Formation of High Quality InP and InAs Nanocrystals in a Noncoordinating Solvent. *Nano Lett*. **2002**, 2, 1027–1030.

12 Nozik, A. J.; Mićić, O. I. Colloidal Quantum Dots of III-V Semiconductors. *MRS Bull*. **1998**, 23, 24–30.

13 Xie, R.; Battaglia, D.; Peng, X. Colloidal InP Nanocrystals as Efficient Emitters Covering Blue to Near-Infrared. *J. Am. Chem. Soc*. **2007**, 129, 15432–15433.

14 Joung, S.; Yoon, S.; Han, C.-S.; Kim, Y.; Jeong, S. Facile Synthesis of Uniform Large-Sized InP Nanocrystal Quantum Dots Using Tris(Tert-Butyldimethylsilyl)Phosphine. *Nanoscale Res. Lett.* **2012**, 7, 93.

15 Pietra, F.; De Trizio, L.; Hoekstra, A. W.; Renaud, N.; Prato, M.; Grozema, F. C.; Baesjou, P. J.; Koole, R.; Manna, L.; Houtepen, A. J. Tuning the Lattice Parameter of InxZnyP for Highly Luminescent Lattice-Matched Core/Shell Quantum Dots. *ACS Nano* **2016**, 10, 4754–4762.

16 Dupont, D.; Tessier, M. D.; Smet, P. F.; Hens, Z. Indium Phosphide-Based Quantum Dots with Shell-Enhanced Absorption for Luminescent Down-Conversion. *Adv. Mater*. **2017**, 29, 1700686.

17 Song, W. S.; Lee, H. S.; Lee, J. C.; Jang, D. S.; Choi, Y.; Choi, M.; Yang, H. Amine-Derived Synthetic Approach to Color-Tunable InP/ZnS Quantum Dots with High Fluorescent Qualities. *J. Nanoparticle Res*. **2013**, 15, 1750.

18 Coropceanu, I.; Bawendi, M. G. Core/Shell Quantum Dot Based Luminescent Solar Concentrators with Reduced Reabsorption and Enhanced Efficiency. *Nano Lett.* **2014**, 14, 4097–4101.

19 Ryu, E.; Kim, S.; Jang, E.; Jun, S.; Jang, H.; Kim, B.; Kim, S. W. Step-Wise Synthesis of InP/ZnS Core - Shell Quantum Dots and the Role of Zinc Acetate. *Chem. Mater.* **2009**, 21, 573–575.

20 Li, L.; Reiss, P. One-Pot Synthesis of Highly Luminescent InP/ZnS Nanocrystals without Precursor Injection. *J. Am. Chem. Soc.* **2008**, 130, 11588–11589.

21 Tessier, M. D.; Dupont, D.; De Nolf, K.; De Roo, J.; Hens, Z. Economic and Size-Tunable Synthesis of InP/ZnE (E = S, Se) Colloidal Quantum Dots. *Chem. Mater.* **2015**, 27, 4893–4898.

22 Qu, L.; Peng, X. Control of Photoluminescence Properties of CdSe Nanocrystals in Growth. *J. Am. Chem. Soc.* **2002**, 124, 2049–2055.

23 Chen, O.; Zhao, J.; Chauhan, V. P.; Cui, J.; Wong, C.; Harris, D. K.; Wei, H.; Han, H.-S.; Fukumura, D.; Jain, R. K.; et al. Compact High-Quality CdSe–CdS Core–shell Nanocrystals with Narrow Emission Linewidths and Suppressed Blinking. *Nat. Mater.* **2013**, 12, 445–451.

24 Cui, J.; Beyler, A. P.; Marshall, L. F.; Chen, O.; Harris, D. K.; Wanger, D. D.; Brokmann, X.; Bawendi, M. G. Direct Probe of Spectral Inhomogeneity Reveals Synthetic Tunability of Single-Nanocrystal Spectral Linewidths. *Nat. Chem.* **2013**, 5, 602–606.

25 Chandrasekaran, V.; Tessier, M. D.; Dupont, D.; Geiregat, P.; Hens, Z.; Brainis, E. Nearly Blinking-Free, High-Purity Single-Photon Emission by Colloidal InP/ZnSe Quantum Dots. *Nano Lett.* **2017**, 17, 6104–6109.

26 Mićić, O. I.; Sprague, J.; Lu, Z.; Nozik, A. J. Highly Efficient Band-Edge Emission from InP Quantum Dots. *Appl. Phys. Lett.* **1996**, 68, 3150–3152.

27 Ahrenkiel, S. P.; Mićić, O. I.; Miedaner, A.; Curtis, C. J.; Nedeljković, J. M.; Nozik, A. J. Synthesis and Characterization of Colloidal InP Quantum Rods. *Nano Lett.* **2003**, 3, 833–837.

28 Nedeljković, J. M.; Mićić, O. I.; Ahrenkiel, S. P.; Miedaner, A.; Nozik, A. J. Growth of InP Nanostructures via Reaction of Indium Droplets with Phosphide Ions: Synthesis of InP Quantum Rods and InP-TiO2 Composites. *J. Am. Chem. Soc.* **2004**, 126, 2632–2639.

29 Ellingson, R. J.; Blackburn, J. L.; Yu, P.; Rumbles, G.; Mićić, O. I.; Nozik, A. J. Excitation Energy Dependent Efficiency of Charge Carrier Relaxation and Photoluminescence in Colloidal InP Quantum Dots. *J. Phys. Chem. B* **2002**, 106, 7758–7765.

30 Micic, O. I.; Cheong, H. M.; Fu, H.; Zunger, A.; Sprague, J. R.; Mascarenhas, A.; Nozik, A. J. Size-Dependent Spectroscopy of InP Quantum Dots. *J. Phys. Chem.* B **1997**, 101, 4904–4912.

31 Mushonga, P.; Onani, M. O.; Madiehe, A. M.; Meyer, M. Indium Phosphide-Based Semiconductor Nanocrystals and Their Applications. *J. Nanomater.* **2012**, 2012, 1–11.

32 Narayanaswamy, A.; Feiner, L. F.; van der Zaag, P. J. Temperature Dependence of the Photoluminescence of InP/ZnS Quantum Dots. *J. Phys. Chem. C* **2008**, 3, 6775–6780.

33 Voznyy, O.; Levina, L.; Fan, F.; Walters, G.; Fan, J. Z.; Kiani, A.; Ip, A. H.; Thon, S. M.; Proppe, A. H.; Liu, M.; et al. Origins of Stokes Shift in PbS Nanocrystals. *Nano Lett.* **2017**, 17, 7191–7195.

34 De Mello Donegá, C. Formation of Nanoscale Spatially Indirect Excitons: Evolution of the Type-II Optical Character of CdTe/CdSe Heteronanocrystals. Phys. Rev. B - Condens. *Matter Mater. Phys.* **2010**, 81, 1–20.

35 Efros, A.; Rosen, M.; Kuno, M.; Nirmal, M.; Norris, D.; Bawendi, M. Band-Edge Exciton in Quantum Dots of Semiconductors with a Degenerate Valence Band: Dark and Bright Exciton States. *Phys. Rev. B* **1996**, 54, 4843–4856.

36 Fu, H.; Zunger, A. InP Quantum Dots: Electronic Structure, Surface Effects, and the Redshifted Emission. Phys. Rev. B **1997**, 56, 1496.

37 Fu, H.; Wang, L.-W.; Zunger, A. Excitonic Exchange Splitting in Bulk Semiconductors. *Phys. Rev. B* **1999**, 59, 5568–5574.

38 Blokland, J. H.; Claessen, V. I.; Wijnen, F. J. P.; Groeneveld, E.; de Mello Donegá, C.; Vanmaekelbergh, D.; Meijerink, A.; Maan, J. C.; Christianen, P. C. M. Exciton Lifetimes of CdTe Nanocrystal Quantum Dots in High Magnetic Fields. *Phys. Rev. B* **2011**, 83, 035304.

39 Rafipoor, M.; Dupont, D.; Tornatzky, H.; Tessier, M. D.; Maultzsch, J.; Hens, Z.; Lange, H. Strain Engineering in InP/(Zn,Cd)Se Core/Shell Quantum Dots. *Chem. Mater.* **2018**, 30, 4393–4400.

40 Fan, F.; Voznyy, O.; Sabatini, R. P.; Bicanic, K. T.; Adachi, M. M.; McBride, J. R.; Reid, K. R.; Park, Y.-S.; Li, X.; Jain, A.; et al. Continuous-Wave Lasing in Colloidal Quantum Dot Solids Enabled by Facet-Selective Epitaxy. *Nature* **2017**, 544, 75–79.

41 Biadala, L.; Siebers, B.; Beyazit, Y.; Tessier, M. D.; Dupont, D.; Hens, Z.; Yakovlev, D. R.; Bayer, M. Band-Edge Exciton Fine Structure and Recombination Dynamics in InP/ZnS Colloidal Nanocrystals. *ACS Nano* **2016**, 10, 3356–3364.

42 Ministro, J. A Study on the Synthesis and the Optical Properties of InP-Based Quantum Dots, *Master Thesis*, Gent University, **2014**.

43 Qu, L.; Peng, X. Control of Photoluminescence Properties of CdSe Nanocrystals in Growth. *J. Am. Chem. Soc.* **2002**, 124, 2049–2055.

44 Haruna, K.; Maeta, H.; Ohashi, K.; Koike, T. The Thermal Expansion Coefficient and Gruneisen Parameter of InP Crystal at Low Temperatures. *J. Phys. C Solid State Phys.* **1987**, 20, 5275–5279.

45 Furis, M.; Htoon, H.; Petruska, M. A.; Klimov, V. I.; Barrick, T.; Crooker, S. A. Bright-Exciton Fine Structure and Anisotropic Exchange in CdSe Nanocrystal Quantum Dots. *Phys. Rev. B* **2006**, 73, 241313.

46 Wijnen, F. J. P.; Blokland, J. H.; Chin, P. T. K.; Christianen, P. C. M.; Maan, J. C. Competition between Zero-Phonon and Phonon-Assisted Luminescence in Colloidal CdSe Quantum Dots. *Phys. Rev. B - Condens. Matter Mater. Phys.* **2008**, 78.

47 Granados del Águila, A.; Pettinari, G.; Groeneveld, E.; de Mello Donegá, C.; Vanmaekelbergh, D.; Maan, J. C.; Christianen, P. C. M. Optical Spectroscopy of Dark and Bright Excitons in CdSe Nanocrystals in High Magnetic Fields. *J. Phys. Chem. C* **2017**, 121, 23693–23704.

48 Lu, Z. Q.; Quinn, T.; Reehal, H. S. Polarization-Dependent Raman Spectra of Thin Crystalline Silicon Films. *J. Appl. Phys*. **2005**, 97, 033512.

49 Hou, H.-J.; Kong, F.-J. Theoretical Investigation on the Structural, Dynamical, and Thermodynamic Properties of the Zinc-Blende InX (X = P, As, Sb). *Phys. status solidi* **2011**, 248, 1399–1404.

50 Seong, M. J.; Mićić, O. I.; Nozik, A. J.; Mascarenhas, A.; Cheong, H. M. Size-Dependent Raman Study of InP Quantum Dots. *Appl. Phys. Lett.* **2003**, 82, 185–187.

51 Rössler, U. New Data and Updates for Several Semiconductors with Chalcopyrite Structure, for Several II-VI Compounds and Diluted Magnetic IV-VI Compounds; *Springer: Berlin, Heidelberg*, **2013**.

52 Gadret, E. G.; de Lima, M. M.; Madureira, J. R.; Chiaramonte, T.; Cotta, M. A.; Iikawa, F.; Cantarero, A. Optical Phonon Modes of Wurtzite InP. *Appl. Phys. Lett.* **2013**, 102, 122101.

53 Buhot, J.; Gallais, Y.; Cazayous, M.; Sacuto, A.; Piekarz, P.; Lapertot, G.; Aoki, D.; Méasson, M.-A. Raman Active High Energy Excitations in URu2Si2. *Phys. B Condens. Matter* **2017**, 506, 19–22.

54 Sun, C. Q.; Pan, L. K.; Li, C. M.; Li, S. Size-Induced Acoustic Hardening and Optic Softening of Phonons in InP, CeO2, SnO2, CdS, Ag, and Si Nanost. *Phys. Rev. B* **2005**, 72, 134301.

55 Oron, D.; Aharoni, A.; de Mello Donega, C.; van Rijssel, J.; Meijerink, A.; Banin, U. Universal Role of Discrete Acoustic Phonons in the Low-Temperature Optical Emission of Colloidal Quantum Dots. *Phys. Rev. Lett.* **2009**, 102, 177402.

56 Takagahara, T. Electron—phonon Interactions in Semiconductor Nanocrystals. J. Lumin. **1996**, 70, 129–143.

57 Lamb, H. On the Vibrations of an Elastic Sphere. P*roc. London Math. Soc.* **1881**, s1-13, 189–212.

58 Cerullo, G.; De Silvestri, S.; Banin, U. Size-Dependent Dynamics of Coherent Acoustic Phonons in Nanocrystal Quantum Dots. *Phys. Rev. B* **1999**, 60, 1928–1932.

59 Eilers, J.; Van Hest, J.; Meijerink, A.; Donega, C. D. M. Unravelling the Size and Temperature Dependence of Exciton Lifetimes in Colloidal ZnSe Quantum Dots. *J. Phys. Chem. C* **2014**, 118, 23313–23319.

60 Granados del Águila, A.; Groeneveld, E.; Maan, J. C.; de Mello Donegá, C.; Christianen, P. C. M. Effect of Electron–Hole Overlap and Exchange Interaction on Exciton Radiative Lifetimes of CdTe/CdSe Heteronanocrystals. *ACS Nano* **2016**, 10, 4102–4110.

61 Granados del Águila, A.; Jha, B.; Pietra, F.; Groeneveld, E.; de Mello Donegá, C.; Maan, J. C.; Vanmaekelbergh, D.; Christianen, P. C. M. Observation of the Full Exciton and Phonon Fine Structure in CdSe/CdS Dot-in-Rod Heteronanocrystals. *ACS Nano* **2014**, 8, 5921–5931.

62 Wong, C. Y.; Kim, J.; Nair, P. S.; Nagy, M. C.; Scholes, G. D. Relaxation in the Exciton Fine Structure of Semiconductor Nanocrystals. *J. Phys. Chem. C* **2009**, 113, 795–811.

63 Huxter, V. M.; Scholes, G. D. Acoustic Phonon Strain Induced Mixing of the Fine Structure Levels in Colloidal CdSe Quantum Dots Observed by a Polarization Grating Technique. *J. Chem. Phys.* **2010**, 132, 104506.

64 Stein, J. L.; Mader, E. A.; Cossairt, B. M. Luminescent InP Quantum Dots with Tunable Emission by Post-Synthetic Modification with Lewis Acids. *J. Phys. Chem. Lett.* **2016**, 7, 1315–1320.

65 Rabouw, F. T.; Kamp, M.; van Dijk-Moes, R. J. A.; Gamelin, D. R.; Koenderink, A. F.; Meijerink, A.; Vanmaekelbergh, D. Delayed Exciton Emission and Its Relation to Blinking in CdSe Quantum Dots. *Nano Lett.* **2015**, 15, 7718–7725.

3.6 Appendix

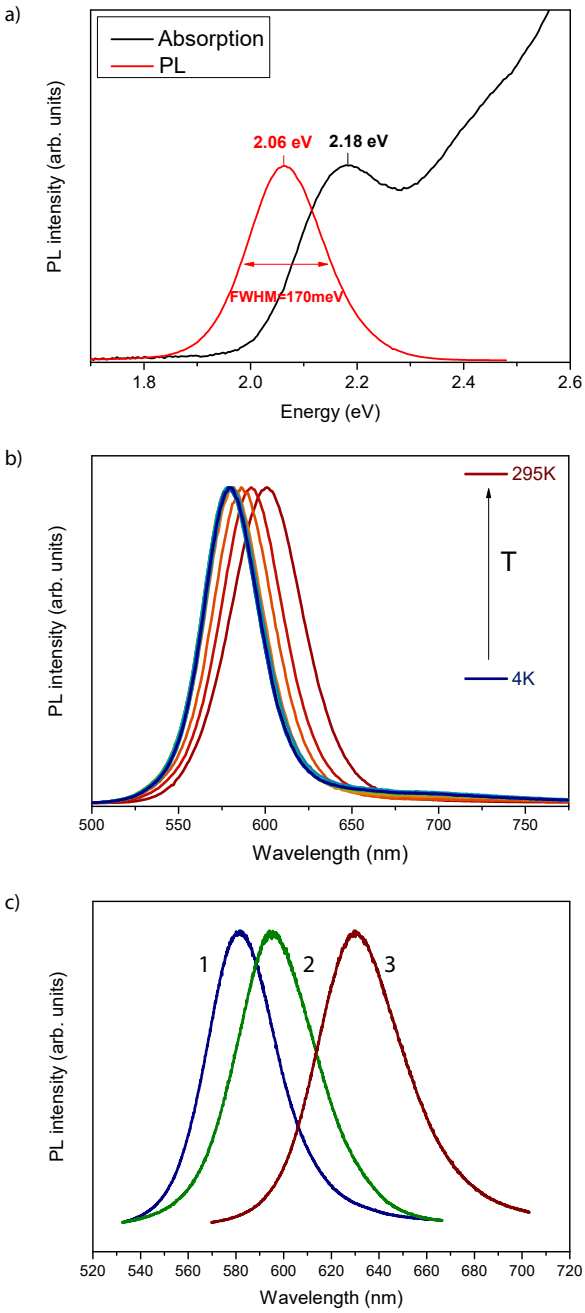

Figure A3.1: a) Absorption and PL spectra for sample 1 (see A3.1c), detected at room temperature. b) PL spectra detected at different temperatures down to 4 K. c) Normalized ensemble PL spectra at low temperature (4 K) of the three InP/ZnSe samples having various core sizes (from 2.9 nm to 3.6 nm).

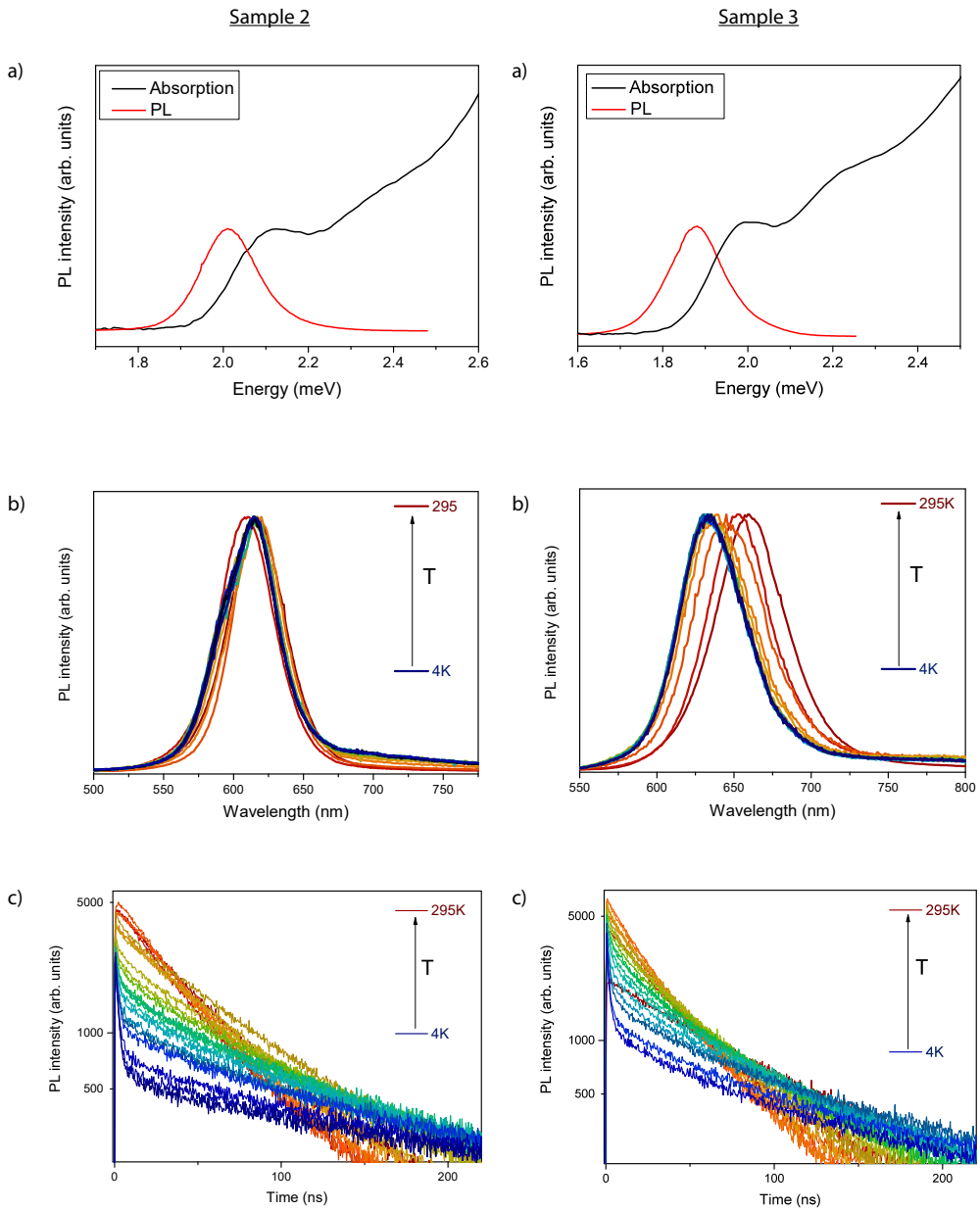

Figure A3.2: a) Absorption and PL spectra for sample 2 and 3, detected at room temperature. b) PL spectra detected at different temperatures down to 4 K. c) Thermally activated PL decay at zero magnetic field for samples 2 and 3, measured at the PL peak maximum (depending on temperature see Figure A3.1b), at various temperatures from 4 K (blue) to 295 K (dark red).

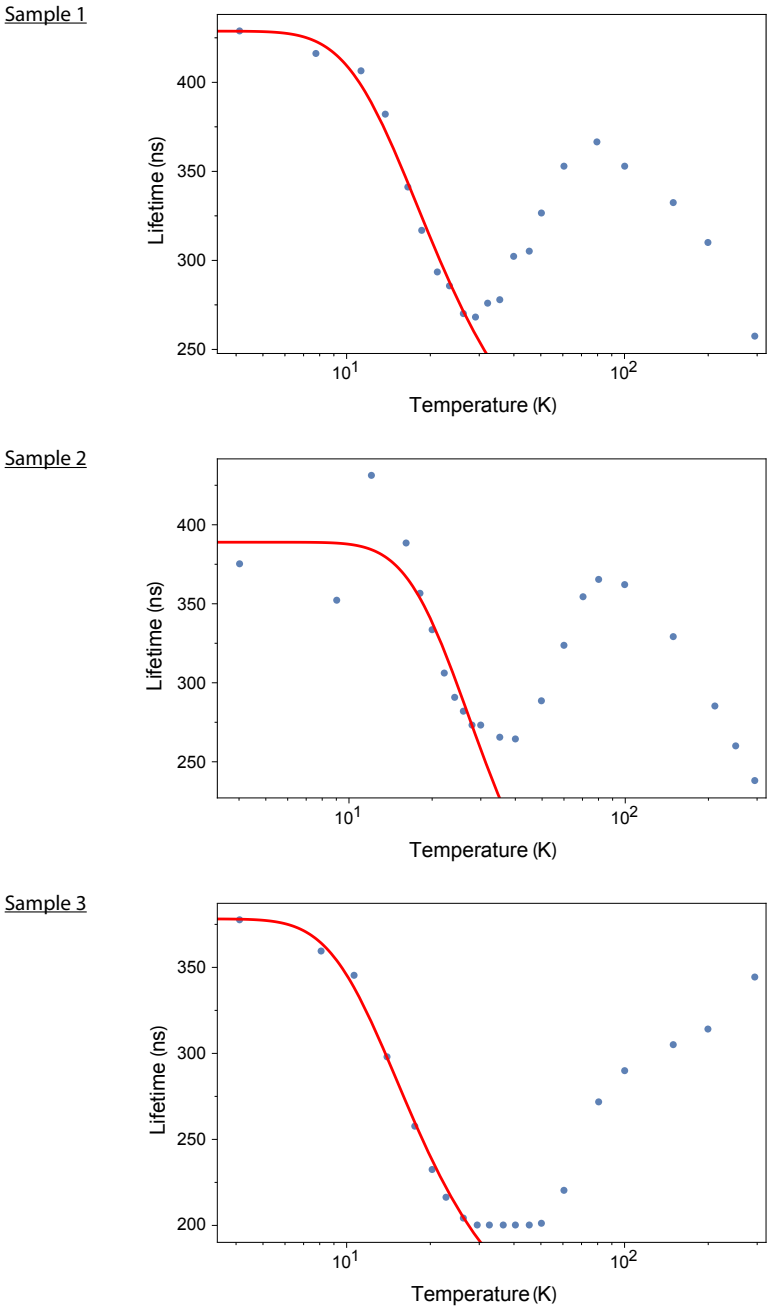

Figure A3.3: Long component lifetime from a bi-exponential fitting (blue points) of time-resolved PL curves for the three samples and respective fitting (red line) related to the three-level system thermal occupation.

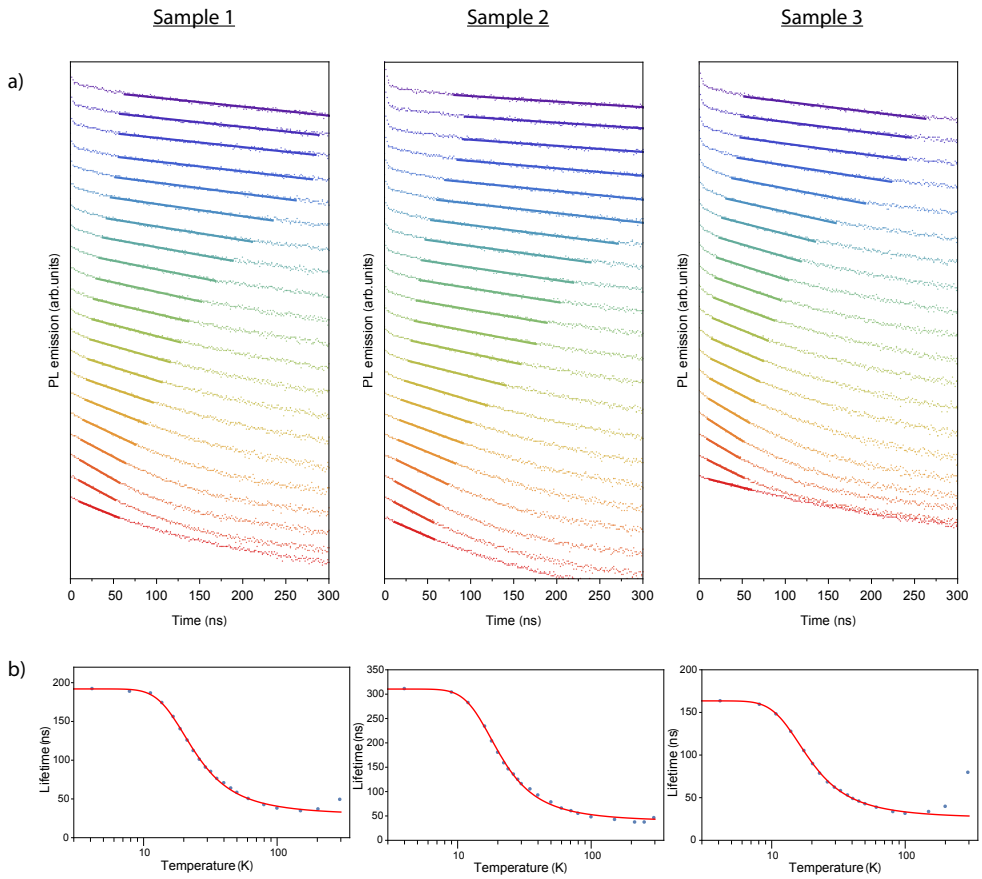

Figure A3.4: The PL decay curves are very non-exponential. Fast components are presumably due to slow thermalization from the bright state, only prominent at low temperatures. Slow components, resembling power-law decay, may be due to reversible trapping, most prominent at high temperatures. Only the intermediate time range shows the radiative decay of the (dark) exciton state. To determine the decay constant of the radiative component, we fitted single exponential decay to the time range dominated by direct radiative decay. This time range, however, varies with temperature. We started with the data recorded at T_1 = 4 K. The lifetime of τ_1 was set as initial parameter then used to define the time range on which the next measurement at T_2 = 8 K was fitted. For each measurement at temperature T_{i+1}, the time range considered was determined by the fit results at the next-lower temperature: between $0.3\tau_i$ and $1.5\tau_i$. a) PL decay at the peak maximum at various temperatures from 4 K (blue spectrum) to 295 K (red spectrum) for the three samples. For each sample, the solid lines in the figure above show the single-exponential fits, in semi-log representation, exactly on the time range on which they were optimized. b) The exciton lifetime as a function of temperature for the three samples and respective fitting (red line) related to the three-level system thermal occupation. The energy difference between the lowest exciton levels are ΔE~5.5 meV for sample 1, ΔE~4.9 meV for sample 2 and ΔE~4.3 meV for sample 3. Note that when varying the range of the fitting we achieve consistent values.

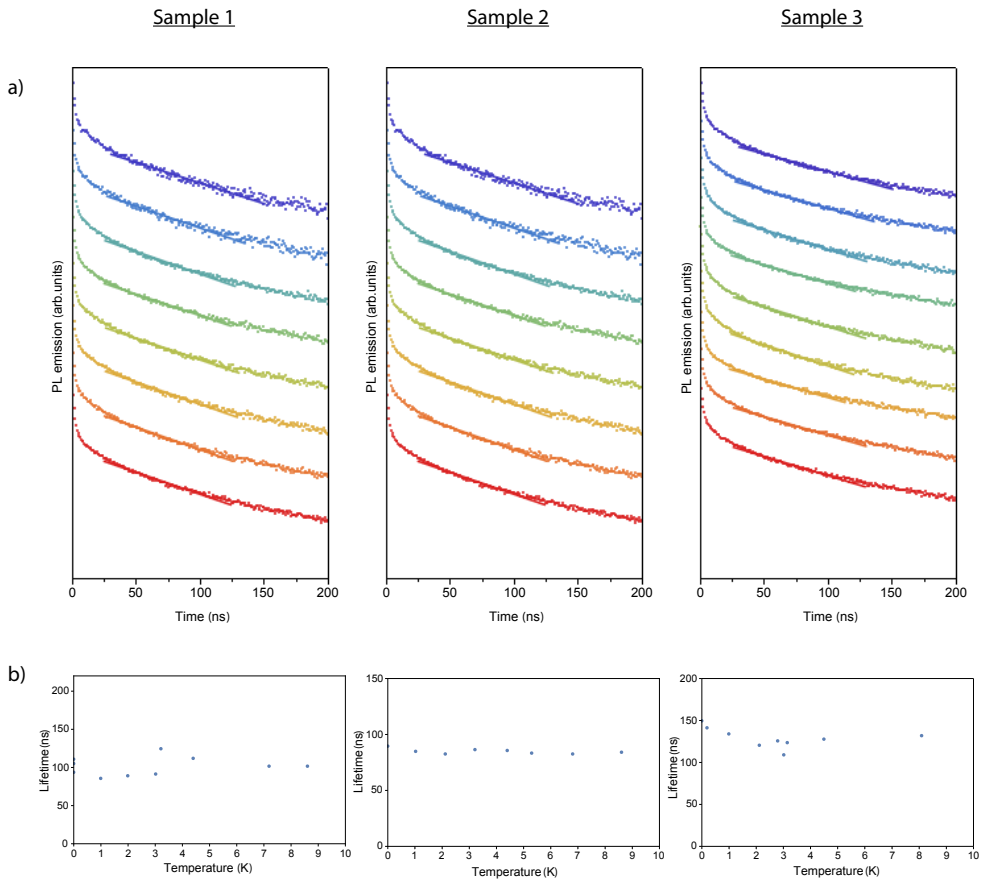

Figure A3.5: a) PL decay at the peak maximum at various temperatures from 9 K (red spectrum) to 10 mK (blue spectrum) for the three samples. b) Respective long component of the exciton lifetime as a function of temperature calculated as described in Figure A3.4. It remains constant in this range of temperature.

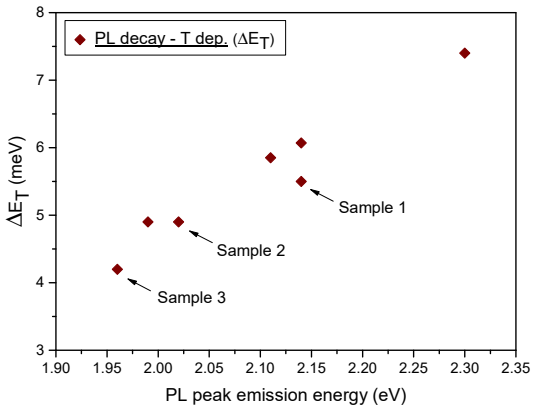

Figure A3.6: Activation energy obtained from the time-resolved PL decay at varying T. The *x*-axis displays the monitored PL emission peak-energy.

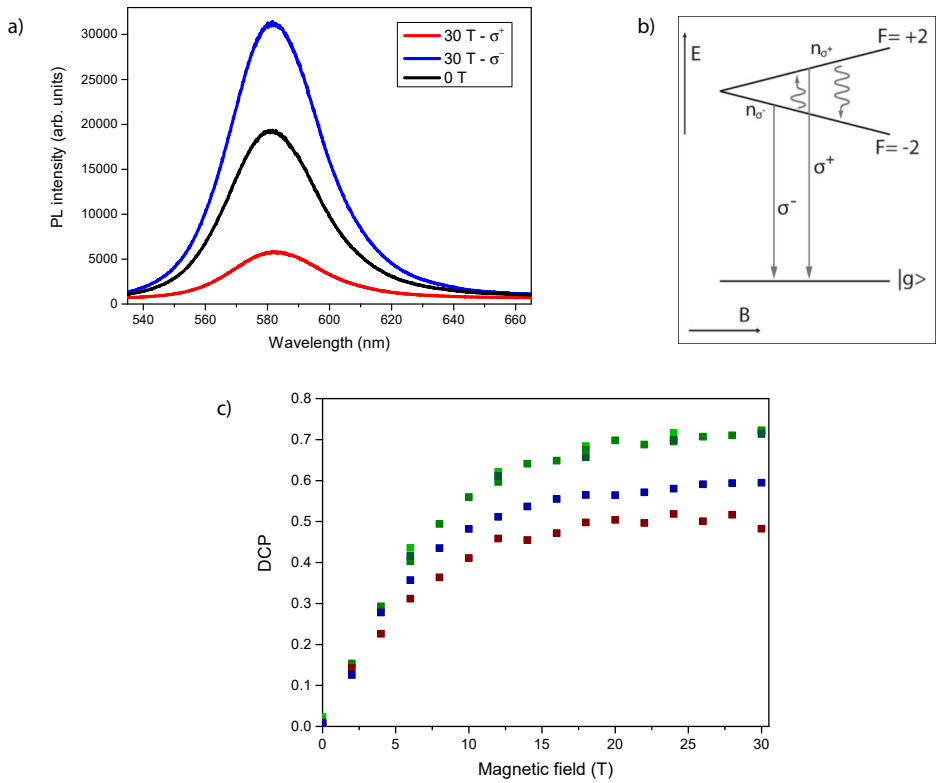

Figure A3.7: a) PL intensity of right and left circularly polarized emission at 0 T (black) and 30 T (blue and red) of sample 1. b) Exciton energy level scheme and polarized emission due to lifting of the degeneracy of the excitonic level in magnetic field (Zeeman effect). c) Steady-state Degree of Circular Polarization (DCP) at 4 K (green for sample 1, red sample 2, blue sample 3) excited with different polarization: circularly left polarized, circularly right polarized and linearly polarized (different green tonality in sample 1, same trend for the other samples).

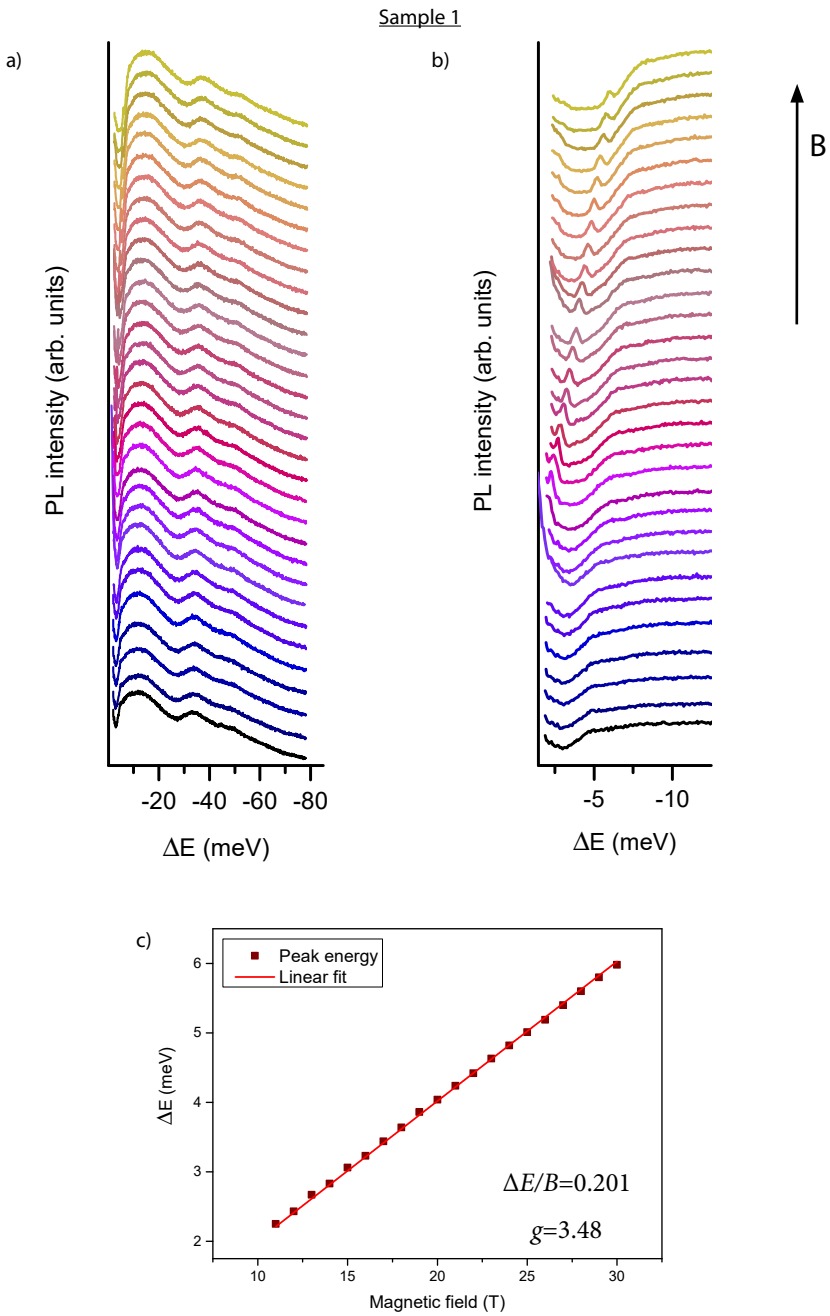

Figure A3.8: a) FLN spectra at low temperature (4 K) related to sample 1, excited with circular right polarization (σ^+) at 590 nm, at various fields from 0 T to 30 T. b) Zoom-in at low energy that shows fluorescence from the lower Zeeman state after spin flip. The resonantly excited state (2.1 eV) is taken as reference and set to 0 meV. The spectra are vertically shifted for clarity. c) Zeeman splitting of the bright exciton state as a function of applied magnetic field. Linear fitting is shown with solid line, from which we extract the *g*-factor.

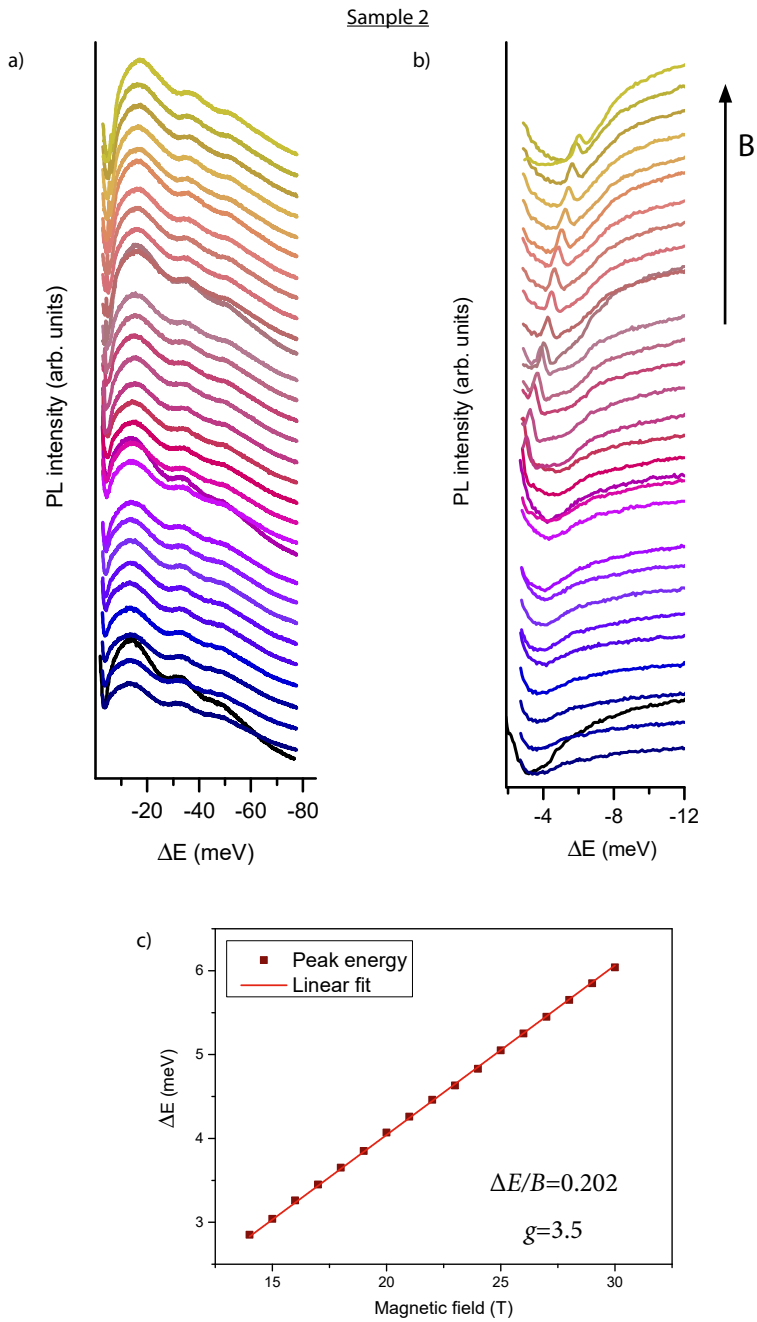

Figure A3.9: a) FLN spectra at low temperature (4 K) related to sample 2, excited with circular right polarization (σ^+) at 590 nm, at various fields from 0 T to 30 T. b) Zoom-in at low energy that shows fluorescence from the lower Zeeman state after spin flip. The resonantly excited state (2.1 eV) is taken as reference and set to 0 meV. The spectra are vertically shifted for clarity. c) Zeeman splitting of the bright exciton state as a function of applied magnetic field. Linear fitting is shown with solid line, from which we extract the *g*-factor.

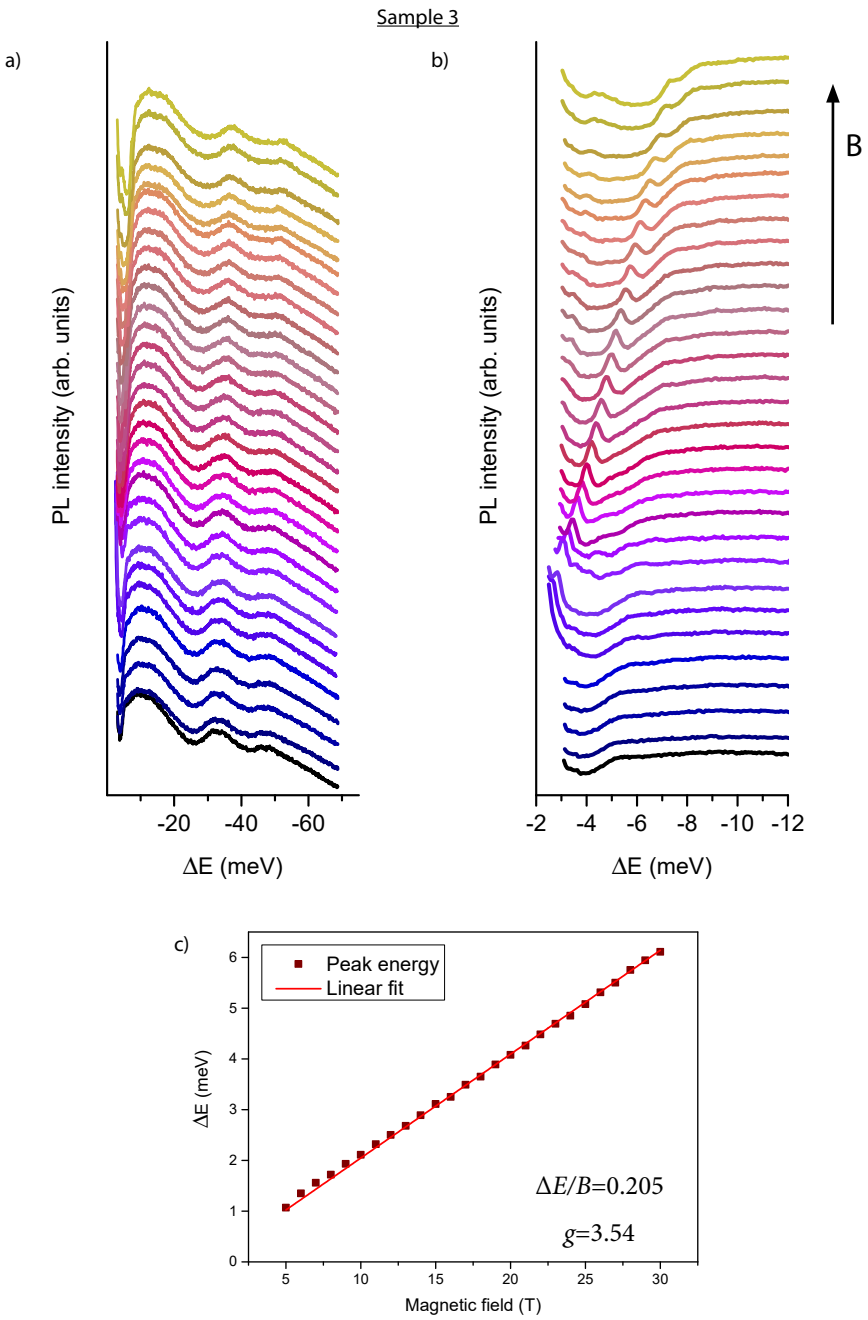

Figure A3.10: a) FLN spectra at low temperature (4 K) related to sample 3, excited with circular right polarization (σ^+) at 627 nm, at various fields from 0 T to 30 T. b) Zoom-in at low energy that shows fluorescence from the lower Zeeman state after spin flip. The resonantly excited state (2.0 eV) is taken as reference and set to 0 meV. The spectra are vertically shifted for clarity. c) Zeeman splitting of the bright exciton state as a function of applied magnetic field. Linear fitting is shown with solid line, from which we extract the *g*-factor.

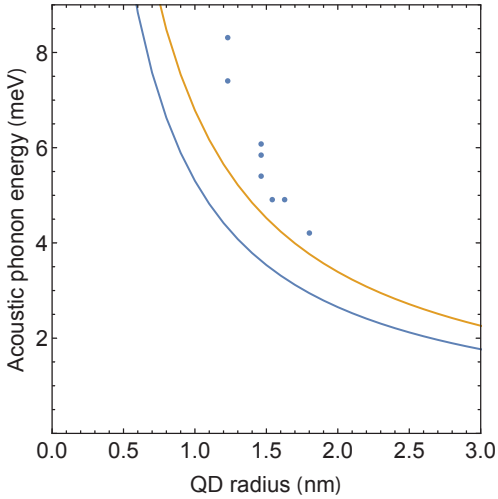

Figure A3.11: Acoustic-phonon energies from temperature-dependent lifetime measurements (blue circles) compared with those calculated from Lamb theory for InP hard spheres: orange line is the l = 0 mode and blue line is the lowest energy l = 2 mode.

Chapter 4

Slow spin relaxation and absence of state mixing in the exciton fine structure of InP/ZnS quantum dots

Based on:
Hyperfine interactions and slow spin dynamics in InP-based core/shell colloidal nanocrystals.
Annalisa Brodu, Mickael D. Tessier, Damien Canneson, Dorian Dupont, Mariana V. Ballottin, Peter C. M. Christianen, Celso de Mello Donega, Zeger Hens, Dmitri R. Yakovlev, Manfred Bayer, Daniel Vanmaekelbergh, and Louis Biadala.
Under review

Abstract

Colloidal InP core/shell nanocrystals could become a believable alternative for CdSe-based nanocrystals for opto-electronic applications, provided that the optical properties are better understood and controlled. Here, we report a detailed study of the exciton fine structure and spin dynamics of InP/ZnS core/shell nanocrystals in an ensemble. The fine structure is resolved by fluorescence line narrowing spectroscopy in a varying magnetic field up to 30 tesla. The spin dynamics were studied by monitoring the time- and energy-resolved photoluminescence and the degree of circular polarization. We found that the lowest exciton state is a forbidden dark state that predominantly decays through phonon-assisted processes. Several results show that mixing of this dark state with the nearest allowed bright state does not occur, up to the highest magnetic fields applied. The degree of circular polarization from the dark state builds up very slowly and saturates at values around 16%. The spin relaxation between the Zeeman lines of the lowest dark level is very slow, showing relaxation time of ~ 400 ns. In the upper bright state, the spin relaxation is much faster, but still takes about 10 ns. Our results demonstrate that the spin physics in InP quantum dots deviates substantially from that in II-VI nanocrystals.

4.1 Introduction

Colloidal semiconductor nanocrystals (NCs) with quantum confinement in all three dimensions, also called quantum dots (QDs), remain to attract interest, since they show a bright luminescence that can be spectrally tuned by their size. For the visible spectrum, CdSe NCs have been the workhorse, as surface passivation with (Zn,S,Se) shells have increased the photoluminescence (PL) quantum yield (QY) up to almost unity and their narrow emission band can be tuned over the entire visible spectrum. For applications in which Cd-containing nanocrystals are forbidden, InP QDs would form a believable alternative. Recently, synthesis methods for InP have been developed on the basis of cheap and safe In- and P-precursors, which allow the production of InP QDs on a large scale. Furthermore, suitable inorganic shells that contain Zn, Cd, S and Se have been developed that increased the PL QY from nearly zero to values up to 60%. This would enable applications of InP QDs as labels in biology,[1–3] as phosphors in large-scale lighting,[4–7] lasers[8] and quantum optics.[9–14] Nevertheless, experimental studies on the optical properties of colloidal InP QDs remain scarce and the understanding of the PL properties has remained limited. For example, InP QDs exhibit broader ensemble emission linewidths than their CdSe analogues.[15–17] This is mostly related to inhomogeneous broadening of the InP QD ensemble,[18–20] but also the exciton fine structure and the exciton-phonon coupling can contribute to the broadening.

InP NCs have a cubic zinc blende lattice. The lowest energy exciton (eightfold degenerate in bulk InP) is split into five fine structure levels by the electron-hole exchange interaction, and the crystal shape anisotropy. The resulting exciton fine structure levels are characterized by their exciton total angular momentum projection, $\mathrm{F} = \mathrm{S}+\mathrm{M}$ where S is the electron spin and M the angular momentum of the hole. The lowest exciton level is a $\mathrm{F} = \pm 2$ state (which is called 'dark' state because radiative recombination from it is forbidden within the electric dipole approximation), followed by higher-energy exciton states, with $\mathrm{F} = \pm 1$ (which are called 'bright' state because radiative recombination from it is allowed), and with $\mathrm{F} = 0$ (one optically dark and one optically bright).[21–23]

For crystals with a zinc blende or wurtzite lattice, a magnetic field parallel to crystal or shape symmetry axis (called q-axis) lifts the exciton spin degeneracy into Zeeman levels with projection $\mathrm{F} = -2$ and $\mathrm{F} = +2$ for the dark state, and $\mathrm{F} = -1$ and $\mathrm{F} = +1$ for the bright state. For a magnetic field B perpendicular to q-axis, the dark and bright exciton are mixed, so dark excitons obtain oscillator strength from the bright excitons.[22] It should be noted that no Zeeman splitting of the dark exciton with $\mathrm{F} = 0$ is expected, only a magnetic brightening due to admixing with bright exciton character when B is perpendicular to q-axis.[22,24] Once drop casted on substrate, spherical NCs have their q-axis randomly oriented with respect to an external magnetic field; this means that the Zeeman splitting and bright-dark mixing should be observed in ensemble measurements under high magnetic field. Thorough studies performed on ensembles of CdSe-based NCs have allowed to unveil the exciton fine structure in detail. It was observed that Zeeman interactions lift the spin degeneracy of the fine structure states, which leads to a splitting of the emission lines in PL spectra. The resulting spin polarization is clearly evidenced by

the degree of circular polarization of the PL in a magnetic field.[25–28] A strong signature of bright-dark mixing in CdSe QDs was the strong intensity increase of the zero-phonon line of the dark exciton with increasing magnetic field, as observed in Fluorescence Line Narrowing (FLN) on ensembles and in single dot experiments, as well.[22,29–31] In addition to these spectral properties, the magnetic field-induced bright-dark mixing is unambiguously evidenced in PL decay measurement in magnetic field. At 4 K and B = 0 T the PL decays occur on 2 markedly different timescales where the fast sub-nanosecond time stems from radiative recombination from higher energy levels shortly after the laser pulse and prior to thermalization, and the long living component from the radiative recombination of the dark exciton.[32,33] Applying an external magnetic field induces a shortening of the lifetime of the long component. To date, these fingerprints have been observed on pure CdSe QDs,[21] and CdSe QDs with different types of shell, *i.e.* CdSe/ZnS,[29,30] CdSe/CdS (dot-in-rod,[25,34] spherical with thin shell,[31,35]), and also CdSe nanoplatelets,[36,37] and on spherical CdTe QDs.[23]

Here we report a study of the time-, spectral- and polarization- resolved optical properties of InP/ZnS core/shell NCs under high magnetic field up to 30 T. This study allowed us to understand the origin of the spectral lines in FLN spectra of InP NCs. Notably we show that the radiative recombination of the dark exciton is almost exclusively achieved by a phonon-assisted process, in marked contrast with CdSe QDs and other colloidal NCs, where a strong zero-phonon-line (ZPL) signal was observed. In addition, the results show a lack of field-induced mixing between the bright and the dark states up to 30 T, a spin relaxation time comparable to the dark exciton lifetime (~1 μs), as well as PL decay lengthening. This forms again a marked contrast with CdSe QDs and other colloidal NCs.

4.2 Results and discussion

4.2.1 General spectroscopic investigation

We present results for five InP/ZnS core/shell QD samples (see ref. 33) optically investigated at the Experimentelle Physik 2 (Technische Universität Dortmund, Germany, by L. Biadala) under magnetic fields up to 15 T and two other InP/ZnS QD samples investigated at High Field Magnet Laboratory (Radboud University, Nijmegen, The Netherlands) under magnetic fields up to 30 T. The absorption and photoluminescence spectra of the latter two samples are shown in the Appendix, Figure A4.1a. For comparison, the results obtained with other InP core/shell QD samples, with shells composed of ZnSe or (Zn,Cd)Se are shown in Appendix, Figure A4.1b.

Due to the zinc blende crystal structure and nearly prolate shape of the InP cores, it can be expected that InP/ZnS nanocrystals will show an exciton fine structure comparable to that measured on CdSe-based NCs, with a dark ground state exciton that dominates the optical properties at cryogenic temperature.[33] It should be remarked here that in contrast with CdSe NCs, in InP/ZnS there is a PL peak 100 meV above the bright-dark doublet.[33] Therefore, special care should be taken when studying magnetic field-induced optical properties of InP/ZnS NCs. To overcome this specific problem and the general limitations

of ensemble-broadened PL spectra,[33] it is convenient to use Fluorescence Line Narrowing (FLN) spectroscopy: by using monochromatic laser light matching the low-energy side of the lowest-energy absorption peak, only a small sub-ensemble (*i.e.* having the largest core) of the InP/ZnS QDs are optically excited. As a result, the emission spectra sharpen by an order of magnitude, and the exciton fine structure can be studied, including the exciton-phonon side bands. The FLN spectra are presented in Figure 4.1a, measured at zero field and a field of 30 tesla. The spectra are referred to the energy of the excitation laser line, exciting the lowest bright state ($\mathrm{F} = \pm 1$). There is hardly any difference between the spectra at zero field and at 30 T. Such FLN spectra have also been observed by Micic et al. with InP QDs passivated with hydrogen fluoride.[38,39] The spectra consist of two broad peaks. The highest-intensity peak at around 23 meV from the laser line seems to be a convolution of at least two other resonances. In our analysis, we assume that the peak at around 58 meV represents the optical phonon replica of the dark state emission. We found from Raman spectroscopy that the energy of the InP core optical phonons is 43 meV (see Figure 3.5 in Chapter 3),[40] thus nearly identical to the bulk value for zinc blende InP.[40,41] Taking this phonon energy into account, we arrive at 15 meV, where we observe a small and poorly resolved feature. We assign this feature to the zero-phonon emission line of the dark state. The highest-intensiy peak at 23 meV is then attributed to the acoustic phonon sideband (Ac) in agreement with the recent study on InP/ZnSe NCs (Chapter 3).[42] From this analysis, we derive a dark-bright splitting of about 15 meV.

These findings of a dark state with a low-weight zero phonon line compared to the phonon-assisted peaks show that the radiative recombination of the dark exciton in InP NCs is almost exclusively phonon-assisted. This is in marked contrast with the findings with CdSe nanocrystals, where the ZPL of the dark state is dominant, as illustrated in Figure 4.1b,c. The magnetic field dependence of unpolarized FLN spectra strongly supports these results. Strikingly, Figure 4.1a shows that the FLN spectra do not depend on the magnetic field up to 30 T. The slight shift to lower energy stems from the Zeeman splitting. The intensity of the first peak (ZPL + acoustic replica) is not enhanced upon rising the magnetic field, we found that the intensity of the highest-intensity peak, in comparison to the optical phonon replica peak, changes less than 10% (a full set of spectra and comparison with other samples can be found in Appendix Figures A4.2 – A4.4). These remarkable results indicate the absence of magnetic field-induced bright-dark mixing, again in strong contrast with CdSe QDs. We emphasize that the absence of bright-dark mixing in ensembles of colloidal InP/ZnS NCs represents an unprecedented situation that can only be found at the single dot level[29,30] or in epitaxially grown nanostructures.[43]

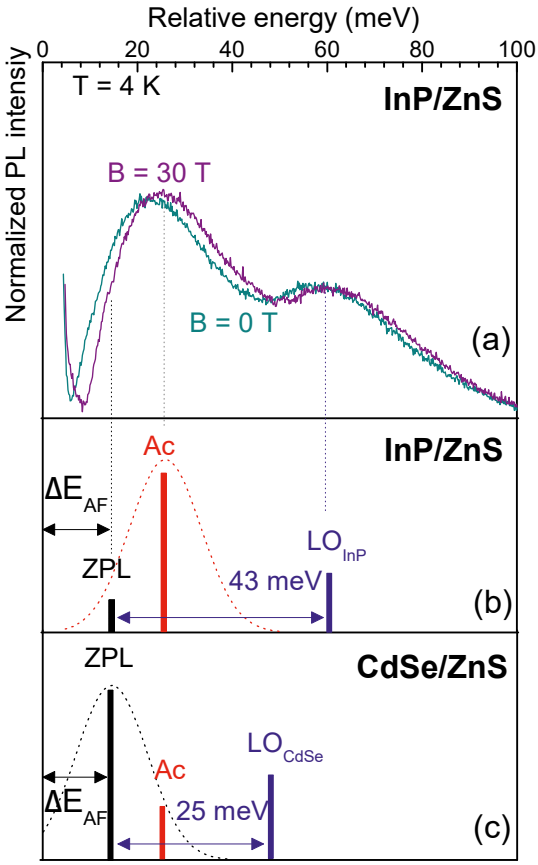

Figure 4.1. Energy peak in fluorescence line-narrowing (FLN) spectra. a) Unpolarized FLN spectra of InP/ZnS NC at 4 K in absence of magnetic fields and at 30 T. The state at 2.1 eV (the excitation laser energy) is taken as reference and set to 0 meV. b) Model of the FLN spectra in InP/ZnS. The blue mark corresponds to the 1 LO line and is shifted from the ZPL of the dark exciton by 43 meV. The black mark is shifted from the laser line by the bright dark splitting. The red mark represents the acoustic phonon sideband. c) Analogue model of the FLN spectra in CdSe/ZnS.

Figure 4.2 presents the PL decay in zero field and at 15 T. Up to 15 T magnetic field the PL decay and the total integrated photoluminescence do not change substantially, in agreement with the absence of magnetic field-induced bright-dark mixing. There is a slight slow down of the PL decay with the time constant going from 850 ns at 0 T to 1100 ns at 1-2 T, after which the decay time remains constant (Figure 4.2b). Figure A4.5 (Appendix) shows the same behavior for other InP/ZnS samples up to 30 tesla. A constant PL decay is expected only for the magnetic field strictly parallel to the q-axis of a given nanocrystal; in this case only Zeeman splitting can occur. For instance, in the case of single CdSe NCs, it was shown that an angle of 25° between the magnetic field and the q-axis of the nanocrystal is enough to induce a bright-dark mixing.[29] In marked contrast with this, we observe for InP QDs a complete absence of shortening of the PL decay in an ensemble measurement. This is also found for other InP core/shell systems, *e.g.* InP/ZnSe and

InP/(Cd,Zn)Se (Appendix, Figure A4.6). We must conclude that the optical properties of InP/ZnS NCs in a magnetic field are compelled by the Zeeman interaction only. This opens new perspectives in the study of magnetic field-induced polarization, spin dynamics and g-factors of exciton states.

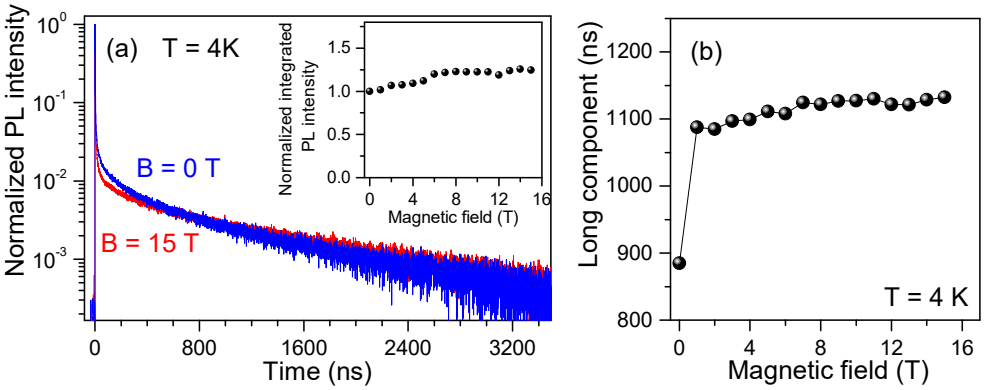

Figure 4.2. Unpolarized PL decay at T = 4 K: a) of ensemble of InP/ZnS nanocrystals (sample 1) at 0 T and 15 T. Inset: Magnetic field dependence of the normalized integrated PL intensity. b) Long component as a function of the magnetic field from 0 to 10 T. Solid line is guide for the eyes.

Figure 4.3a shows the polarization-resolved PL spectra of σ^+ (red) and σ^- (blue) circular polarization emission, of the same InP/ZnS sample at a magnetic field of 15 T, together with the spectrally resolved DCP. At 0 T (black) the emission is unpolarized. Similarly to other colloidal nanostructures, also in InP/ZnS NCs the degree of time-integrated circular polarization [DCP $=(I_{\sigma^+}-I_{\sigma^-})/(I_{\sigma^+}+I_{\sigma^-})$] is negative, which indicates a dominant contribution of σ^- polarization in magnetic field.[25–27,31,44] We observe a strong spectral dependence of the DCP: the high energy part of the PL spectrum has a DCP two times larger than the low energy part (Figure 4.3a). This large difference arises from the difference in the origin of the photon emitted in the low and high energy part of the PL spectra. Following a previous analysis[29] the high energy photons are emitted from an exciton state about 100 meV above the bright-dark doublet (inset Figure 4.3b). Figure 4.3c shows the magnetic field dependence of the DCP at high (green) and low (orange) emission energy, corresponding to the upper bright and dark exciton recombination, respectively. Surprisingly, there is only a weak DCP around – 0.35 (– 0.16) at B = 15 T for the high (low) energy part of the PL spectrum. In principle, a rise of the DCP up to –1 could be expected in the framework of pure Zeeman interactions in spherical zinc blende nanocrystals. These results are in agreement with the spectrally integrated DCP of the InP/ZnS samples measured up to 30 T, and with other InP core/shell samples, shown in Appendix Figures A4.7 – A4.8. It is noteworthy that such low DCP values have been observed also in ensembles of randomly oriented of CdSe[25,27,31] and CdTe[23,45] QDs. The DCP being much lower than 1 has been attributed to the shape of the nanocrystals,[23,45] long spin dynamics,[26] or the nature of the recombination mechanism of the dark exciton.[25,46]

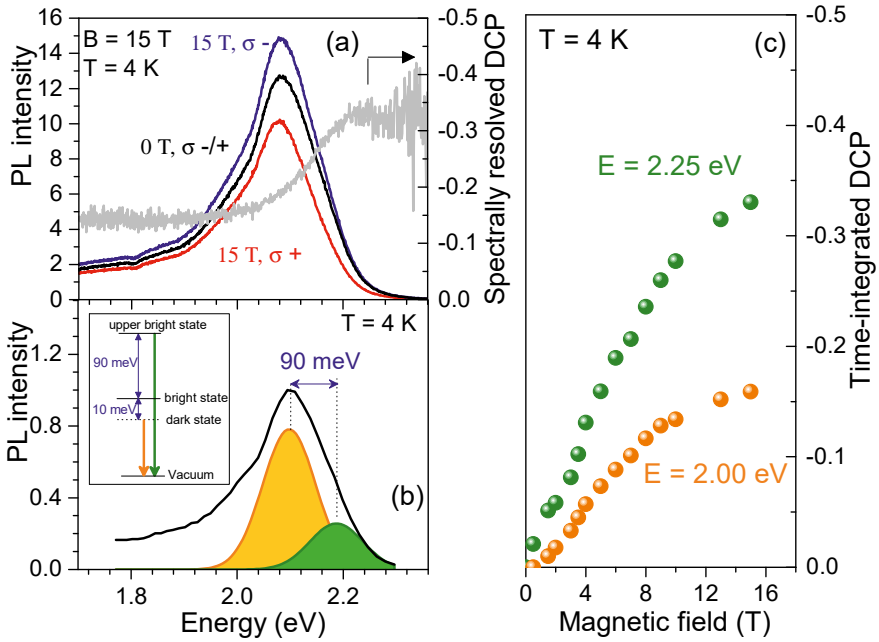

Figure 4.3. Polarizes emission of InP/ZnS NCs at T = 4 K. a) Polarization resolved PL spectra for magnetic field B = 0 T and 15 T together with the spectrally resolved DCP (light grey). b) Same PL spectrum at 0 T (black) with the highlighted contribution in the PL spectrum of the upper bright state (green) and the bright-dark doublet (orange). Inset: detailed exciton fine structure involved in the PL emission (adapted from ref. 33). c) Magnetic field dependence of the DCP at the spectral position of the upper bright state (green) and the bright-dark doublet (orange).

The non-linear rise of the DCP between 0 and 8 tesla (Fig. 4.3c) suggests that the spin relaxation time τ_S, between the Zeeman sublevels must be comparable to the radiative recombination time of the exciton, τ_R.[26,47] In order to get deeper insight into the spin dynamics, we studied the time-resolved degree of circular polarization (TRDCP). Figure 4.4a shows the polarization-resolved PL decay at 15 T at the PL maximum (E_{det} = 2.1 eV) together with the corresponding TRDCP. We clearly see that the buildup of the spin polarization occurs on two markedly different time scales. The fast initial rise occurs in 24 ns, while the relaxation to the saturation level P_{sat} = –0.27 is achieved in 400 ns. The origin of the spin dynamics can hardly be unveiled from the TRDCP at the PL maximum, since bright, dark and higher exciton states (Figure 4.3b) contribute to the PL signal.[33]

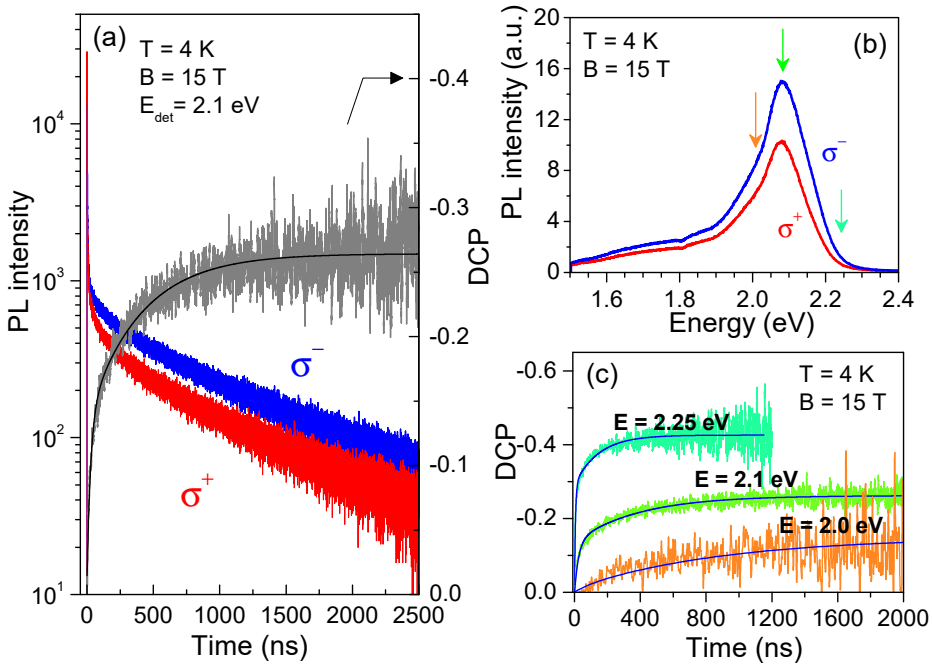

Figure 4.4. Time-resolved measurement of ensemble of InP/ZnS at T = 4.2 K. a) Time-resolved PL decay at the maximum of the PL (green arrow in panel b) at B = 15 T of σ^- (blue) and σ^+ (red) polarization together with the time-resolved DCP (grey). Solid line is fitting with two exponential growth with time constant τ_{short} = 24 ns and τ_{long} = 400 ns. b) Corresponding polarization resolved PL spectra. c) Time-resolved DCP at various spectral position (corresponding to the colored arrows in panel b).

The spectral dependence of the TRDCP allows to separate the various contributions: the low energy part of the spectrum results only from the radiative recombination of the dark exciton (Figure 4.4b, orange arrow at 2.00 eV), while the high energy part mostly results from the higher bright state (Figure 4.4b, blue arrow at 2.25 eV). The TRDCP measured at E = 2.00 eV (Figure 4.4c) directly shows the spin dynamics of the dark ground exciton, which can be well reproduced by a single exponential function with a spin relaxation time of ~ 400 ns. This is several orders of magnitude longer than in an ensemble of CdSe-based NCs.[27,35] The slow spin dynamics can, in principle, be due to the spin relaxation between the dark exciton Zeeman levels $F = +2$ and $F = -2$ which requires a simultaneous spin flip of the electron and the hole. We emphasize that the slow spin dynamics observed for InP QDs is in line with the absence of magnetic field induced bright-dark mixing. This is in firm contrast to the case of CdSe QDs where a fast spin relaxation time goes hand-in-hand with bright-dark mixing.[29]

By contrast, the TRDCP at high energy (E = 2.25 eV) shows that the spin thermalization is achieved mostly within 6 ns. This fast spin dynamics can be attributed to the relaxation from an upper bright state which requires only one charge carrier spin-flip, that occur on considerably faster time scales than the concomitant flip of the electron and hole spin. Note that the remaining long component in the TRDCP is likely due to residual

contribution of the dark exciton line (Figure 4.3b). It is noteworthy that this inter level spin-flip time of ~6 ns is significantly longer under magnetic field than those previously reported at 0 T where a spin relaxation time of 700 ps was measured.[33]

4.2.2 Absence of magnetic field induced bright-dark mixing

Above, we presented results that show that a magnetic field does not mix the forbidden dark and bright states in InP QDs with ZnS shells, and that this is also the case when the shell is ZnSe or (Zn,Cd)Se. This is rather unique, and in strong contrast with, for instance, CdSe-based QDs.[25,27,48] According to the existing theory, bright-dark mixing is absent when the magnetic field is parallel to a high-symmetry axis.[22] Such a situation has occasionally been observed in single-dot photoluminescence spectroscopy.[29,30] But in an ensemble the symmetry axes are randomly oriented, and bright-dark mixing should occur. Following commonly used effective-mass theory, the mixing appears because the off-diagonal terms in the Hamiltonian are non-zero when the magnetic field is not strictly parallel to the q-axis.[22,49] The only alternative to cancel these terms lays in the vanishing of the matrix element which couples the excitonic states. Theoretical calculations, which go beyond the scope of this thesis, are required to determine the analytical expression of these matrix elements. We emphasize that FLN and PL decay results on InP/ZnSe and InP/(Zn,Cd)Se NCs also report an absence of bright-dark mixing (see chapters 3 and 6).[42] The lack of bright-dark mixing in InP NCs has important consequences, such as the ability to study spin physics in an ensemble that would normally only be possible with a single quantum dot. A striking example is the lengthening of the long-living component of the PL decay with increasing the magnetic field. This has only been observed on single CdSe NCs, where the magnetic field was applied almost along the q-axis.[29] To explain this, it was assumed that a bright-dark mixing is induced by an intrinsic magnetic field (perpendicular to the q-axis) arising from magnetic defects in the NC. [29]

4.2.3 The weak degree of circular polarization in magnetic field

Compared to CdSe NCs, the saturation level of the DCP in InP/ZnS NCs is much lower, especially in the low energy part of the PL spectra, which is dominated by the dark exciton recombination. The low DCP values could be caused by several effects. First, a small dark exciton g-factor prevents the buildup of a spin population since the Zeeman splitting $g\mu_B B$ can be smaller than the thermal energy down to low temperature. While values around -0.75 are expected, we measured only saturation at about -0.16. It is noteworthy that the theoretical value only assumes that the dark $|\pm 2\rangle$ state couples to the bright $|\pm 1^{U,L}\rangle$ and therefore inherit its polarization properties. However, as shown by Rodina et al., the dark exciton state, $|\pm 2\rangle$, can couple to the $|0^U\rangle$ through acoustic phonons.[49] This coupling is notably responsible for the low DCP values in CdSe/CdS dot-in-rod nanostructures.[25] In the case of a lack of bright dark mixing and a dominant coupling to acoustic phonons, as observed in InP/ZnS NCs, the dark exciton polarization properties will be given by the $|0^U\rangle$ state, which shows linear polarization. This explains the low DCP values observed here in InP/ZnS as well as in InP/ZnSe NCs and in a previous report by Langof et al.[50]

4.3 Conclusion

The optical properties of InP/ZnS core/shell NCs under magnetic fields show a marked difference compared to II-VI nanocrystals. In particular, in fluorescence line narrowing spectra, the dark exciton zero-phonon line can hardly be observed and emission is mainly assisted by acoustic phonons. Moreover, the insensitivity of FLN spectra and PL decay to magnetic fields demonstrate a lack of bright-dark mixing. In line with this, the time-resolved DCP related to the dark exciton shows a very slow spin relaxation time indicating that a simultaneous spin-flip of both the electron and the hole is required to build-up the spin population. This unprecedented situation allows for unveiling mechanisms involved in the dark exciton radiative recombination. Our results show the richness of the spin physics in III-V colloidal nanostructures. We believe that they will stimulate future research on InP-based nanocrystal opto-electronics.

4.4 Methods

Sample preparation. InP/ZnS, InP/ZnSe and InP/(Zn,Cd)Se core/shell QD samples were synthesized, following the method reported in ref. 15. The QD samples were washed by precipitation with methanol, isolated by centrifugation and redispersed in octadecene. To achieve a QDs film the solution was deposited using a *drop-cast* method, on crystalline silicon substrate for FLN measurements, and on a quartz substrate for PL and TrPL measurements.

PL and Time-resolved Photoluminescence (TrPL). The Time-resolved PL (TrPL) and polarized PL measurements were performed on QD films deposited on quartz substrates (see sample preparation above).

In the Time-resolved PL measurements the excitation was provided by a picosecond pulsed diode-laser operating at 405 nm. The same repetition rate (125 kHz) was used for all samples and controlled by the laser driver internal clock. The average count rate was kept at 3% of the laser repetition rate. This low excitation fluence was used in order to maintain single photon statistics and avoid multiexciton formation. The TrPL signal of the QDs ensemble was spectrally integrated on all the wavelengths. The PL signal was detected by an avalanche photo diode connected to a single-photon counter (time-correlated single photon counting).

Polarized PL measurements were performed in static (and time resolved) configuration, using the same excitation source, in continuous or pulse wave mode. The excitation was circularly polarized with the use of a linear polarizer and a Babinet Soleil compensator. The PL light was guided through a single grating spectrometer (300 grooves/mm grating) and detected by a liquid nitrogen cooled charge couple device (CCD) in the in static configuration and by an avalanche photo diode connected to a single-photon counter (time-correlated single photon counting) in the time resolved configuration. The emitted photons were detected in crossed and co-polarization relative to the laser polarization by

using a linear polarizer and a lambda-quarter wave plate. Cut-off optical filters were used in excitation and detection, for both PL and TRPL experiments.

Fluorescence Line-Narrowing (FLN) measurements. For these experiments the samples used were QD in glass cuvettes or in films on crystalline silicon substrate (see sample preparation). The samples in film were mounted in a titanium sample holder on top of a three-axis piezo-positioner. The FLN measurements were performed using a narrow excitation source, achieved by using a tunable jet-stream dye (Rhodamine 6G) laser. This monochromatic laser beam was circularly polarized by means of a linear polarizer and a Babinet-Soleil compensator. The laser beam was focused on the sample by a singlet lens (10 mm focal length). The same lens was used to collect the PL emission and direct it to the detection setup (Backscattering geometry). The samples and optical probe were mounted inside a liquid-helium bath cryostat. The FLN signal was guided through a 0.3 m long single grating spectrometer (300 grooves/mm grating) and detected by a liquid nitrogen cooled charge couple device (CCD). The emitted photons were detected in crossed polarization relative to the laser polarization by using a linear polarizer and a lambda-quarter wave plate. Cut-off optical filters were used in excitation and detection.

ACKNOWLEDGMENT: We acknowledge the support of the HFML-RU/FOM, member of the European Magnetic Field Laboratory (EMFL).

4.5 References

1 Zhou, J.; Liu, Y.; Tang, J.; Tang, W. Surface Ligands Engineering of Semiconductor Quantum Dots for Chemosensory and Biological Applications. *Mater. Today* **2017**, *20*, 360–376.

2 Lacroix, L.-M.; Delpech, F.; Nayral, C.; Lachaize, S.; Chaudret, B. New Generation of Magnetic and Luminescent Nanoparticles for in Vivo Real-Time Imaging. *Interface Focus* **2013**, *3*, 1–19.

3 Walling, M.; Novak, J.; Shepard, J. R. E. Quantum Dots for Live Cell and In Vivo Imaging. *Int. J. Mol. Sci.* **2009**, *10*, 441–491.

4 Ippen, C.; Greco, T.; Wedel, A. InP/ZnSe/ZnS: A Novel Multishell System for InP Quantum Dots for Improved Luminescence Efficiency and Its Application in a Light-Emitting Device. *J. Inf. Disp.* **2012**, *13*, 91–95.

5 Wood, V.; Panzer, M. J.; Chen, J.; Bradley, M. S.; Halpert, J. E.; Bawendi, M. C.; Bulović, V. Inkjet-Printed Quantum Dot-Polymer Composites for Full-Color AC-Driven Displays. *Adv. Mater.* **2009**, *21*, 2151–2155.

6 Shirasaki, Y.; Supran, G. J.; Bawendi, M. G.; Bulović, V. Emergence of Colloidal Quantum-Dot Light-Emitting Technologies. *Nat. Photonics* **2013**, *7*, 13–23.

7 Lim, J.; Jun, S.; Jang, E.; Baik, H.; Kim, H.; Cho, J. Preparation of Highly Luminescent Nanocrystals and Their Application to Light-Emitting Diodes. *Adv. Mater.* **2007**, *19*, 1927–1932.

8 Foucher, C.; Guilhabert, B.; Laurand, N.; Dawson, M. D. Wavelength-Tunable Colloidal Quantum Dot Laser on Ultra-Thin Flexible Glass. *Appl. Phys. Lett.* **2014**, *104*, 1–5.

9 Samuel, I. Colloidal Nanocrystals: Electrifying Quantum Dots for Lasers. *Nat. Mater.* **2017**, *17*, 9–10.

10 Shen, H.; Cao, W.; Shewmon, N. T.; Yang, C.; Li, L. S.; Xue, J. High-Efficiency, Low Turn-on Voltage Blue-Violet Quantum-Dot-Based Light-Emitting Diodes. *Nano Lett.* **2015**, *15*, 1211–1216.

11 Chen, O.; Wei, H.; Maurice, A.; Bawendi, M.; Reiss, P. Pure Colors from Core–shell Quantum Dots. *MRS Bull.* **2013**, *38*, 696–702.

12 Bourzac, K. Quantum Dots Go on Display. *Nature* **2013**, *493*, 283–283.

13 Choi, M. K.; Yang, J.; Kang, K.; Kim, D. C.; Choi, C.; Park, C.; Kim, S. J.; Chae, S. I.; Kim, T.-H.; Kim, J. H.; *et al.* Wearable Red–green–blue Quantum Dot Light-Emitting Diode Array Using High-Resolution Intaglio Transfer Printing. *Nat. Commun.* **2015**, *6*, 7149.

14 Yang, Y.; Zheng, Y.; Cao, W.; Titov, A.; Hyvonen, J.; Manders, J. R.; Xue, J.; Holloway, P. H.; Qian, L. High-Efficiency Light-Emitting Devices Based on Quantum Dots with Tailored Nanostructures. *Nat. Photonics* **2015**, *9*, 259–266.

15 Tessier, M. D.; Dupont, D.; De Nolf, K.; De Roo, J.; Hens, Z. Economic and Size-Tunable Synthesis of InP/ZnE (E = S, Se) Colloidal Quantum Dots. *Chem. Mater.* **2015**, *27*, 4893–4898.

16 Qu, L.; Peng, X. Control of Photoluminescence Properties of CdSe Nanocrystals in Growth. *J. Am. Chem. Soc.* **2002**, *124*, 2049–2055.

17 Chen, O.; Zhao, J.; Chauhan, V. P.; Cui, J.; Wong, C.; Harris, D. K.; Wei, H.; Han, H.-S.; Fukumura, D.; Jain, R. K.; *et al.* Compact High-Quality CdSe–CdS Core–shell Nanocrystals with Narrow Emission Linewidths and Suppressed Blinking. *Nat. Mater.* **2013**, *12*, 445–451.

18 Cui, J.; Beyler, A. P.; Bischof, T. S.; Wilson, M. W. B.; Bawendi, M. G. Deconstructing the Photon Stream from Single Nanocrystals: From Binning to Correlation. *Chem. Soc. Rev.* **2014**, *43*, 1287–1310.

19 Cui, J.; Beyler, A. P.; Marshall, L. F.; Chen, O.; Harris, D. K.; Wanger, D. D.; Brokmann, X.; Bawendi, M. G. Direct Probe of Spectral Inhomogeneity Reveals Synthetic Tunability of Single-Nanocrystal Spectral Linewidths. *Nat. Chem.* **2013**, *5*, 602–606.

20 Chandrasekaran, V.; Tessier, M. D.; Dupont, D.; Geiregat, P.; Hens, Z.; Brainis, E. Nearly Blinking-Free, High-Purity Single-Photon Emission by Colloidal InP/ZnSe Quantum Dots. *Nano Lett.* **2017**, *17*, 6104–6109.

21 Nirmal, M.; Norris, D. J.; Kuno, M.; Bawendi, M. G.; Efros, A. L.; Rosen, M. Observation of the "Dark Exciton" in CdSe Quantum Dots. *Phys. Rev. Lett.* **1995**, *75*, 3728–3731.

22 Efros, A.; Rosen, M.; Kuno, M.; Nirmal, M.; Norris, D.; Bawendi, M. Band-Edge Exciton in Quantum Dots of Semiconductors with a Degenerate Valence Band: Dark and Bright Exciton States. *Phys. Rev. B* **1996**, *54*, 4843–4856.

23 Blokland, J. H.; Claessen, V. I.; Wijnen, F. J. P.; Groeneveld, E.; de Mello Donegá, C.; Vanmaekelbergh, D.; Meijerink, A.; Maan, J. C.; Christianen, P. C. M. Exciton Lifetimes of CdTe Nanocrystal Quantum Dots in High Magnetic Fields. *Phys. Rev. B* **2011**, *83*, 35304.

24 Louyer, Y.; Biadala, L.; Trebbia, J.-B.; Fernée, M. J.; Tamarat, P.; Lounis, B. Efficient Biexciton Emission in Elongated Cdse/Zns Nanocrystals. *Nano Lett.* **2011**, *11*, 4370–4375.

25 Siebers, B.; Biadala, L.; Yakovlev, D. R.; Rodina, A. V; Aubert, T.; Hens, Z.; Bayer, M. Exciton Spin Dynamics and Photoluminescence Polarization of CdSe/CdS Dot-in-Rod Nanocrystals in High Magnetic Fields. *Phys. Rev. B - Condens. Matter Mater. Phys.* **2015**, *91*, 155304.

26 Liu, F.; Biadala, L.; Rodina, A. V.; Yakovlev, D. R.; Dunker, D.; Javaux, C.; Hermier, J.-P.; Efros, A. L.; Dubertret, B.; Bayer, M. Spin Dynamics of Negatively Charged Excitons in CdSe/CdS Colloidal Nanocrystals. *Phys. Rev. B* **2013**, *88*, 35302.

27 Furis, M.; Hollingsworth, J. A.; Klimov, V. I.; Crooker, S. A. Time- and Polarization-Resolved Optical Spectroscopy of Colloidal CdSe Nanocrystal Quantum Dots in High Magnetic Fields. *J. Phys. Chem. B* **2005**, *109*, 15332–15338.

28 Wijnen, F. J. P.; Blokland, J. H.; Chin, P. T. K.; Christianen, P. C. M.; Maan, J. C. Competition between Zero-Phonon and Phonon-Assisted Luminescence in Colloidal CdSe Quantum Dots. *Phys. Rev. B - Condens. Matter Mater. Phys.* **2008**, *78*.

29 Biadala, L.; Louyer, Y.; Tamarat, P.; Lounis, B. Band-Edge Exciton Fine Structure of Single CdSe/ZnS Nanocrystals in External Magnetic Fields. *Phys. Rev. Lett.* **2010**, *105*, 157402.

30 Louyer, Y.; Biadala, L.; Trebbia, J.-B.; Fernée, M. J.; Tamarat, P.; Lounis, B. Efficient Biexciton Emission in Elongated CdSe/ZnS Nanocrystals. *Nano Lett.* **2011**, *11*, 4370–4375.

31 Wijnen, F. J. P.; Blokland, J. H.; Chin, P. T. K.; Christianen, P. C. M.; Maan, J. C. Competition between Zero-Phonon and Phonon-Assisted Luminescence in Colloidal CdSe Quantum Dots. *Phys. Rev. B* **2008**, *78*, 235318.

32 Labeau, O.; Tamarat, P.; Lounis, B. Temperature Dependence of the Luminescence Lifetime of Single CdSe/ZnS Quantum Dots. *Phys. Rev. Lett.* **2003**, *90*, 257404.

33 Biadala, L.; Siebers, B.; Beyazit, Y.; Tessier, M. D.; Dupont, D.; Hens, Z.; Yakovlev, D. R.; Bayer, M. Band-Edge Exciton Fine Structure and Recombination Dynamics in InP/ZnS Colloidal Nanocrystals. *ACS Nano* **2016**, *10*, 3356–3364.

34 Granados del Águila, A.; Jha, B.; Pietra, F.; Groeneveld, E.; de Mello Donegá, C.; Maan, J. C.; Vanmaekelbergh, D.; Christianen, P. C. M. Observation of the Full Exciton and Phonon Fine Structure in CdSe/CdS Dot-in-Rod Heteronanocrystals. *ACS Nano* **2014**, *8*, 5921–5931.

35 Liu, F.; Biadala, L.; Rodina, A. V.; Yakovlev, D. R.; Dunker, D.; Javaux, C.; Hermier, J.-P.; Efros, A. L.; Dubertret, B.; Bayer, M. Spin Dynamics of Negatively Charged Excitons in CdSe/CdS Colloidal Nanocrystals. *Phys. Rev. B* **2013**, *88*, 35302.

36 Biadala, L.; Liu, F.; Tessier, M. D.; Yakovlev, D. R.; Dubertret, B.; Bayer, M. Recombination Dynamics of Band Edge Excitons in Quasi-Two-Dimensional CdSe Nanoplatelets. *Nano Lett.* **2014**, *14*, 1134–1139.

37 Shornikova, E. V.; Biadala, L.; Yakovlev, D. R.; Sapega, V. F.; Kusrayev, Y. G.; Mitioglu, A. A.; Ballottin, M. V.; Christianen, P. C. M.; Belykh, V. V.; Kochiev, M. V.; *et al.* Addressing the Exciton Fine Structure in Colloidal Nanocrystals: The Case of CdSe Nanoplatelets. *Nanoscale* **2018**, *10*.

38 Bertram, D.; Mićić, O.; Nozik, A. Excited-State Spectroscopy of InP Quantum Dots. *Phys. Rev. B* **1998**, *57*, R4265–R4268.

39 Mic, O. I.; Cheong, H. M.; Fu, H.; Zunger, a; Sprague, J. R.; Mascarenhas, a; Nozik, a J. Size-Dependent Spectroscopy of InP Quantum Dots. *J. Phys. Chem. B* **1997**, *5647*, 4904–4912.

40 Seong, M. J.; Mićić, O. I.; Nozik, A. J.; Mascarenhas, A.; Cheong, H. M. Size-Dependent Raman Study of InP Quantum Dots. *Appl. Phys. Lett.* **2003**, *82*, 185–187.

41 Hou, H. J.; Kong, F. J. Theoretical Investigation on the Structural, Dynamical, and Thermodynamic Properties of the Zinc-Blende InX (X = P, As, Sb). *Phys. status solidi* **2011**, *248*, 1399–1404.

42 Brodu, A.; Ballottin, M. V.; Buhot, J.; Van Harten, E. J.; Dupont, D.; La Porta, A.; Prins, P. T.; Tessier, M. D.; Versteegh, M. A. M.; Zwiller, V.; *et al.* Exciton Fine Structure and Lattice Dynamics in InP/ZnSe Core/Shell Quantum Dots. *ACS Photonics* **2018**, *5*, 3353–3362.

43 Bayer, M.; Ortner, G.; Stern, O.; Kuther, A.; Gorbunov, A.; Forchel, A.; Hawrylak, P.; Fafard, S.; Hinzer, K.; Reinecke, T.; *et al.* Fine Structure of Neutral and Charged Excitons in Self-Assembled In(Ga)As/(Al)GaAs Quantum Dots. *Phys. Rev. B* **2002**, *65*, 195315.

44 Canneson, D.; Shornikova, E. V.; Yakovlev, D. R.; Rogge, T.; Mitioglu, A. A.; Ballottin, M. V.; Christianen, P. C. M.; Lhuillier, E.; Bayer, M.; Biadala, L. Negatively Charged and Dark Excitons in CsPbBr 3 Perovskite Nanocrystals Revealed by High Magnetic Fields. *Nano Lett.* **2017**, *17*, 6177–6183.

45 Liu, F.; Rodina, A. V.; Yakovlev, D. R.; Greilich, A.; Golovatenko, A. A.; Susha, A. S.; Rogach, A. L.; Kusrayev, Y. G.; Bayer, M. Exciton Spin Dynamics of Colloidal CdTe Nanocrystals in Magnetic Fields. *Phys. Rev. B* **2014**, *89*, 115306.

46 Rodina, A. V.; Efros, A. L. Radiative Recombination from Dark Excitons in Nanocrystals: Activation Mechanisms and Polarization Properties. *Phys. Rev. B* **2016**, *93*, 155427.

47 Javaux, C.; Mahler, B.; Dubertret, B.; Shabaev, A.; Rodina, A. V; Efros, A. L.; Yakovlev, D. R.; Liu, F.; Bayer, M.; Camps, G.; *et al.* Thermal Activation of Non-Radiative Auger Recombination in Charged Colloidal Nanocrystals. *Nat. Nanotechnol.* **2013**, *8*, 206–212.

48 Nirmal, M.; Norris, D. J.; Kuno, M.; Bawendi, M. G.; Efros, A. L.; Rosen, M. Observation of The "dark Ection" in CdSe Quantum Dots. **1995**, *75*, 3728–3731.

49 Rodina, A. V; Efros, A. L. Radiative Recombination from Dark Excitons in Nanocrystals : Activation Mechanisms and Polarization Properties. *Phys. Rev. B* **2016**, *93*, 155427.

50 Langof, L.; Fradkin, L.; Ehrenfreund, E.; Lifshitz, E.; Micic, O. I.; Nozik, A. J. Colloidal InP/ZnS Core-Shell Nanocrystals Studied by Linearly and Circularly Polarized Photoluminescence. *Chem. Phys.* **2004**, *297*, 93–98.

4.6 Appendix

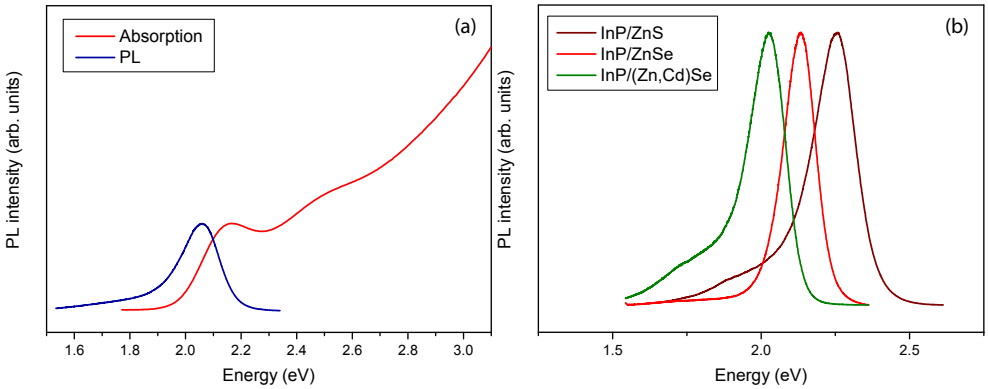

Figure A4.1: a) Absorption (red) and PL (blue) spectra for InP/ZnS NCs (sample 2) investigated at High Field Magnet Laboratory (Radboud University, Nijmegen, The Netherlands). b) PL spectra of InP/ZnS with a 2.5 nm InP core diameter (brown), InP/ZnSe (red) and InP/$Cd_{0.09}Zn_{0.91}Se$ (green) NC samples, used for comparison.

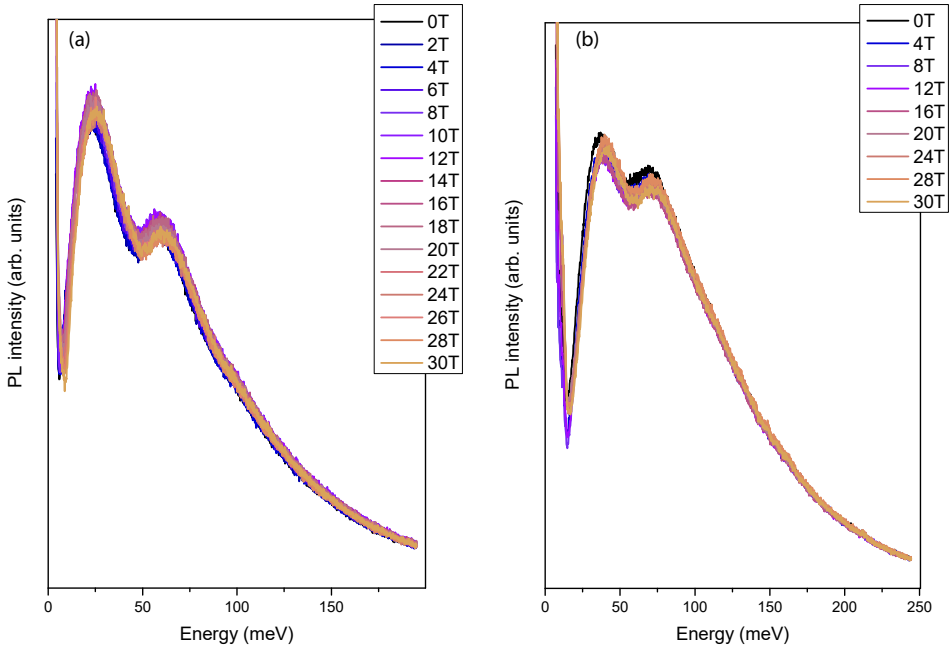

Figure A4.2: Unpolarized fluorescence line-narrowing (FLN) spectroscopy at 4 K at variable magnetic fields from 0 to 30 T, with samples measured in cuvette. a) Spectra of the InP/ZnS sample 1, upon excitation at 2.1 eV. b) Spectra of a InP/ZnS sample (with a 2.5 nm InP core diameter), upon excitation at 2.3 eV. The excitation laser energy is taken as reference and set to 0 meV.

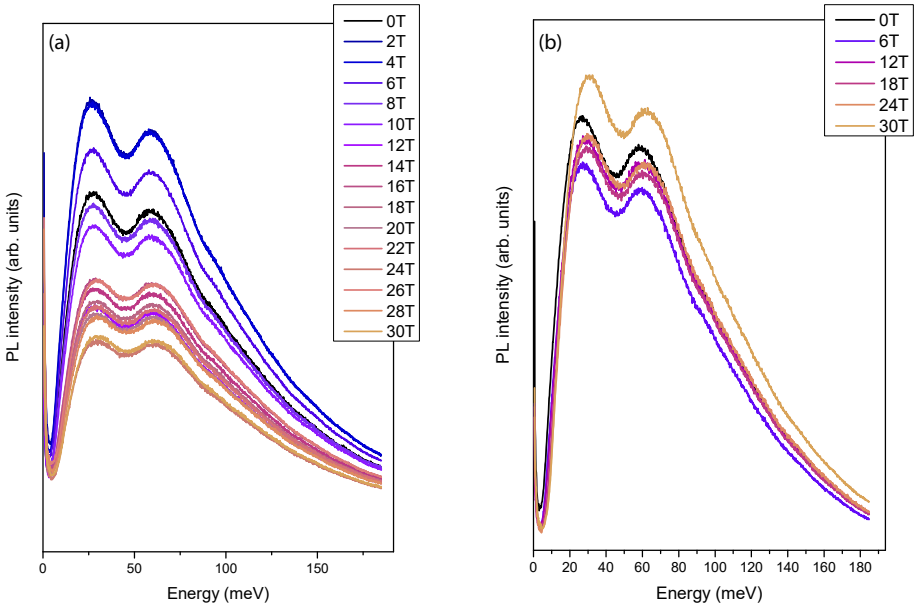

Figure A4.3: Fluorescence line-narrowing (FLN) spectroscopy at 4 K at variable magnetic fields from 0 to 30 T, for the sample 1 measured in film, upon excitation at 2.1 eV. a) Excitation with σ^- light and detection of the σ^+ emission. b) Excitation with σ^+ light and detection of the σ^- emission. The different polarizations affect the emission intensity, but it is not systematically enhanced upon rising the magnetic field, in agreement with the absence of magnetic field induced bright-dark mixing.

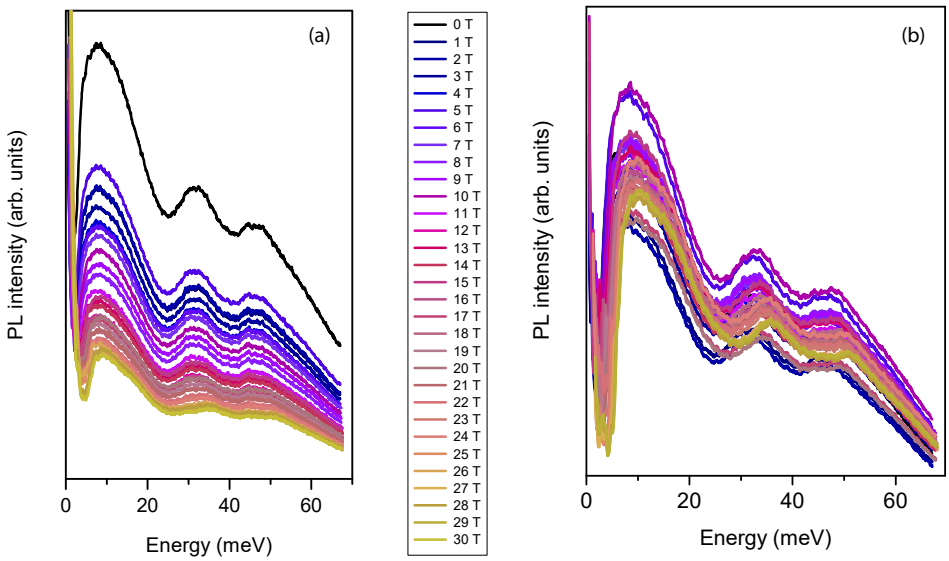

Figure A4.4: Fluorescence line-narrowing (FLN) spectroscopy at 4 K at variable magnetic fields from 0 to 30 T, for an InP/ZnSe sample with 3.1 nm InP core diameter, measured in film, upon excitation at 2.0 eV. a) Excitation with σ^- light and detection of the σ^+ emission. b) Excitation with σ^+ light and detection of the σ^- emission. Same trend also for InP core NCs with different shells.

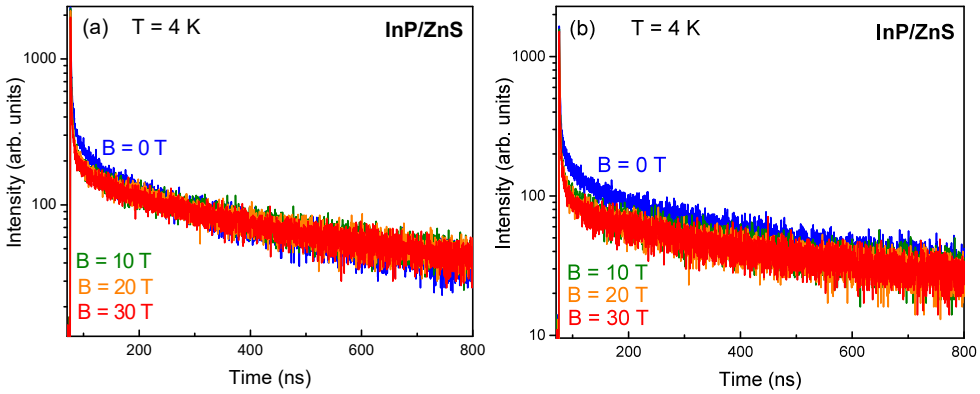

Figure A4.5: Unpolarized PL decay at 0 T, 10 T, 20 T and 30 T at T = 4 K: a) of ensemble of InP/ZnS nanocrystals (sample 1), b) of a InP/ZnS sample (with a 2.5 nm InP core diameter).

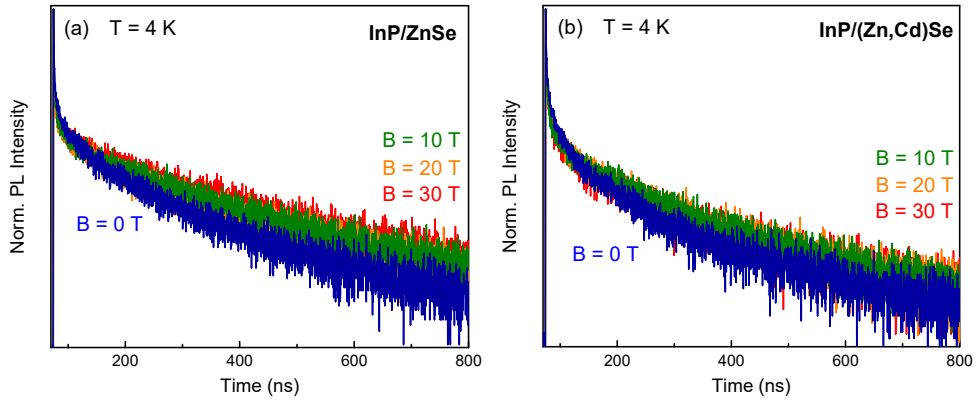

Figure A4.6: Unpolarized PL decay at 0 T, 10 T, 20 T and 30 T at T = 4 K: a) of ensemble of InP/ZnSe nanocrystals, b) of ensemble of a InP/(Zn,Cd)Se nanocrystals with 9% Cd content.

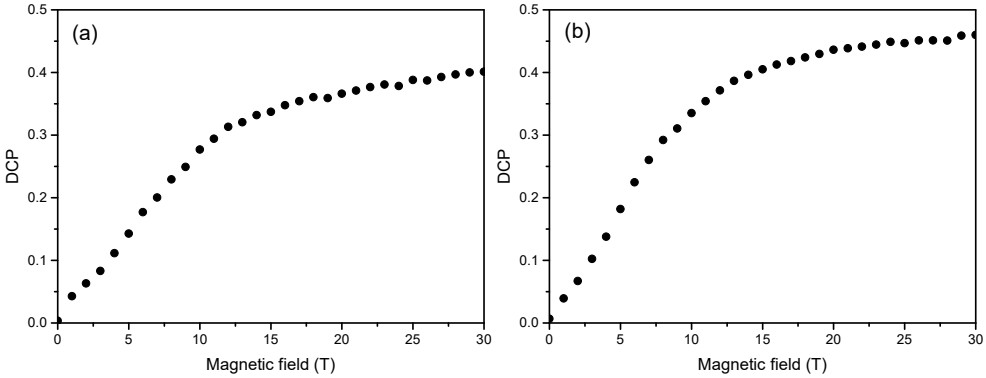

Figure A4.7: Magnetic field dependence of the spectrally integrated DCP: a) of ensemble of InP/ZnS nanocrystals (sample 1), b) of a InP/ZnS sample (with a 2.5 nm InP core diameter).

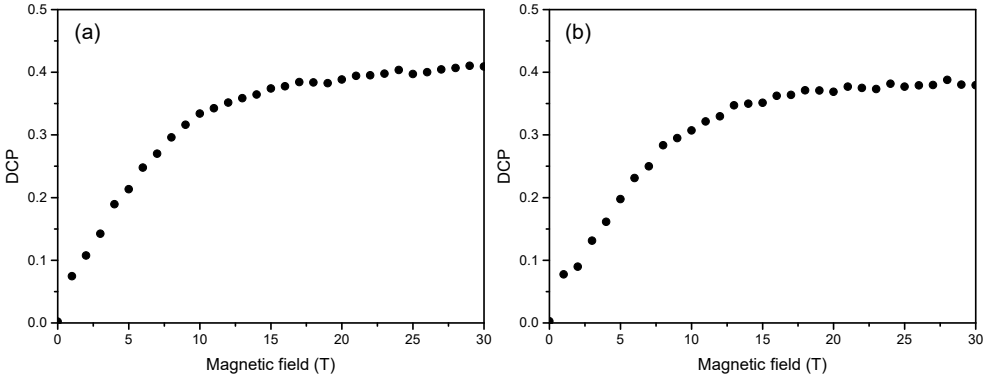

Figure A4.8: Magnetic field dependence of the spectrally integrated: a) of ensemble of InP/ZnSe nanocrystals, b) of ensemble of InP/(Zn,Cd)Se nanocrystals.

Chapter 5

Exciton–phonon coupling in InP quantum dots with ZnS and (Zn,Cd)Se shells

Based on:
Exciton–phonon coupling in InP quantum dots with ZnS and (Zn,Cd)Se shells.
Annalisa Brodu, Mariana V. Ballottin, Jonathan Buhot, Dorian Dupont, Mickael D. Tessier, Zeger Hens, Freddy T. Rabouw, Peter C. M. Christianen, Celso de Mello Donega, and Daniel Vanmaekelbergh.
Submitted.

Abstract

InP-based colloidal quantum dots are promising for optoelectronic devices such as LEDs and lasers. Understanding and optimizing their emission process is of scientific interest and essential for large-scale applications. Here we present a study of the exciton recombination dynamics in InP QDs with various shells: ZnS, ZnSe and (Zn,Cd)Se with different amounts of Cd (5%, 9%, 12%). Phonon energies extracted from Raman spectroscopy measurements at cryogenic temperatures (4-5 K) are compared with exciton emission peaks observed in fluorescence line narrowing (FLN) spectra. This allowed us to determine the position of both the bright $F = \pm 1$ state and the lowest dark $F = \pm 2$ state. We could identify the phonon modes involved in the radiative recombination of the dark state and found that acoustic and optical phonons of both the core and the shell are involved in this process. The Cd content in the shell increases electron wavefunction delocalization, and thereby enhances the exciton–phonon coupling through the Fröhlich interaction.

5.1 Introduction

Colloidal semiconductor nanocrystals (NCs) exhibit size-tunable narrow emission spectra in combination with broad absorption and excitation spectra. These characteristics make colloidal semiconductor NCs (often called quantum dots, QDs) of high interest in nanoscience and optoelectronic applications, such as lasers and LEDs (light-emitting diodes).[1–8] InP-based QDs have a high potential for opto-electronics because of their bright emission, ranging from 500 to 1000 nm,[9,10] with near-unity photoluminescence quantum yield.[11] The promise of large-scale applications of InP-based QDs requires a detailed optical characterization to determine the exciton recombination processes, including the exciton–phonon interaction.

In recent years, several studies have established that in II-VI semiconductor nanomaterials with zincblende structure and prolate shape, the degeneracy of the lowest exciton level is partially lifted due to the electron–hole exchange interaction and the shape asymmetry of the QDs.[12–17] This results in an exciton fine-structure that consists of five levels. The lowest-energy exciton state is referred to as a dark state because radiative recombination from it is forbidden within the electric-dipole approximation. This state is followed by a higher-energy 'bright' exciton state from which the radiative transition to the ground state is allowed.[16,17]

Several studies have reported effects of exciton–phonon coupling on the emission from the different exciton fine-structure levels. While most such studies focused on core-only QDs,[18–22] core/shell QDs are more relevant for applications. Usually in a core/shell geometry, a higher-bandgap material overcoats the core to protect it from fast oxidation and to increase the photoluminescence quantum yield by passivating surface defects. The shell can play a fundamental role in the exciton radiative recombination process. For instance, in core/shell QDs the electron (e) and hole (h) wavefunctions can be both localized in the core (type-I localization regime), or be spatially separated in the core and shell (type-II localization regime). An intermediate regime (type-I$^{1/2}$), in which one carrier is localized while the other is delocalized over the whole QD, is also possible.[23] In this way, the carrier localization regime can be tuned from type-I to type-II, which has important consequences for the exciton fine structure[15] and a number of properties, for example the photoluminescence (PL) and absorption spectra, phonon coupling, and blinking mechanism.[23–28] When the e and h wave functions are (partially) spatially separated (type-I½ or type-II regime), the exciton is polarized which increases coupling to lattice phonons via the Fröhlich interaction.[29–31] Despite the relevance of this, thorough studies of the exciton–phonon coupling in core/shell structures remain scarce.

Here, we present a study of the exciton–phonon coupling in InP-based QDs with various shells: ZnS, ZnSe and (Zn,Cd)Se with different amounts of Cd (5%, 9%, 12%). All samples have an InP QD core diameter of 3.0 ± 0.1 nm and a shell thickness that varies from 5 nm for the ZnS shell, to 7 nm for the (Zn,Cd)Se shells and PL quantum yields of about 60%.[9,24] We studied the exciton–phonon coupling using a combination of Raman spectroscopy and fluorescence line-narrowing (FLN) spectroscopy at 4 K. Raman spectra reveal the

phonon energies in these core/shell structures. FLN spectra show multiple emission peaks due to various emission pathways, which we assign to the involvement of several phonon modes.

We discuss the exciton states involved in the photoluminescence and the role of phonons in the recombination dynamics. Both acoustic and optical phonons of the core and shell are involved in the exciton recombination process and they play an important role in enhancing the radiative recombination rate of the dark state.

5.2 Results and discussion

5.2.1 Samples characterization

We studied five InP core/shell QD samples with comparable InP core of 3.0 ± 0.1 nm in diameter and various shells: ZnS, ZnSe and (Zn,Cd)Se with different Cd contents (5%, 9%, 12%). The InP QDs with ZnS and ZnSe shell were synthesized as described in ref. 9, and the ones with (Zn,Cd)Se shell as described in ref. 24. The samples were characterized by PL spectroscopy at room temperature (RT) and at 4 K, (Appendix, Figure A5.1). All samples emit in the visible range between 1.92 and 2.06 eV at RT, with the InP/ZnS QDs emitting at 1.99 eV, the InP/ZnSe QDs emitting at 2.06 eV, while the PL peak of the InP/(Cd,Zn)Se QDs shifts to lower energies with increasing Cd content, reaching 1.92 eV for 12% Cd. The full-width at half-maximum (FWHM) of the PL peaks ranges from 150 to 180 meV. The PL spectra show a considerable blueshift (about 60 meV for all samples) upon cooling to 4 K, due to the contraction of the crystal lattice.[32] The PL blueshift is accompanied by a decrease in the FWHM which ranges from 130 to 150 meV at 4 K.

5.2.2 Raman and FLN spectroscopy

We performed Raman spectroscopy to detect (Raman-active) phonons in the various InP core/shell QDs involved in this study. The phonon energies extracted from the Raman spectra were subsequently compared to results obtained from FLN spectroscopy, a size-selective technique that allows the observation of PL lines with reduced inhomogeneous line broadening. In FLN spectroscopy, a spectrally narrow *laser line* with energy matching the low-energy side of the absorption spectrum is used to resonantly excite a small sub-ensemble of the QDs. In other words, only the QDs with a high oscillator strength exciton state (bright state) that matches the energy of the excitation photons are excited. This size-selective excitation results in a minimally inhomogeneously broadened emission spectrum, revealing the fine structure of the lowest exciton states and their coupling to phonons. This allowed us to study the exciton–phonon coupling in our systems.[33] To reduce the thermal broadening contribution, the FLN and Raman measurements were performed at 4 K.

5.2.3 Phonons in InP/ZnS QDs

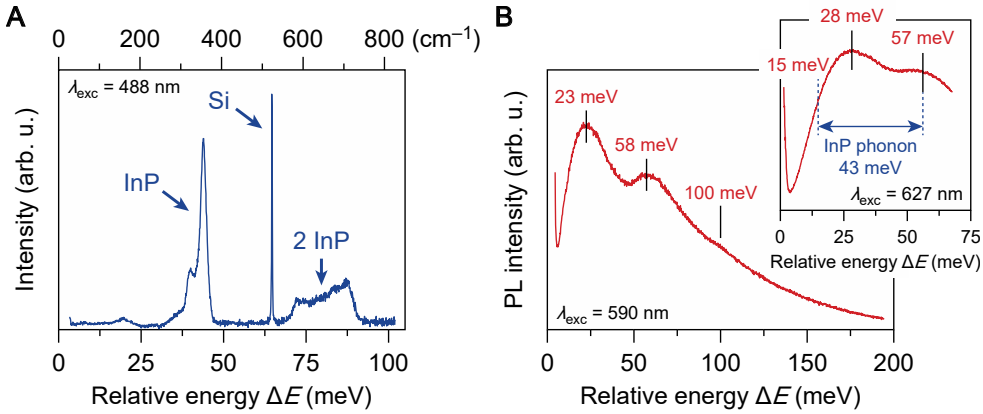

Figure 5.1. Raman and FLN spectra recorded at 4 K for InP/ZnS core/shell QDs with a core diameter of 3.0 ± 0.1 nm. a) Raman spectrum, obtained upon excitation at 2.54 eV. The peaks in the 300–400 cm^{-1} range are assigned to the LO and TO phonon modes of the InP cores. b) FLN spectrum of the same InP/ZnS core/shell QD sample, obtained by exciting resonantly at 2.10 eV. Inset: high-resolution FLN spectrum of the same sample, obtained by exciting resonantly at 1.98 eV and detected by a triple-grating spectrometer. The laser energy (excited state energy) is taken as reference and set to 0 meV, and the emission intensity is plotted as a function of $\Delta E = E_{laser} - E_{detected}$. The highest-intensity peak is related to emission from the dark state coupled to an acoustic phonon, the lower-intensity peaks are related to optical phonon replicas of the dark state.

Figure 5.1a presents the Raman spectrum of the InP/ZnS core/shell QDs recorded at 4 K, exciting the sample at 2.54 eV. It shows two peaks (fitting in Appendix, Figure A5.2) at 324 and 355 cm^{-1} (40 and 44 meV), which can be assigned to the transverse-optical (TO) and longitudinal-optical (LO) phonon modes of InP. These two peaks are shifted to higher energies compared to LO and TO phonon modes of the bare InP QDs (respectively 310 and 342 cm^{-1}),[34,35] presumably due to the compressive strain created by the lattice mismatch with the ZnS shell, since the lattice parameter of ZnS is smaller than that of InP, (viz., 5.420 and 5.869 Å, respectively, at 300 K). Similar results have been reported for InP QDs with CdSe and ZnSe shells.[17,25] The sharp peak at approximately 520 cm^{-1} originates from the crystalline silicon substrate.[36] At about 550–750 cm^{-1} double Raman processes of the InP phonons are observed. No clear signature of ZnS phonons is observed between 275 and 350 cm^{-1} such as in the bulk material.[37] However a bump around 250–300 cm^{-1} may be assigned to ZnS phonon modes. The absence of clear ZnS-related peaks is possibly due to the limited thickness of the ZnS shell, combined with partial overlap with the InP phonon peaks. We believe that the weak features below 200 cm^{-1} are associated to phonon modes related to the InP lattice, considering they are also present in the InP/ZnSe spectrum (see below and Appendix, Figure A5.3).

Figure 5.1b shows the low temperature (4 K) FLN spectrum of the InP/ZnS core/shell QDs, excited resonantly at 2.10 eV. The inset is the high-resolution FLN spectrum of the same sample, obtained by exciting the sample at 1.89 eV. The FLN spectra are referred to the energy of the excitation laser, which means that the energy of the excited state populated

by the laser is taken as a reference and set to 0 meV. Two pronounced peaks are resolved at 23 meV and 58 meV from the laser line. A third less defined feature is visible around 100 meV. The highest-intensity peak at 23 meV is ascribed to emission from the dark state coupled to acoustic phonons,[17] while the lower-intensity peak at 58 meV is attributed to a vibronic replica due to coupling of the dark state with InP LO/TO phonons. The feature in the FLN spectrum at about 100 meV is assigned to a two-phonon replica due to coupling to the LO/TO phonon modes of InP. Although the zero-phonon-line (ZPL) of the dark state is not resolved in the spectra, its position may be estimated by subtracting the InP phonon energy of 43 meV from the resonance peak observed at 58 meV, which yields 15 meV.

5.2.4 Phonons in InP/ZnSe QDs

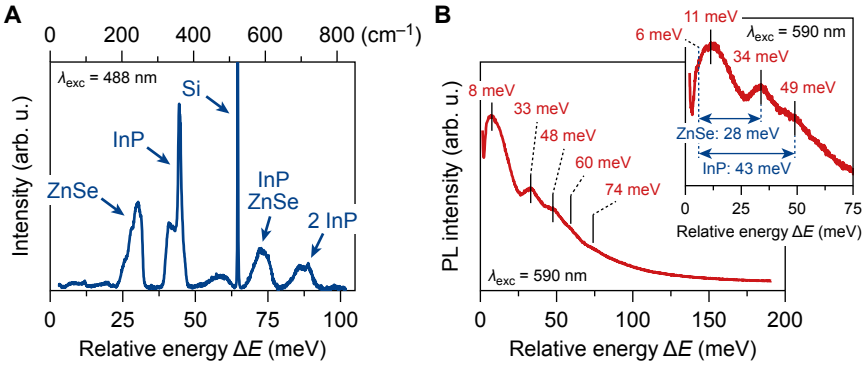

Figure 5.2. Raman and FLN spectra recorded at 4 K for InP/ZnSe core/shell QDs with a core diameter of 3.0 ± 0.1 nm. a) Raman spectrum, obtained upon excitation at 2.54 eV. The peaks in the 300–400 cm^{-1} range are assigned to the LO and TO phonon modes of the InP core in the InP/ZnSe core/shell QDs. The group of peaks around 200–260 cm^{-1} is assigned to the ZnSe phonon modes. b) FLN spectrum of the same InP/ZnSe core/shell QD sample. Inset: high-resolution FLN spectrum of the same sample, detected by a triple-grating spectrometer. The spectra are obtained by exciting resonantly the sample at 2.10 eV. This excited state (2.10 eV) is taken as reference and set to 0 meV, and the emission intensity is plotted as a function of $\Delta E = E_{laser} - E_{detected}$. The highest-intensity peak is related to emission from the dark state coupled to an acoustic phonon, the lower-intensity peaks are related to optical phonon replicas of the ZnSe shell (28 meV) and the InP core (43 meV). The energies of phonon modes involved are indicated.

In Figure 5.2 we study the phonons involved in the excitonic recombination process in InP/ZnSe QDs. The Raman spectrum in Figure 5.2a, obtained under 2.54 eV excitation, shows peaks between 200 and 260 cm^{-1} (25–32 meV) that are absent in the Raman spectra of InP/ZnS QDs (see Figure 5.1a). We attribute these peaks to ZnSe phonons.[17,25,38] The LO and TO phonon modes of the InP lattice are present, also in this case, in the spectral range between 315 and 380 cm^{-1} (39–47 meV). Above 400 cm^{-1} it is possible to identify double Raman and combination Raman processes of the InP and ZnSe phonons: the double mode of ZnSe lattice at approximately 470 cm^{-1}, the combination band of InP and ZnSe phonons at 590 cm^{-1}, and the double mode of InP lattice (plus possible contributions from the third overtone of ZnSe phonon mode) between 650 and 750 cm^{-1}. The weak peaks below 200 cm^{-1} are associated to phonon modes of the InP lattice (see Appendix, Figure A5.3). In particular they can be ascribed to single process of acoustic phonon modes of InP due to

an increase of the density of states in the center of the Brillouin zone (Γ) possibly created by defects in the crystal structure and a consequent back-folding of the phonon dispersion curves towards Γ[34,39] or to double processes at the edge of the Brillouin zone where the density of states may be strong. As mentioned above, the sharp peak at approximately 520 cm^{-1} comes from the phonon modes of the crystalline silicon substrate.[36]

Figure 5.2b displays the FLN spectrum of the same InP/ZnSe QD sample excited at 2.10 eV. The highest-intensity peak (at around 8 meV from the laser line) is assigned to emission from the dark state coupled to acoustic phonons, as previously done in chapter 3. The peaks at 33 meV and 48 meV are attributed to vibronic replicas due to coupling of the dark state with a ZnSe and InP optical phonon, respectively. Furthermore, two weaker features, around 60 and 74 meV, are visible. These energy values match with a coupling of the dark state with two ZnSe phonons or with one InP and one ZnSe phonon respectively. By subtracting the ZnSe phonon energy of 28 meV from the peak at 33 meV, or the InP phonon energy of 43 meV from the peak at 48 meV, we find a value of 5 meV for the ZPL. Interestingly, a weak hump is observed at 5-6 meV in the high-resolution FLN spectrum (inset in Figure 5.2b) which can thus be assigned to the ZPL.

5.2.5 Phonons in InP/(Cd, Zn)Se QDs

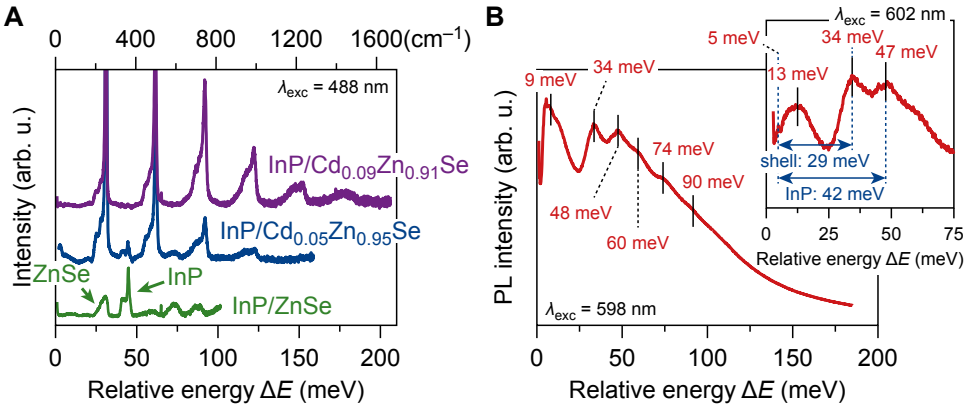

Figure 5.3. Raman and FLN spectra recorded at 4 K for InP/ZnSe and InP/(Cd, Zn)Se core/shell QDs with the same InP core diameter of 3.0 ± 0.1 nm. a) Raman spectra obtained upon excitation at 2.54 eV of InP/ZnSe core/shell QDs (green), and InP/(Cd, Zn)Se core/shell QDs with 5% of Cd (blue) and with 9% of Cd (purple). For clarity, curves have been shifted vertically and the most intense peaks are not fully shown. b) FLN spectrum of the InP/(Cd, Zn)Se core/shell QDs with 9% of Cd, obtained upon resonant excitation at 2.07 eV. The inset shows the corresponding high-resolution spectrum upon excitation at 2.06 eV. The emission intensity is plotted as a function of $\Delta E = E_{laser} - E_{detected}$. The phonon energies involved are indicated.

Figure 5.3a presents the Raman spectra of InP/ZnSe core/shell QDs, and InP/(Cd, Zn)Se with 5% and 9% Cd, obtained under 2.54 eV excitation. A strong resonant effect is observed in the Raman scattering peaks of the samples with Cd containing shells. Moreover, this effect is enhanced by increasing the amount of Cd in the shell. As a consequence of this strong resonance, an impressive series of overtones are observed for the shells with 5 and 9% of

Cd, probably due to a better overlap between the shell bandgap and the excitation energy. The energy of the phonon modes of the shell around 200–260 cm^{-1} does not significantly change when Cd is mixed into the ZnSe material (up to 9%), as was observed previously.[25] Contrary to the strongly enhanced Raman scattering signal from shell phonons, the signal from InP core phonons decreases with Cd doping and is hardly observable for the QDs with 9% Cd shell. Similarly to the shell phonons, the energy of InP core phonons is not significantly affected by composition of the (Cd,Zn)Se shell.[25]

We compare the phonon energies extracted from the Raman spectra with the positions of the FLN peaks of the InP/(Cd, Zn)Se QDs sample with 9% Cd (Figure 5.3b). The FLN peak energies are comparable to those observed for the InP/ZnSe QDs sample (Figure 5.2b), but the phonon replicas are better defined. In the FLN spectrum of the sample with 9% Cd, we even observe an indication of a two-InP phonon replica at approximately 90 meV from the laser line. Furthermore, a small peak at approximately 5 meV is observed and ascribed to the ZPL. The energy difference from this ZPL to the peaks at 33 meV and at 48 meV matches perfectly with the phonon energies of the (Cd,Zn)Se shell and the InP core, respectively.

5.2.6 Photoluminescence decay of InP/ZnS, InP/ZnSe and InP/(Cd,Zn)Se core/shell QDs

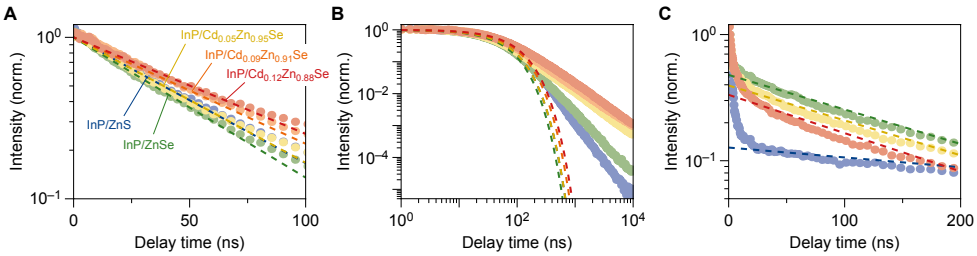

Figure 5.4. PL decay curves measured at the PL peak maximum for the InP/ZnS QDs (blue), InP/ZnSe QDs (green), and InP/(Cd,Zn)Se core/shell QDs with 5% Cd (yellow), 9% Cd (orange) and 12% Cd (red). Dashed lines are fits to single-exponential decay. a) PL decay curves measured at room temperature and plotted on a semi-logarithmic scale. b) The same PL decay curves, but plotted on a double-logarithmic scale up to a delay time of 10 µs. c) PL decay curves measured at 4 K at the peak maximum (which is shifted compared to room temperature) and plotted on a semi-logarithmic scale.

Figure 5.4a shows the PL decay curves of our samples measured at the PL peak maximum at room temperature for the InP/ZnS QDs (blue), InP/ZnSe QDs (green), and InP/(Cd,Zn)Se core/shell QDs with 5% Cd (yellow), 9% Cd (orange) and 12% Cd (red). On a short time scale up to 100 ns, the curves are nearly single-exponential with lifetimes of approximately 50 ns. This initial fast decay is ascribed to the exciton radiative recombination, which involves the bright and dark exciton fine-structure states in thermal equilibrium.[16,17,40] The radiative recombination rate is proportional to the square of the spatial overlap integral of the electron and hole wave functions.[15,41,42] Therefore, a reduction of the spatial overlap affects the oscillator strength of the exciton transitions and, accordingly, the radiative decay rates.[15]

Using a single-exponential fit on the timescale from 0 to 100 ns, we estimate a radiative lifetime of $\tau = 55.7$ ns for the InP/ZnS QDs, and increasing lifetimes of $\tau = 50.0$, 55.9, 65.9, and 72.6 ns for the InP/(Cd,Zn)Se QDs with increasing Cd content of 0, 5, 9, and 12%, respectively. This lengthening of the exciton radiative lifetime suggests that the electron–hole wave function overlap in InP/(Cd,Zn)Se QDs gradually decreases as the Cd content in the shell increases. This can be attributed to the increasing delocalization of the electron wave function into the shell due to the gradual reduction of the conduction-band offset with increasing Cd content. Indeed admixing Cd into a ZnSe shell reduces the bandgap of the shell.[24]

Figure 5.4b presents the same PL decay curves at room temperature, plotted on a double-logarithmic until 10 μs after excitation. On the time scale beyond 100 ns, the PL decay curves deviate from the single exponent that we fitted in Figure 5.4a (dashed lines), and the emission is dominated by a 'delayed component' with approximately power-law decay (*i.e.*, straight line on double-logarithmic scale). This delayed component is assigned to temporary charge trapping (for example on the surface or at the core–shell hetero-interface of the QD) for up to a few microseconds, until the exciton state is restored by detrapping and then emits a photon.[43] The contribution of the delayed emission (and hence the probability of temporary charge carrier trapping) is smallest in the InP/ZnS QDs and increases with increasing Cd content for the InP/(Cd,Zn)Se QDs. This trend might be related to the larger shell thickness of QDs with higher Cd content (with a consequent increase of average number of traps per QD) or to the additional electron wave function delocalization into the shell. A similar behavior was found for CdSe/CdS QDs with increasing CdS shell thickness.[43]

Figure 5.4c shows the PL decay curves of our samples at 4 K. The decay curves show a fast component at $t < 25$ ns, which we ascribe to emission from higher-energy (bright) states shortly after the laser pulse and prior to thermalization.[15–17,43–48] The slower decay from 50 to 200 ns is ascribed to radiative recombination from (mostly) the dark exciton state. Whereas at room-temperature the lowest bright and dark exciton fine-structure states are both populated at thermal equilibrium, at 4 K the dark state dominates the thermal population distribution. The radiative lifetime is therefore significantly longer than at room temperature. This is evident when comparing Figures 5.4a and 5.4c. We estimate the radiative lifetimes at 4 K from a single-exponential fit of the PL decay curves, excluding the

initial fast component. The largest reduction of the radiative recombination rates occurs for the InP/ZnS QD sample, as the lifetime increases by a factor 10 from 55.7 ns at room temperature to 556 ns at 4 K.

Interestingly, the effect of the shell composition (*i.e.,* ZnS *versus* (Cd,Zn)Se with increasing Cd content) on the radiative lifetimes at 4 K is opposite to that observed at room temperature. We find that the radiative lifetime at 4 K is by far the longest for the InP/ZnS QDs (*viz*., 556 ns), and decreases from 159 ns for the InP/ZnSe QDs to 157 ns and 143 ns for InP/(Cd,Zn)Se QDs with 9 and 12% Cd, respectively. This is in striking contrast to the behaviour observed at room temperature, where the lifetime lengthens with increasing Cd content from 50 ns (no Cd) to 72.6 ns (12% Cd). These seemingly contradictory observations can nevertheless be both understood in terms of the effect of the shell composition on the delocalization of the electron wavefunction. As discussed above, the electron delocalization into the shell increases with increasing Cd content, due to the gradual reduction of the conduction band offset between the InP core and the (Cd,Zn)Se shell. This is clearly reflected in the shift of PL peak to lower energies with increasing Cd content (*viz*., from 2.06 to 1.92 eV, from no Cd to 12% Cd), as a result of the reduction of the quantum confinement potential. At room temperature, the direct effect of the reduction of the electron–hole overlap integral on the exciton oscillator strength dominates because the emission originates primarily from the bright exciton fine-structure state. Consequently, the exciton radiative lifetime at room temperature lengthens with increasing Cd content. In contrast, at 4 K the emission comes predominantly from the dark exciton fine-structure state because the population of the bright exciton state is negligible. Radiative recombination from the dark state is forbidden within the electric-dipole approximation, and therefore coupling to polar phonons is required to induce significant transition dipole moments, and hence enhance the radiative recombination rate.[15,40,49,50] The vibronic nature of the dark-exciton emission is clearly evidenced in the FLN spectra discussed above. As a result, the radiative recombination rate of the dark exciton fine-structure state (and therefore the radiative lifetime at 4 K) is expected to be extremely sensitive to the exciton-phonon coupling strength. We argue that the dependence of the radiative lifetimes at 4 K on the shell composition can be rationalized in terms of the impact of the delocalization of the electron wave function on the exciton–phonon coupling. The gradual increase of the electron delocalization into the shell going from ZnS to (Cd,Zn)Se with increasing Cd content leads to increasingly larger exciton polarizability, which enhances coupling to polar lattice phonons through the Fröhlich interaction,[19,29–31] as previously shown for Type-I[1/2] and Type-II CdTe/CdSe hetero-nanocrystals with increasing degree of electron–hole spatial separation.[27] This interpretation is consistent with the FLN data discussed above, which shows more pronounced phonon replicas for InP core/shell QDs when going from a ZnS (Figure 5.1b) to a ZnSe (Figure 5.2b) and to a (Cd,Zn)Se (Figure 5.3b) shell.

5.3 Conclusion

We studied the exciton fine-structure and the role of phonons in core/shell quantum dot (QD) systems with an InP core of around 3.0 ± 0.1 nm and various shells: ZnS, ZnSe and (Zn,Cd)Se. In particular, the phonon energies extracted from Raman spectra were compared with the peak positions in fluorescence line narrowing (FLN) spectra at $T = 4$ K. Our results demonstrate how the lower bright and dark exciton fine-structure states are involved in the exciton radiative recombination and the dynamic and crucial role of phonons in activating the emission from the dark state. We find that the exciton recombination process involves acoustic and optical phonons of both the core and the shell. The coupling to phonons plays a major role in the recombination process increasing the oscillator strength of the dark state[15,40,49,50] and hence enhancing the radiative recombination rates.

5.4 Methods

Sample preparation. InP/ZnS and InP/ZnSe core/shell QD samples were synthesized, following the method reported in ref. 9. InP QDs with (Zn,Cd)Se shell were synthesized following the method of ref. 24. The QD samples were washed by precipitation with methanol, isolated by centrifugation and redispersed in toluene and 1-dodecanethiol. To achieve a QDs film the solution was deposited using a *drop-cast* method, on crystalline silicon substrate for Raman and FLN measurements, and on a quartz substrate for PL and TrPL measurements.

PL and Time-resolved Photoluminescence (TrPL). The PL and the Time-resolved PL measurements were performed on QD films deposited on quartz substrates (see sample preparation above). In the PL measurements, the excitation was provided by a 450 W Xenon lamp and the PL signal was dispersed by an Edinburgh Instruments FLS920 spectrometer equipped with double grating monochromators and detected by a Hamamatsu R928 photomultiplier tube (PMT). The Time-resolved PL decay measurements were performed monitoring the PL peak wavelength for all samples. The excitation was provided by a pulsed diode laser, operating at 405 nm with a repetition rate of 100 kHz. The Time-resolved PL curves were acquired by time-correlated single-photon counting using a Hamamatsu H7422 PMT. The average count rate was kept at 3% of the laser repetition rate, by adjusting the slit width. This low excitation fluence was used in order to maintain single photon statistics and avoid multiexciton formation.

To achieve low temperatures, samples were placed inside an optical ^{4}He cryostat (Oxford Instruments).

Raman spectroscopy measurements. Raman scattering measurements were performed at High Field Magnet Laboratory (Radboud University). To achieve low temperatures, samples were placed in an optical ^{4}He cryostat (Microstat Oxford). Samples were probed in backscattering geometry with an incident laser line at 488 nm from a solid-state laser. To prevent both excessive laser heating and sample damage, a low laser power of 30 µW was used. The scattered light was filtered by a RazorEdge ultrasteep long-pass edge filter and analyzed by a 1 m long single grating (1200 grooves/mm) FHR-1000 Horiba spectrometer equipped with a nitrogen-cooled PyLoN CCD camera (Princeton Instruments). The resolution of our measurements was 1 cm^{-1}.

Fluorescence Line-Narrowing (FLN) measurements. FLN experiments at low temperatures were performed at the High Field Magnet Laboratory (Radboud University). For these experiments the samples used were QD films on crystalline silicon substrate (see sample preparation). To achieve low temperatures, the samples were placed in an optical ^{4}He cryostat (Microstat Oxford). Samples were probed in backscattering geometry. The FLN measurements were performed using a narrow excitation source, achieved by using a tunable jet-stream dye (Rhodamine 6G) laser. This monochromatic laser beam was circularly polarized by means of a linear polarizer and a Babinet-Soleil compensator. The FLN signal was guided through a 0.3 m long single grating spectrometer (300 grooves/mm grating) and detected by a liquid nitrogen cooled charge couple device (CCD). The emitted photons were detected in crossed polarization relative to the laser polarization by using a linear polarizer and a lambda-quarter wave plate. Cut-off optical filters were used in excitation and detection.

For the high-resolution FLN spectra, the samples were mounted in a titanium sample holder on top of a three-axis piezo-positioner. The laser beam was focused on the sample by a singlet lens (10 mm focal length). The same lens was used to collect the PL emission and direct it to the detection setup (Backscattering geometry). The samples and optical probe were mounted inside a liquid-helium bath cryostat. The high-resolution FLN emission was detected in crossed polarization mode relative to the laser polarization by using a linear polarizer and a lambda-quarter wave plate. The resonant-PL emission was analyzed by a 0.5 m long triple-grating spectrometer (3∗1800 grooves/mm holographic gratings) in subtractive mode, equipped with a liquid nitrogen cooled CCD camera (Symphony-Horiba).

ACKNOWLEDGMENT: We acknowledge the support of the HFML-RU/FOM, member of the European Magnetic Field Laboratory (EMFL).

5.5 References

1 Grundmann, M. The Present Status of Quantum Dot Lasers. *Phys. E Low-dimensional Syst. Nanostructures* **1999**, *5*, 167–184.

2 Ledentsov, N. N. Quantum Dot Laser. *Semicond. Sci. Technol.* **2011**, *26*, 014001.

2 Samuel, I. Colloidal Nanocrystals: Electrifying Quantum Dots for Lasers. *Nat. Mater.* **2017**, *17*, 9–10.

4 Jang, E.; Jun, S.; Jang, H.; Lim, J.; Kim, B.; Kim, Y. White-Light-Emitting Diodes with Quantum Dot Color Converters for Display Backlights. *Adv. Mater.* **2010**, *22*, 3076–3080.

5 Kim, T.-H.; Jun, S.; Cho, K.-S.; Choi, B. L.; Jang, E. Bright and Stable Quantum Dots and Their Applications in Full-Color Displays. *MRS Bull.* **2013**, *38*, 712–720.

6 Talapin, D. V.; Steckel, J. Quantum Dot Light-Emitting Devices. *MRS Bull.* **2013**, *38*, 685–691.

7 Supran, G. J.; Shirasaki, Y.; Song, K. W.; Caruge, J.-M.; Kazlas, P. T.; Coe-Sullivan, S.; Andrew, T. L.; Bawendi, M. G.; Bulović, V. QLEDs for Displays and Solid-State Lighting. *MRS Bull.* **2013**, *38*, 703–711.

8 Steckel, J. S.; Ho, J.; Coe-Sullivan, S. QDs Generate Light for Next-Generation Displays. *Photonics Spectra* **2014**, *48*, 55–61.

9 Tessier, M. D.; Dupont, D.; De Nolf, K.; De Roo, J.; Hens, Z. Economic and Size-Tunable Synthesis of InP/ZnE (E = S, Se) Colloidal Quantum Dots. *Chem. Mater.* **2015**, *27*, 4893–4898.

10 Toufanian, R.; Piryatinski, A.; Mahler, A. H.; Iyer, R.; Hollingsworth, J. A.; Dennis, A. M. Bandgap Engineering of Indium Phosphide-Based Core/Shell Heterostructures Through Shell Composition and Thickness. *Front. Chem.* **2018**, *6*, 1–12.

11 Li, Y.; Hou, X.; Dai, X.; Yao, Z.; Lv, L.; Jin, Y.; Peng, X. Stoichiometry-Controlled InP-Based Quantum Dots: Synthesis, Photoluminescence, and Electroluminescence. *J. Am. Chem. Soc.* **2019**, *141*, 6448–6452.

12 Nirmal, M.; Norris, D. J.; Kuno, M.; Bawendi, M. G.; Efros, A. L.; Rosen, M. Observation of the "Dark Exciton" in CdSe Quantum Dots. *Phys. Rev. Lett.* **1995**, *75*, 3728–3731.

13 Efros, A.; Rosen, M.; Kuno, M.; Nirmal, M.; Norris, D.; Bawendi, M. Band-Edge Exciton in Quantum Dots of Semiconductors with a Degenerate Valence Band: Dark and Bright Exciton States. *Phys. Rev. B* **1996**, *54*, 4843–4856.

14 Blokland, J. H.; Claessen, V. I.; Wijnen, F. J. P.; Groeneveld, E.; de Mello Donegá, C.; Vanmaekelbergh, D.; Meijerink, A.; Maan, J. C.; Christianen, P. C. M. Exciton Lifetimes of CdTe Nanocrystal Quantum Dots in High Magnetic Fields. *Phys. Rev. B* **2011**, *83*, 035304.

15 Granados del Águila, A.; Groeneveld, E.; Maan, J. C.; de Mello Donegá, C.; Christianen, P. C. M. Effect of Electron–Hole Overlap and Exchange Interaction on Exciton Radiative Lifetimes of CdTe/CdSe Heteronanocrystals. *ACS Nano* **2016**, *10*, 4102–4110.

16 Biadala, L.; Siebers, B.; Beyazit, Y.; Tessier, M. D.; Dupont, D.; Hens, Z.; Yakovlev, D. R.; Bayer, M. Band-Edge Exciton Fine Structure and Recombination Dynamics in InP/ZnS Colloidal Nanocrystals. *ACS Nano* **2016**, *10*, 3356–3364.

17 Brodu, A.; Ballottin, M. V.; Buhot, J.; Van Harten, E. J.; Dupont, D.; La Porta, A.; Prins, P. T.; Tessier, M. D.; Versteegh, M. A. M.; Zwiller, V.; *et al.* Exciton Fine Structure and Lattice Dynamics in InP/ZnSe Core/Shell Quantum Dots. *ACS Photonics* **2018**, *5*, 3353–3362.

18 Micic, O. I.; Cheong, H. M.; Fu, H.; Zunger, A.; Sprague, J. R.; Mascarenhas, A.; Nozik, A. J. Size-Dependent Spectroscopy of InP Quantum Dots. *J. Phys. Chem. B* **1997**, *101*, 4904–4912.

19 Shiang, J. J.; Risbud, S. H.; Alivisatos, A. P. Resonance Raman Studies of the Ground and Lowest Electronic Excited State in CdS Nanocrystals. *J. Chem. Phys.* **1993**, *98*, 8432–8442.

20 Klein, M. C.; Hache, F.; Ricard, D.; Flytzanis, C. Size Dependence of Electron-Phonon Coupling in Semiconductor Nanospheres: The Case of CdSe. *Phys. Rev. B* **1990**, *42*, 11123–11132.

21 Alivisatos, A. P.; Harris, T. D.; Carroll, P. J.; Steigerwald, M. L.; Brus, L. E. Electron–vibration Coupling in Semiconductor Clusters Studied by Resonance Raman Spectroscopy. *J. Chem. Phys.* **1989**, *90*, 3463–3468.

22 Nirmal, M.; Murray, C. B.; Bawendi, M. G. Fluorescence-Line Narrowing in CdSe Quantum Dots: Surface Localization of the Photogenerated Exciton. *Phys. Rev. B* **1994**, *50*, 2293–2300.

23 Donegá, C. D. M. Synthesis and Properties of Colloidal Heteronanocrystals. *Chem. Soc. Rev.* **2011**, *40*, 1512–1546.

24 Dupont, D.; Tessier, M. D.; Smet, P. F.; Hens, Z. Indium Phosphide-Based Quantum Dots with Shell-Enhanced Absorption for Luminescent Down-Conversion. *Adv. Mater.* **2017**, *29*, 1700686.

25 Rafipoor, M.; Dupont, D.; Tornatzky, H.; Tessier, M. D.; Maultzsch, J.; Hens, Z.; Lange, H. Strain Engineering in InP/(Zn,Cd)Se Core/Shell Quantum Dots. *Chem. Mater.* **2018**, *30*, 4393–4400.

26 Htoon, H.; Malko, A. V.; Bussian, D.; Vela, J.; Chen, Y.; Hollingsworth, J. A.; Klimov, V. I. Highly Emissive Multiexcitons in Steady-State Photoluminescence of Individual "Giant" CdSe/CdS Core/Shell Nanocrystals. *Nano Lett.* **2010**, *10*, 2401–2407.

27 Dennis, A. M.; Mangum, B. D.; Piryatinski, A.; Park, Y. S.; Hannah, D. C.; Casson, J. L.; Williams, D. J.; Schaller, R. D.; Htoon, H.; Hollingsworth, J. a. Suppressed Blinking and Auger Recombination in Near-Infrared Type-II InP/CdS Nanocrystal Quantum Dots. *Nano Lett.* **2012**, *12*, 5545–5551.

28 Toufanian, R.; Piryatinski, A.; Mahler, A. H.; Iyer, R.; Hollingsworth, J. A.; Dennis, A. M. Bandgap Engineering of Indium Phosphide-Based Core/Shell Heterostructures Through Shell Composition and Thickness. *Front. Chem.* **2018**, *6*, 1–12.

29 Lin, C.; Gong, K.; Kelley, D. F.; Kelley, A. M. Electron-Phonon Coupling in CdSe/CdS Core/Shell Quantum Dots. *ACS Nano* **2015**, *9*, 8131–8141.

30 Groeneveld, E.; De Mello Donegá, C. Enhanced Exciton-Phonon Coupling in Colloidal Type-II CdTe-CdSe Heteronanocrystals. *J. Phys. Chem. C* **2012**, *116*, 16240–16250.

31 Cui, J.; Beyler, A. P.; Coropceanu, I.; Cleary, L.; Avila, T. R.; Chen, Y.; Cordero, J. M.; Heathcote, S. L.; Harris, D. K.; Chen, O.; *et al.* Evolution of the Single-Nanocrystal Photoluminescence Linewidth with Size and Shell: Implications for Exciton-Phonon Coupling and the Optimization of Spectral Linewidths. *Nano Lett.* **2016**, *16*, 289–296.

32 Haruna, K.; Maeta, H.; Ohashi, K.; Koike, T. The Thermal Expansion Coefficient and Gruneisen Parameter of InP Crystal at Low Temperatures. *J. Phys. C Solid State Phys.* **1987**, *20*, 5275–5279.

33 Nirmal, M.; Murray, C. B.; Bawendi, M. G. Fluorescence-Line Narrowing in CdSe Quantum Dots: Surface Localization of the Photogenerated Exciton. *Phys. Rev. B* **1994**, *50*, 2293–2300.

34 Hou, H. J.; Kong, F. J. Theoretical Investigation on the Structural, Dynamical, and Thermodynamic Properties of the Zinc-Blende InX (X = P, As, Sb). *Phys. status solidi* **2011**, *248*, 1399–1404.

35 Seong, M. J.; Mićić, O. I.; Nozik, A. J.; Mascarenhas, A.; Cheong, H. M. Size-Dependent Raman Study of InP Quantum Dots. *Appl. Phys. Lett.* **2003**, *82*, 185–187.

36 Lu, Z. Q.; Quinn, T.; Reehal, H. S. Polarization-Dependent Raman Spectra of Thin Crystalline Silicon Films. *J. Appl. Phys.* **2005**, *97*, 033512.

37 Vagelatos, N.; Wehe, D.; King, J. S. Phonon Dispersion and Phonon Densities of States for ZnS and ZnTe. *J. Chem. Phys.* **1974**, *60*, 3613–3618.

38 Rössler, U. *New Data and Updates for Several Semiconductors with Chalcopyrite Structure, for Several II-VI Compounds and Diluted Magnetic IV-VI Compounds*; Springer: Berlin, Heidelberg, 2013.

39 Gadret, E. G.; De Lima, M. M.; Madureira, J. R.; Chiaramonte, T.; Cotta, M. A.; Iikawa, F.; Cantarero, A. Optical Phonon Modes of Wurtzite InP. *Appl. Phys. Lett.* **2013**, *102*.

40 Eilers, J.; Van Hest, J.; Meijerink, A.; Donega, C. D. M. Unravelling the Size and Temperature Dependence of Exciton Lifetimes in Colloidal ZnSe Quantum Dots. *J. Phys. Chem. C* **2014**, *118*, 23313–23319.

41 de Mello Donegá, C.; Koole, R. Size Dependence of the Spontaneous Emission Rate and Absorption Cross Section of CdSe and CdTe Quantum Dots. *J. Phys. Chem. C* **2009**, *113*, 6511–6520.

42 Efros, A. L. Luminescence Polarization of CdSe Microcrystals. *Phys. Rev. B* **1992**, *46*, 7448–7458.

43 Rabouw, F. T.; Kamp, M.; van Dijk-Moes, R. J. A.; Gamelin, D. R.; Koenderink, A. F.; Meijerink, A.; Vanmaekelbergh, D. Delayed Exciton Emission and Its Relation to Blinking in CdSe Quantum Dots. *Nano Lett.* **2015**, *15*, 7718–7725.

44 Liu, F.; Biadala, L.; Rodina, A. V.; Yakovlev, D. R.; Dunker, D.; Javaux, C.; Hermier, J.-P.; Efros, A. L.; Dubertret, B.; Bayer, M. Spin Dynamics of Negatively Charged Excitons in CdSe/CdS Colloidal Nanocrystals. *Phys. Rev. B* **2013**, *88*, 035302.

45 Biadala, L.; Louyer, Y.; Tamarat, P.; Lounis, B. Direct Observation of the Two Lowest Exciton Zero-Phonon Lines in Single CdSe/ZnS Nanocrystals. *Phys. Rev. Lett.* **2009**, *103*, 037404.

46 Liu, F.; Biadala, L.; Rodina, A. V.; Yakovlev, D. R.; Dunker, D.; Javaux, C.; Hermier, J.-P.; Efros, A. L.; Dubertret, B.; Bayer, M. Spin Dynamics of Negatively Charged Excitons in CdSe/CdS Colloidal Nanocrystals. *Phys. Rev. B* **2013**, *88*, 035302.

47 Biadala, L.; Siebers, B.; Gomes, R.; Hens, Z.; Yakovlev, D. R.; Bayer, M. Tuning Energy Splitting and Recombination Dynamics of Dark and Bright Excitons in CdSe/CdS Dot-in-Rod Colloidal Nanostructures. *J. Phys. Chem. C* **2014**, *118*, 22309–22316.

48 Oron, D.; Aharoni, A.; de Mello Donega, C.; van Rijssel, J.; Meijerink, A.; Banin, U. Universal Role of Discrete Acoustic Phonons in the Low-Temperature Optical Emission of Colloidal Quantum Dots. *Phys. Rev. Lett.* **2009**, *102*, 177402.

49 Wong, C. Y.; Kim, J.; Nair, P. S.; Nagy, M. C.; Scholes, G. D. Relaxation in the Exciton Fine Structure of Semiconductor Nanocrystals. *J. Phys. Chem. C* **2009**, *113*, 795–811.

50 Huxter, V. M.; Scholes, G. D. Acoustic Phonon Strain Induced Mixing of the Fine Structure Levels in Colloidal CdSe Quantum Dots Observed by a Polarization Grating Technique. *J. Chem. Phys.* **2010**, *132*, 104506.

5.6 Appendix

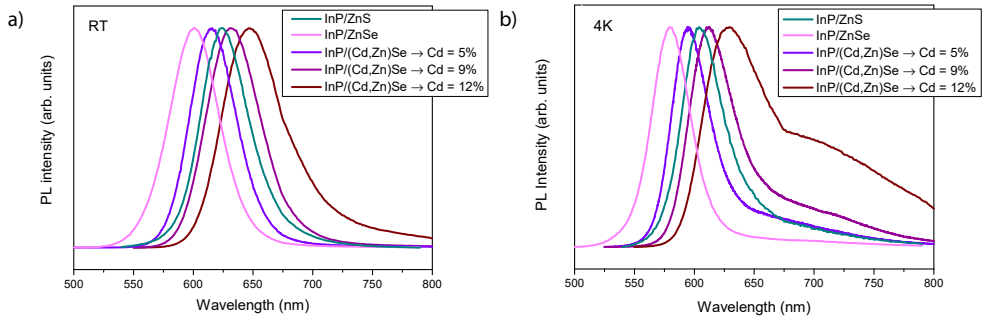

Figure A5.1: Normalized ensemble PL spectra for the five InP core/shell QD samples having various shells: ZnS, ZnSe and (Zn,Cd)Se with different amounts of Cd (5%, 9%, 12%), a) at room temperature, b) at 4 K.

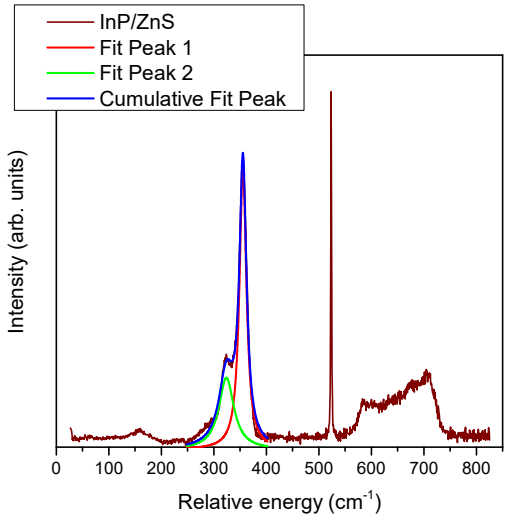

Figure A5.2: Lorentzian fits in Raman spectrum recorded at 4 K, with a 488 nm laser line, for InP/ZnSe core/shell QDs with a core diameter of around 3 nm.

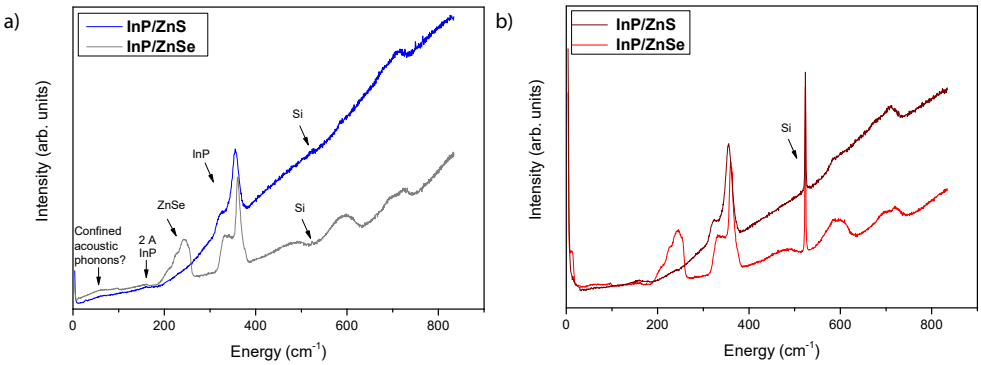

Figure A5.3: Raman recorded at 4 K, with a 488 nm laser line, for InP/ZnSe and InP/ZnS core/shell QDs with a core diameter of around 3 nm. a) Raman spectrum, obtained with perpendicular polarization configuration. b) Raman spectrum, obtained with parallel polarization configuration. The background is due to a residual luminescence of the samples.

Chapter 6

Exciton fine structure of InP/(Zn,Cd)Se core/shell quantum dots

Based on:
Exciton fine structure of InP/(Zn,Cd)Se core/shell Quantum Dots.
Annalisa Brodu, Jonathan Buhot, Mariana V. Ballottin, Marion Severijnen, Dorian Dupont, Zeger Hens, Freddy T. Rabouw, Peter C. M. Christianen, Celso de Mello Donega, and Daniel Vanmaekelbergh.
In preparation.

Colloidal InP QDs are a feasible alternative for CdSe QDs in opto-electronic applications. InP(core)/ZnSe(shell) systems show reasonable photoluminescence quantum efficiencies, but with a photoluminescence spectrum that is considerably broader than that of the CdSe QD counterparts. It is thus of interest to study the exciton fine structure of this system, including the coupling of different exciton states to the lattice phonons. In an attempt to reduce the interfacial strain between core and shell, we have also added variable amounts of Cd to the ZnSe shell. We use FLN spectroscopy to study the exciton fine structure with reduced spectral broadening. Furthermore, we vary the magnetic field from 0 to 30 T in order to induce a Zeeman splitting in the different types of spin states. We observe that a bright $F = \pm 1$ level splits into $F = +1$ and $F = -1$ states, crossing in energy a lower bright $F = 0$ level upon increasing magnetic field. Furthermore, the radiative decay from the dark state is enhanced by interaction with acoustic phonons, and with optical phonons from the InP core and the II-VI compound shell, as well. The exciton fine structure remains roughly unchanged with the amount of Cd (0 - 9%) incorporated in the ZnSe shell.

Abstract

6.1 Introduction

Colloidal semiconductor nanocrystals show an energy level structure and related optical properties that strongly depend on the size and shape of the nanocrystals. This is due to spatial confinement of the exciton wave function in the nanocrystal. Semiconductor nanocrystals that have all three dimensions sufficiently small to confine the exciton are called quantum dots (QDs). QDs of the II-VI family have been investigated thoroughly. The synthesis and optical characterization of especially CdSe QDs have reached a mature level. Due to their bright and size-tunable emission over the entire visible range, colloidal CdSe QDs know already several applications, for example as phosphors in displays and TV screens.[1–3] On the long term, it will be required to replace the CdSe by a heavy metal-free compound. Colloidal QDs of the III-V family, especially InP QDs, may be appropriate for this, provided that their optical brightness and spectral tunability are similar to those of CdSe QDs. We should remark here that InP QDs can now be synthesized with safe and affordable precursors.[4] However, there are still considerable disadvantages related to the use of InP. First of all, bare InP cores have a low PL quantum efficiency; shells of ZnS, ZnSe, and ZnSe with low and variable amount of Cd have been developed to reduce the non-radiative surface recombination, which has resulted in promising photoluminescence quantum efficiencies as high as 60%.[4–6] Second, optical absorption and photoluminescence spectroscopy showed that InP QDs have a considerably broad emission spectrum with linewidths around 170 -190 meV, which would lower the color definition and resolution in displays, or require the use of filters. The broad spectral bandwidth of InP QDs is most probably related to inhomogeneous (size) broadening, but the fine structure of the lowest ($1S_h$, $1S_e$) exciton state, the exciton phonon coupling and the trap-associated emission pathway can be also important.[7,8]

With regard to the fine structure of InP QDs with a zinc blende or wurtzite structure, effective-mass theory[9] predicts that the lowest energy exciton (intrinsically eightfold degenerate) is split into five fine structure levels due to the interplay of the electron-hole exchange interaction, the intrinsic crystal field (in a wurtzite structure), and the crystal shape anisotropy.[9] The resulting exciton fine structure levels are characterized by their total angular momentum projection 'F'. For nearly spherical QDs, it is predicted that the lowest state should be $F = \pm 2$ (which is called 'dark' state because radiative recombination from it is electric dipole forbidden), followed by two states with $F = \pm 1$ (which is called 'bright' state because radiative recombination from it is allowed), and two with $F = 0$ (one optically dark and one optically bright). The relative order of the exciton states is determined by the crystal shape asymmetry.[9–11] In this respect, it should be remarked that the shape of the InP cores in the core-shell systems is not known, while the overall core-shell crystal has the shape of a tetrahedron for thick II-VI shells. The (thick) passivating shells around the InP core can also strongly influence the extension of the electron and hole wave functions, and in this way the electron-hole exchange energy and, hence, the exciton fine structure.[12] In addition, shells of different II-VI compounds have a variable lattice mismatch with the facets of the InP nanocrystals. The resulting interfacial strain might be a factor of importance, both for the PL quantum yield, spectral width and details

of the fine structure. It is thus of large importance, to investigate the fine structure energy levels of InP QDs as a function of the chemical composition and thickness of the shells.

Here we report on the exciton fine structure of InP core/ II-VI shell systems, with InP cores of 3.0±0.1 nm in diameter and 5-7 nm thick shells of ZnSe and (Cd,Zn)Se with variable amounts of Cd (5 and 9%). The incorporation of small amount of Cd in the ZnSe shell reduces the heteroepitaxial strain because it decreases the lattice mismatch between the InP core (lattice constant = 5.87 Å) and the shell (lattice constant increases from 5.68 Å for pure ZnSe to 6.08 Å for pure CdSe).[13] It also increases the degree of delocalization of the electron wave function into the shell and therefore the electron-hole exchange interaction is reduced. We use FLN spectroscopy to reduce the inhomogeneous spectral broadening. Furthermore, we vary the magnetic field from 0 to 30 T in order to induce a Zeeman splitting in the spin degenerate fine-structure-states.[8,14–17] A bright $\mathrm{F} = \pm 1$ level splits into $\mathrm{F} = +1$ and $\mathrm{F} = -1$ states, crossing in energy a lower bright $\mathrm{F} = 0$ level at some specific field. Furthermore, the decay from the dark state is enhanced by interaction with acoustic phonons and with optical phonons from both the InP core and the II-VI compound shell. We observe that the exciton fine structure remains roughly unchanged with the amount of Cd (0 - 9%) incorporated in the ZnSe shell.

6.2 Results and discussion

6.2.1 Basic optical characterization

We present results for three InP-based core/shell QD samples with the same InP core, 3.0±0.1 nm in diameter, passivated with shells, 10-15 nm in thickness, made from ZnSe and (Cd,Zn)Se with 5% and 9% Cd. The samples were synthesized with safe and affordable precursors and present a PL quantum yield of ~60%.[5]

In Figure 6.1a and b, we show the photoluminescence (PL) spectra of the three samples, at room temperature (RT) and 4 K, respectively. At room temperature, the InP/ZnSe sample shows maximum PL intensity at 2.06 eV; with increasing Cd content the PL peak shifts to lower energies, the emission maximum lying at 1.96 eV for the sample with 9% Cd. The full width at half maximum of the PL peak is 160 meV for all samples. The emission shifts gradually to higher energy upon decreasing temperature, reaching a blue shift of 60 meV at 4 K, due to the contraction of the crystal lattice.[18] At this temperature a lower energy tail becomes evident in the PL spectra, increasing with the Cd content. The full width at half maximum decreases to 140 meV, which points to a considerable inhomogeneous broadening.

The PL decay at room temperature (Figure 6.1c, measured at the peak maximum) shows a lengthening of the exciton radiative lifetime with increasing Cd content. On a short time range up to a delay time of 100 ns, the PL decays are nearly single-exponential, with lifetimes ranging from τ = 50.0 ns for the InP/ZnSe sample, to 55.9 and 65.9 ns for the samples with 5% and 9% Cd respectively. For delay times beyond 100 ns, the PL decay curves deviate from the single-exponential and the emission is dominated by a 'delayed

component'. Also the contribution of the delayed emission increases with increasing Cd content.

At 4 K (Figure 6.1d) the PL decay curves show an initial fast component, which we ascribe to emission from higher-energy bright states shortly after the laser pulse and prior to thermalization.[8,19,20] The long component is attributed to radiative recombination mostly from the dark exciton state. We estimate the radiative lifetimes at 4 K from a single-exponential fit of the PL decay curves, excluding the initial fast component. We find that the radiative lifetime at 4 K is longer than at room temperature and decreases from 159 ns for the InP/ZnSe QDs to 157 ns for InP/(Cd,Zn)Se QDs with 9% Cd. A more detailed discussion of the photoluminescence decay of these samples is given in Chapter 5.

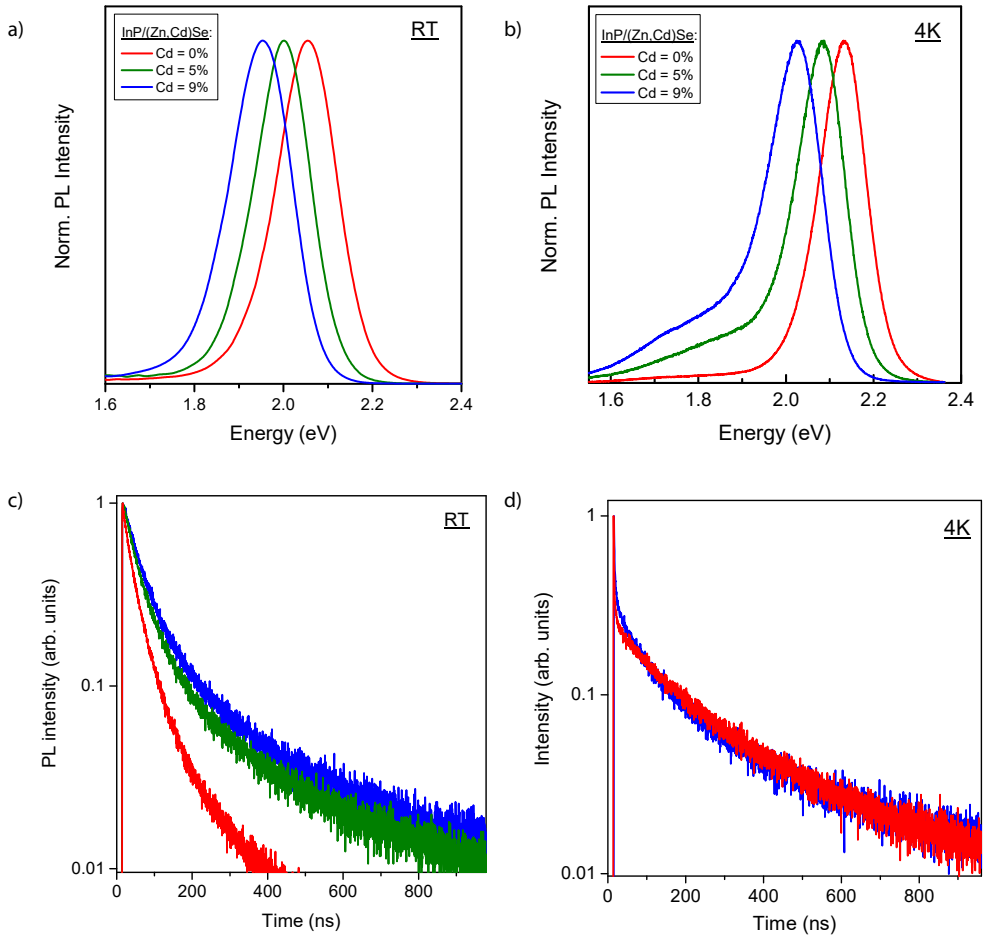

Figure 6.1. Basic optical properties of the studied InP/(Zn, Cd) Se core/shell QDs with 0, 5, or 9% Cd. a) PL spectra at room temperature, b) PL spectra at 4 K, c) Photoluminescence decay measured at the maximum of the PL peak at room temperature, d) Photoluminescence decay measured at 4 K at the maximum of the PL spectrum at 4 K.

6.2.2 Fluorescence line narrowing spectroscopy at variable magnetic field

We performed Fluorescence Line-Narrowing (FLN) spectroscopy at 4 K in order to reduce the inhomogeneous line broadening such that the fine structure in the emission can be resolved. FLN is an energy-selective technique that uses monochromatic laser light for excitation. If the laser photon energy matches the low-energy side of the absorption spectrum, the photoluminescence is due to a narrow sub-ensemble of very similar core-shell QDs emitting at the lowest energy. In other words, with a monochromatic laser a resonant fine structure state with high oscillator strength is excited; in the present case the bright $\mathrm{F} = \pm 1$ state. Relaxation towards lower states in the fine structure, followed by radiative recombination should then result in a spectrum composed of narrow emission peaks, revealing the lower exciton states with their phonon side bands. Furthermore, an external magnetic field splits the $\mathrm{F} = \pm 1$ state, and excitation with right (σ^+) or left (σ^-) circularly polarized light predominantly excites either the $\mathrm{F} = +1$ or $\mathrm{F} = -1$ state.

Figure 6.2 shows the FLN spectra of the InP/ZnSe QDs sample, under excitation at 602 nm (2.1 eV) in cross polarization configuration, *i.e.* σ^+ circularly polarized light is used for excitation (therefore predominantly exciting the upper $\mathrm{F} = +1$ state), while σ^- circularly polarized emission is detected. All the FLN spectra reported here are referred to the resonantly excited state (the bright $\mathrm{F} = +1$ state), which is set to zero and $\Delta\mathrm{E}$ indicates the relative emission energy from the laser line.

Figure 6.2a shows the FLN spectra at various magnetic fields from 8 T to 30 T, zoomed in on the energy range just below excitation. Two sharp optical transitions can be observed; the first one (marked as 'A'), becomes visible above 16 T and shifts linearly from $\Delta\mathrm{E}$ = 2 meV to lower energies with increasing field, reaching a value of $\Delta\mathrm{E}$ = 3.5 meV at 30 T. A second feature, (marked as 'B') becomes visible above 8 T, and shifts more steeply to lower energies with increasing field, reaching a value of $\Delta\mathrm{E}$ = 7.5 meV at 30 T. In Figure 6.2b, the same set of FLN spectra are presented but now for a broader energy range, revealing three other features designated as 'D', 'E' and 'F'. The peak 'D' has been already ascribed in a previous work to emission from the dark state coupled to acoustic phonons.[8] The two lower energy peaks ('E' and 'F') have been identified as vibronic replicas originating from coupling of the dark state with optical phonons in the ZnSe shell and InP core.[8] Notice that similar features are observed in the spectra of InP/ZnSe core/shell QDs with a different core size between 2.9 nm and 3.1 nm (see Appendix Figures A6.1 and A6.2).

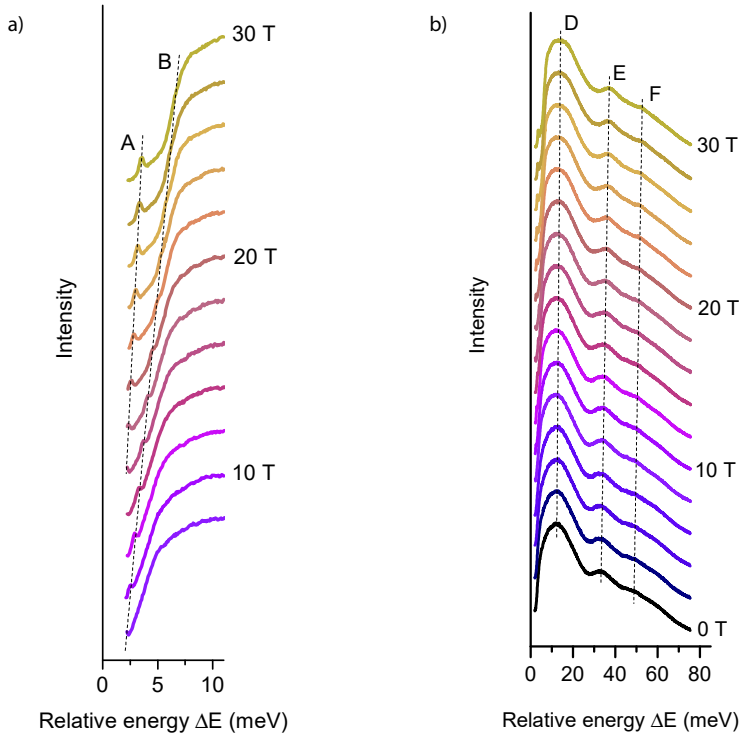

Figure 6.2. FLN spectra at low temperature (4 K) of the InP/ZnSe sample, excited with circular right polarization (σ^+) at 602 nm. The resonantly excited state (2.1 eV) is taken as reference and set to 0 meV, and the emission intensity is plotted as a function of $\Delta E = E_{laser} - E_{detected}$. The spectra are vertically shifted for clarity. a) Spectra at various fields from 8 T to 30 T, zoomed at the low energy range to highlight the peaks designated as A and B. b) Spectra at various fields from 0 T to 30 T, full energy range to show the main features designated as D, E and F.

In Figure 6.3, we present the FLN spectra obtained for the InP QDs with a (Zn,Cd)Se shell in which 5% Cd is incorporated. Also this sample was excited at 602 nm (2.1 eV) in cross polarization configuration, using σ^+ circularly polarized light, thus exciting the upper $F = +1$ state, while detecting the σ^- circularly polarized emission. Panel a in Figure 6.3 presents the spectra closest to the excitation energy. Three optical transitions are visible: the first one (marked as A), is visible above 16 T, and shifts to lower energies with increasing field, from $\Delta E = 2$ meV to $\Delta E = 3.2$ meV at 30 T. A second feature, (marked as B) becomes evident at 8 T and shifts more steeply to lower energies, reaching a value of $\Delta E = 6.2$ meV at 30 T. The third feature (marked as C) is directly visible at zero field with an energy of $\Delta E = 4.9$ meV and shifts downwards reaching $\Delta E = 7.6$ meV at 30 T. Figure 6.3b shows the results over a broader energy range. The three main features are indicated as D, E and F. The peak D is ascribed to emission from the dark state coupled to acoustic phonons; the lower energy peaks E and F are phonon replicas of the dark state due to coupling with the optical phonons of the ZnSe shell and the InP core, respectively.[8] The results are very similar to those obtained with InP QDs with a ZnSe shell shown in Figure 6.2 and Appendix Figures A6.1 and A6.2.

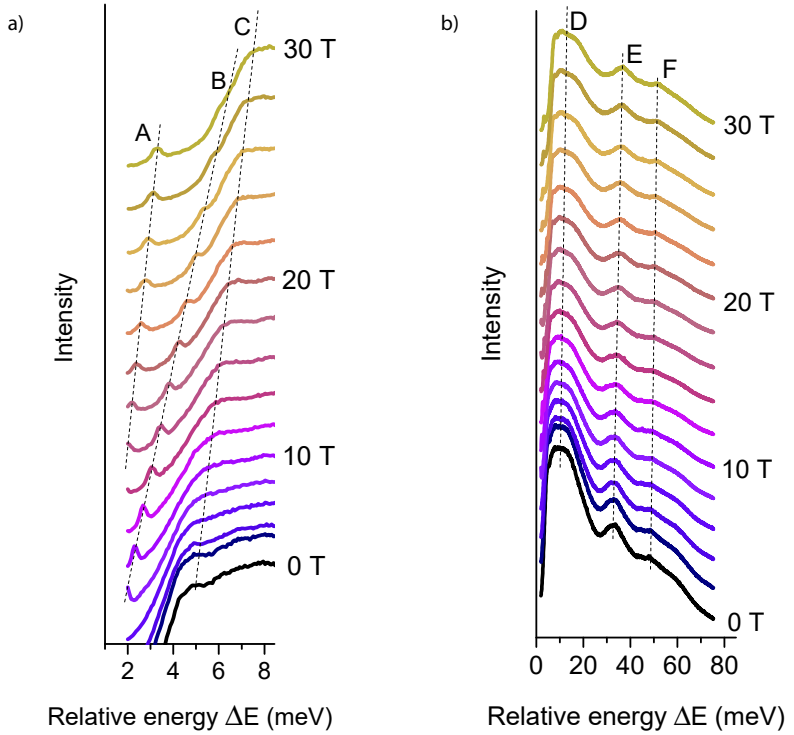

Figure 6.3. FLN spectra at low temperature (4 K) of the InP/($Cd_{0.05}Zn_{0.95}$)Se sample, excited with circular right polarization (σ^+) at 602 nm. The resonantly excited state (2.1 eV) is taken as reference and set to 0 meV, and the emission intensity is plotted as a function of $\Delta E = E_{laser} - E_{detected}$. The spectra are vertically shifted for clarity. a) Spectra at various magnetic fields from 8 T to 30 T, zoomed at the low energy range to highlight the peaks designated as A, B and C. b) Spectra at various fields from 0 T to 30 T, full energy range to show the main features designated as D, E and F.

Figure 6.4 summarizes the evolution of the peak energies with applied magnetic field as observed in the FLN spectra, for the InP/(Zn,Cd)Se core/shell QDs that we have studied (*i.e.* with a pure ZnSe shell, and with ZnSe shells with 5 and 9% Cd incorporated). The FLN spectra of the latter sample are shown in the Appendix Figure A6.3 and A6.4. Figure 6.4 shows that the relative energies of the exciton fine structure states with respect to the laser excitation line almost do not change when Cd is incorporated in the ZnSe shell. The transition 'A' shows an energy shift with increasing magnetic field with respect to the $F = +1$ state with a slope $\Delta E/\Delta B = 0.1$ in all samples (fittings can be found in Appendix Figure A6.5). Importantly, the results indicate a value of $\Delta E = 0.6$ meV (average over the three samples) at zero magnetic field (B = 0) obtained by linear extrapolation. We attribute this emission to a bright $F = 0$ state, slightly lower in energy than the $F = +1$ state (see Figure 6.5). From this $F = 0$ state, unpolarized emission is expected when all the randomly oriented InP QDs have equal probability to absorb a σ^+ phonon. However, QDs that are aligned with the main symmetry axis parallel to the laser excitation direction have a higher probability of absorbing a σ^+ photon with energy resonant with the $F = +1$ state. Due to this, the emission from the F = 0 state can also obtain some preferential linear polarization (see eq. 2.21 and 2.22 in Chapter 2).[9] The transitions marked as 'B' in Figure

6.4a, exhibit a steeper shift to lower energy with magnetic field, with $\Delta E/\Delta B = 0.2$ (fittings for the different samples and excitations can be found in the Appendix, Figures A6.6). The shift of this state extrapolates to almost zero ($\Delta E = 0.1$ meV) at zero field. We ascribe this emission to the bright $F = -1$ state that shifts to lower energy (with respect to the excited $F = +1$) twice as steep as the $F = 0$ state, because the Zeeman splitting lifts the exciton spin degeneracy only of the $F = \pm 1$ and $F = \pm 2$ states. From this linear Zeeman splitting, we deduce a Landé gyromagnetic factor $g = 3.5$, identical for all three samples and thus independent of the Cd content in the shell (see Appendix Figure A6.6). This g-factor value is in good agreement with values previously reported for InP based QDs.[8,21,22] A third transition marked as 'C' in Figure 6.4a for the InP/($Cd_{0.05}Zn_{0.95}$)Se and InP/($Cd_{0.09}Zn_{0.91}$)Se QDs, is attributed to the zero phonon line of the $F = -2$ dark state (see energy scheme in Figure 6.5). At zero magnetic field, the energy shift $\Delta E = 4.7$ meV with respect to the $F = +1$ state, corresponds to the bright-dark splitting Δ_{bd}. Remarkably, the bright-dark splitting does not depend on the Cd content in the ZnSe shell, despite that there is a trend towards a Type $I^{1/2}$ exciton localization regime with increasing Cd content in the shell (*i.e.*, the electron wavefunction gradually extends into the shell, while the hole wavefunction remains localized in the core). Furthermore, the peak emission energy of this transition shows a non-linear evolution as a function of the magnetic field applied. Indeed, at low fields its spectral position is roughly constant up to 6 T, while at higher magnetic fields the peak shifts linearly to lower energy with increasing field. This peculiar behavior is also observed in the FLN spectra of InP/ZnSe core/shell QDs with different core sizes (Appendix Figures A6.1 and A6.2). Similar behavior was observed in self-assembled CdSe/CdS dot-in-rod heteronanocrystals with the main symmetric axis oriented parallel to the direction of the laser excitation, the detected emission and the applied field.[17] This has been attributed to an extra exchange interaction splitting (Δ_{xy}) of the bright $F = \pm 1$ state at zero magnetic field due to an anisotropy in the plane perpendicular to the c-axis of the nanorods.[17] We remark that such a zero-field splitting is also observed in the 'B' emission of our samples. At low field (<6 T), when the Zeeman splitting is smaller than the asymmetry splitting (Δ_{xy}), the $F = \pm 1$ levels are mixed. As a result, the excitation and consequent relaxation to the dark $F = -2$ state, can take place both from the bright $F = +1$ and $F = -1$ states, while at higher field (> 6 T) only the excitation and relaxation from $F = +1$ to the $F = -2$ state is possible.

In Figure 6.4b, we present the evolution of C, D, E and F peaks (with respect to the laser line) for increasing magnetic field. All four transitions shift to lower energy in a very similar way (see parallel dashed lines in Figure 6.4b), implying that they are all due to optical transitions from the same $F = -2$ state (see Figure 6.5). Thus, these three emissions are vibronic replicas of the $F = -2$ state coupling with different phonons: the transition marked as 'D' is identified as an acoustic phonon replica, while the transitions 'E' and 'F' are attributed to phonon replicas due to coupling with optical phonons of the shell and InP core, respectively.[8]

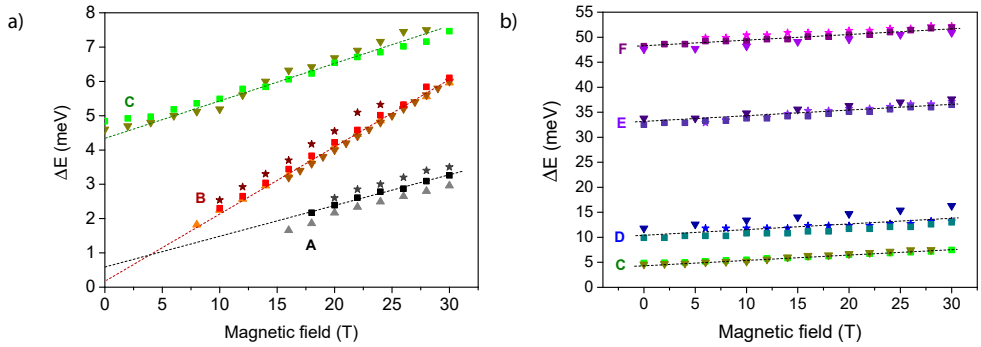

Figure 6.4. Peak energies of the most prominent transitions at 4 K as a function of the magnetic field obtained from various samples: InP/ZnSe (stars), InP/($Cd_{0.05}Zn_{0.95}$)Se (squares), InP/($Cd_{0.09}Zn_{0.91}$)Se (triangles: down - excitation at 602 nm, up – excitation at 632 nm). Energy peak extracted respectively from fluorescence line-narrowing measurements at 4 K shown in Figures 6.2 and 6.3, and Appendix Figures A6.3 and A6.4). The dashed-lines are guides to the eye. a) Zero-Phonon-Line transitions: A (black/grey symbols) from the $F = 0$ level, B (brown/red) from the $F = -1$ level and C (green) from the $F = -2$ level. b) Phonon replicas of the last dark state (C transition): D (blue), coupling with acoustic phonons; E (violet), coupling with optical (Cd,Zn)Se phonons and F (magenta), coupling with optical InP phonons.

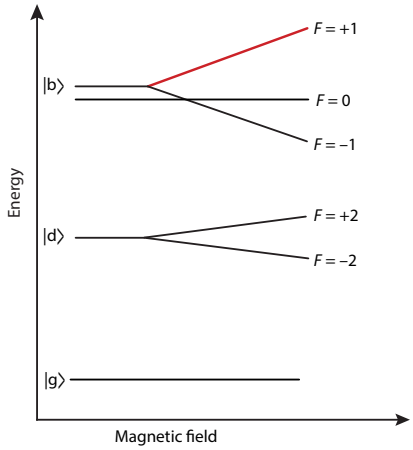

Figure 6.5. Field dependent energy level scheme used to interpret the data. It shows the ground state |g⟩ and the excited bright |b⟩ and the dark |d⟩ states. The lowest excited state is a dark $F = \pm 2$ state that splits in an $F = +2$ and an $F = -2$ state due to the Zeeman effect under magnetic field. Above the dark state, a bright $F = 0$ state close in energy to an upper $F = \pm 1$ state which cross the $F = 0$ state due to the Zeeman splitting under magnetic field. No anti-crossing effect was detected.

Summarizing, incorporating small amounts of Cd (≤ 9%) in the ZnSe shell, we observe a gradual redshift of the PL spectra and lengthening of the PL decay at room temperature. These effects suggest a gradual delocalization of the electron wavefunction into the shell with increasing Cd content, while the hole wavefunction remains localized in the core. Indeed admixing Cd into a ZnSe shell reduces the conduction-band offset between the InP core and the (Cd,Zn)Se shell,[5,23,24] with a resulting reduction of the quantum confinement potential for the electron wavefunction and increasing the degree of electron–hole

spatial separation.[12,25–27] Besides, addition of Cd in ZnSe shell increases the lattice constant of the shell, minimizing the strain between the InP core and the shell. The effect of high concentrations of Cd (up to 100% Cd) has been investigated in previous work on strain engineering.[13] Despite the effects of Cd addition into the shell on the PL spectra and PL decay, we observe here that the exciton fine structure remains roughly unchanged. This limited change of the exciton fine structure with the chemical composition of the shell may point to a dominant role of the hole (which remains confined in the core) in the determining the exciton fine structure. An alternative explanation is that the delocalization of the electron wavefunction over the shell with increasing Cd content is not strong enough to significantly influence the exciton fine structure. In this context, the main effect of the electron delocalization over the shell is to increase the exciton-phonon coupling. Indeed, as discussed in Chapter 5, the gradual increase of the electron delocalization into the shell leads to increase of the exciton polarizability, thereby enhancing the coupling to polar lattice phonons through the Fröhlich interaction.[28–31] This is consistent with the shortening of the radiative lifetimes at 4 K with increasing Cd content. In fact, at 4 K the emission comes predominantly from the lower dark exciton fine structure state and the coupling with phonons plays an important role to enhance the radiative recombination rate.

6.3 Conclusion

We presented a study of the exciton fine-structure of three InP-based core/shell QD samples, all with same InP core of 3±1 nm and various shell compositions: ZnSe, $(Cd_{0.05}Zn_{0.95})Se$ and $(Cd_{0.09}Zn_{0.91})Se$. Using FLN spectroscopy in a varying magnetic field from 0 to 30 T, we observed that the lowest-energy fine structure exciton state is a $F = \pm 2$ dark state, from which radiative recombination is assisted by coupling to confined acoustic and optical phonons of the core and the shell of the QDs. This lowest-energy $F = \pm 2$ dark state is followed by a bright $F = 0$ state, which has not been observed previously. The upper bright state $F = \pm 1$ is 0.6 meV above the $F = 0$ state and 4.7 meV from the $F = \pm 2$ state.

6.4 Methods

Sample preparation. InP/ZnSe and InP/(Zn,Cd)Se core/shell QD samples were synthesized, following the method reported in ref. 5. The QD samples were washed by precipitation with methanol, isolated by centrifugation and redispersed in toluene and 1-dodecanethiol. To achieve a QDs film the solution was deposited using a *drop-cast* method, on crystalline silicon substrate for FLN measurements, and on a quartz substrate for PL and TrPL measurements.

PL and Time-resolved Photoluminescence (TrPL). The PL and the Time-resolved PL measurements were performed on QD films deposited on quartz substrates (see sample preparation above). In the PL measurements, the excitation was provided by a 450 W Xenon

lamp and the PL signal was dispersed by an Edinburgh Instruments FLS920 spectrometer equipped with double grating monochromators and detected by a Hamamatsu R928 photomultiplier tube (PMT). The Time-resolved PL decay measurements were performed monitoring the PL peak wavelength for all samples. The excitation was provided by a pulsed diode laser, operating at 405 nm with a repetition rate of 100 kHz. The Time-resolved PL curves were acquired by time-correlated single-photon counting using a Hamamatsu H7422 PMT. The average count rate was kept at 3% of the laser repetition rate, by adjusting the slit width. This low excitation fluence was used in order to maintain single photon statistics and avoid multiexciton formation.

To achieve low temperatures, samples were placed inside an optical ^{4}He cryostat (Oxford Instruments).

Fluorescence Line-Narrowing (FLN) measurements. FLN experiments at low temperatures were performed at the High Field Magnet Laboratory (Radboud University). For these experiments the samples used were QD films on crystalline silicon substrate (see sample preparation). The samples were mounted in a titanium sample holder on top of a three-axis piezo-positioner. The FLN measurements were performed using a narrow excitation source, achieved by using a tunable jet-stream dye (Rhodamine 6G) laser. This monochromatic laser beam was circularly polarized by means of a linear polarizer and a Babinet-Soleil compensator. The laser beam was focused on the sample by a singlet lens (10 mm focal length). The same lens was used to collect the PL emission and direct it to the detection setup (Backscattering geometry). The samples and optical probe were mounted inside a liquid-helium bath cryostat. The high-resolution FLN emission was detected in crossed polarization mode relative to the laser polarization by using a linear polarizer and a lambda-quarter wave plate. The resonant-PL emission was analyzed by a 0.5 m long triple-grating spectrometer (3∗1800 grooves/mm holographic gratings) in subtractive mode, equipped with a liquid nitrogen cooled CCD camera (Symphony-Horiba).

ACKNOWLEDGMENT: We acknowledge the support of the HFML-RU/FOM, member of the European Magnetic Field Laboratory (EMFL).

6.5 References

1 Wood, V.; Panzer, M. J.; Chen, J.; Bradley, M. S.; Halpert, J. E.; Bawendi, M. C.; Bulović, V. Inkjet-Printed Quantum Dot-Polymer Composites for Full-Color AC-Driven Displays. *Adv. Mater.* **2009**, *21*, 2151–2155.

2 Shirasaki, Y.; Supran, G. J.; Bawendi, M. G.; Bulović, V. Emergence of Colloidal Quantum-Dot Light-Emitting Technologies. *Nat. Photonics* **2013**, *7*, 13–23.

3 Lim, J.; Jun, S.; Jang, E.; Baik, H.; Kim, H.; Cho, J. Preparation of Highly Luminescent Nanocrystals and Their Application to Light-Emitting Diodes. *Adv. Mater.* **2007**, *19*, 1927–1932.

4 Tessier, M. D.; Dupont, D.; De Nolf, K.; De Roo, J.; Hens, Z. Economic and Size-Tunable Synthesis of InP/ZnE (E = S, Se) Colloidal Quantum Dots. *Chem. Mater.* **2015**, *27*, 4893–4898.

5 Dupont, D.; Tessier, M. D.; Smet, P. F.; Hens, Z. Indium Phosphide-Based Quantum Dots with Shell-Enhanced Absorption for Luminescent Down-Conversion. *Adv. Mater.* **2017**, *29*, 1700686.

6 Pietra, F.; De Trizio, L.; Hoekstra, A. W.; Renaud, N.; Prato, M.; Grozema, F. C.; Baesjou, P. J.; Koole, R.; Manna, L.; Houtepen, A. J. Tuning the Lattice Parameter of InxZnyP for Highly Luminescent Lattice-Matched Core/Shell Quantum Dots. *ACS Nano* **2016**, *10*, 4754–4762.

7 Janke, E. M.; Williams, N. E.; She, C.; Zherebetskyy, D.; Hudson, M. H.; Wang, L.; Gosztola, D. J.; Schaller, R. D.; Lee, B.; Sun, C.; *et al.* Origin of Broad Emission Spectra in InP Quantum Dots: Contributions from Structural and Electronic Disorder. *J. Am. Chem. Soc.* **2018**, *140*, 15791–15803.

8 Brodu, A.; Ballottin, M. V.; Buhot, J.; Van Harten, E. J.; Dupont, D.; La Porta, A.; Prins, P. T.; Tessier, M. D.; Versteegh, M. A. M.; Zwiller, V.; *et al.* Exciton Fine Structure and Lattice Dynamics in InP/ZnSe Core/Shell Quantum Dots. *ACS Photonics* **2018**, *5*, 3353–3362.

9 Efros, A.; Rosen, M.; Kuno, M.; Nirmal, M.; Norris, D.; Bawendi, M. Band-Edge Exciton in Quantum Dots of Semiconductors with a Degenerate Valence Band: Dark and Bright Exciton States. *Phys. Rev. B* **1996**, *54*, 4843–4856.

10 Nirmal, M.; Norris, D. J.; Kuno, M.; Bawendi, M. G.; Efros, A. L.; Rosen, M. Observation of the "Dark Exciton" in CdSe Quantum Dots. *Phys. Rev. Lett.* **1995**, *75*, 3728–3731.

10 Blokland, J. H.; Claessen, V. I.; Wijnen, F. J. P.; Groeneveld, E.; de Mello Donegá, C.; Vanmaekelbergh, D.; Meijerink, A.; Maan, J. C.; Christianen, P. C. M. Exciton Lifetimes of CdTe Nanocrystal Quantum Dots in High Magnetic Fields. *Phys. Rev. B* **2011**, *83*, 035304.

12 Granados del Águila, A.; Groeneveld, E.; Maan, J. C.; de Mello Donegá, C.; Christianen, P. C. M. Effect of Electron–Hole Overlap and Exchange Interaction on Exciton Radiative Lifetimes of CdTe/CdSe Heteronanocrystals. *ACS Nano* **2016**, *10*, 4102–4110.

13 Rafipoor, M.; Dupont, D.; Tornatzky, H.; Tessier, M. D.; Maultzsch, J.; Hens, Z.; Lange, H. Strain Engineering in InP/(Zn,Cd)Se Core/Shell Quantum Dots. *Chem. Mater.* **2018**, *30*, 4393–4400.

14 Wijnen, F. J. P.; Blokland, J. H.; Chin, P. T. K.; Christianen, P. C. M.; Maan, J. C. Competition between Zero-Phonon and Phonon-Assisted Luminescence in Colloidal CdSe Quantum Dots. *Phys. Rev. B* **2008**, *78*, 235318.

15 Micic, O. I.; Sprague, J. R.; Curtis, C. J.; Jones, K. M.; Machol, J. L.; Nozik, A. J.; Giessen, H.; Fluegel, B.; Mohs, G.; Peyghambarian, N. Synthesis and Characterization of InP, GaP, and GaInP2 Quantum Dots. *J. Phys. Chem.* **1995**, *99*, 7754–7759.

16 Babinski, A.; Potemski, M.; Christianen, P. C. M. Optical Spectroscopy on Semiconductor Quantum Dots in High Magnetic Fields. *Comptes Rendus Phys.* **2013**, *14*, 121–130.

17 Granados del Águila, A.; Jha, B.; Pietra, F.; Groeneveld, E.; de Mello Donegá, C.; Maan, J. C.; Vanmaekelbergh, D.; Christianen, P. C. M. Observation of the Full Exciton and Phonon Fine Structure in CdSe/CdS Dot-in-Rod Heteronanocrystals. *ACS Nano* **2014**, *8*, 5921–5931.

18 Haruna, K.; Maeta, H.; Ohashi, K.; Koike, T. The Thermal Expansion Coefficient and Gruneisen Parameter of InP Crystal at Low Temperatures. *J. Phys. C Solid State Phys.* **1987**, *20*, 5275–5279.

19 Biadala, L.; Siebers, B.; Beyazit, Y.; Tessier, M. D.; Dupont, D.; Hens, Z.; Yakovlev, D. R.; Bayer, M. Band-Edge Exciton Fine Structure and Recombination Dynamics in InP/ZnS Colloidal Nanocrystals. *ACS Nano* **2016**, *10*, 3356–3364.

20 Eilers, J.; Van Hest, J.; Meijerink, A.; Donega, C. D. M. Unravelling the Size and Temperature Dependence of Exciton Lifetimes in Colloidal ZnSe Quantum Dots. *J. Phys. Chem. C* **2014**, *118*, 23313–23319.

21 Langof, L.; Fradkin, L.; Ehrenfreund, E.; Lifshitz, E.; Micic, O. I.; Nozik, A. J. Colloidal InP/ZnS Core-Shell Nanocrystals Studied by Linearly and Circularly Polarized Photoluminescence. *Chem. Phys.* **2004**, *297*, 93–98.

22 De Luca, M.; Polimeni, A.; Fonseka, H. A.; Meaney, A. J.; Christianen, P. C. M.; Maan, J. C.; Paiman, S.; Tan, H. H.; Mura, F.; Jagadish, C.; *et al.* Magneto-Optical Properties of Wurtzite-Phase InP Nanowires. *Nano Lett.* **2014**, *14*, 4250–4256.

23 Norris, D. J.; Efros, A. L.; Erwin, S. C. Doped Nanocrystals. *Science.* **2008**, *319*, 1776–1779.

24 Donegá, C. D. M. Synthesis and Properties of Colloidal Heteronanocrystals. *Chem. Soc. Rev.* **2011**, *40*, 1512–1546.

25 de Mello Donegá, C.; Koole, R. Size Dependence of the Spontaneous Emission Rate and Absorption Cross Section of CdSe and CdTe Quantum Dots. *J. Phys. Chem. C* **2009**, *113*, 6511–6520.

26 Efros, A. L. Luminescence Polarization of CdSe Microcrystals. *Phys. Rev. B* **1992**, *46*, 7448–7458.

27 de Mello Donegá, C. Formation of Nanoscale Spatially Indirect Excitons: Evolution of the Type-II Optical Character of CdTe/CdSe Heteronanocrystals. *Phys. Rev. B* **2010**, *81*, 165303.

28 Shiang, J. J.; Risbud, S. H.; Alivisatos, A. P. Resonance Raman Studies of the Ground and Lowest Electronic Excited State in CdS Nanocrystals. *J. Chem. Phys.* **1993**, *98*, 8432–8442.

29 Lin, C.; Gong, K.; Kelley, D. F.; Kelley, A. M. Electron-Phonon Coupling in CdSe/CdS Core/Shell Quantum Dots. *ACS Nano* **2015**, *9*, 8131–8141.

30 Groeneveld, E.; De Mello Donegá, C. Enhanced Exciton-Phonon Coupling in Colloidal Type-II CdTe-CdSe Heteronanocrystals. *J. Phys. Chem. C* **2012**, *116*, 16240–16250.

(31) Cui, J.; Beyler, A. P.; Coropceanu, I.; Cleary, L.; Avila, T. R.; Chen, Y.; Cordero, J. M.; Heathcote, S. L.; Harris, D. K.; Chen, O.; *et al.* Evolution of the Single-Nanocrystal Photoluminescence Linewidth with Size and Shell: Implications for Exciton-Phonon Coupling and the Optimization of Spectral Linewidths. *Nano Lett.* **2016**, *16*, 289–296.

6.6 Appendix

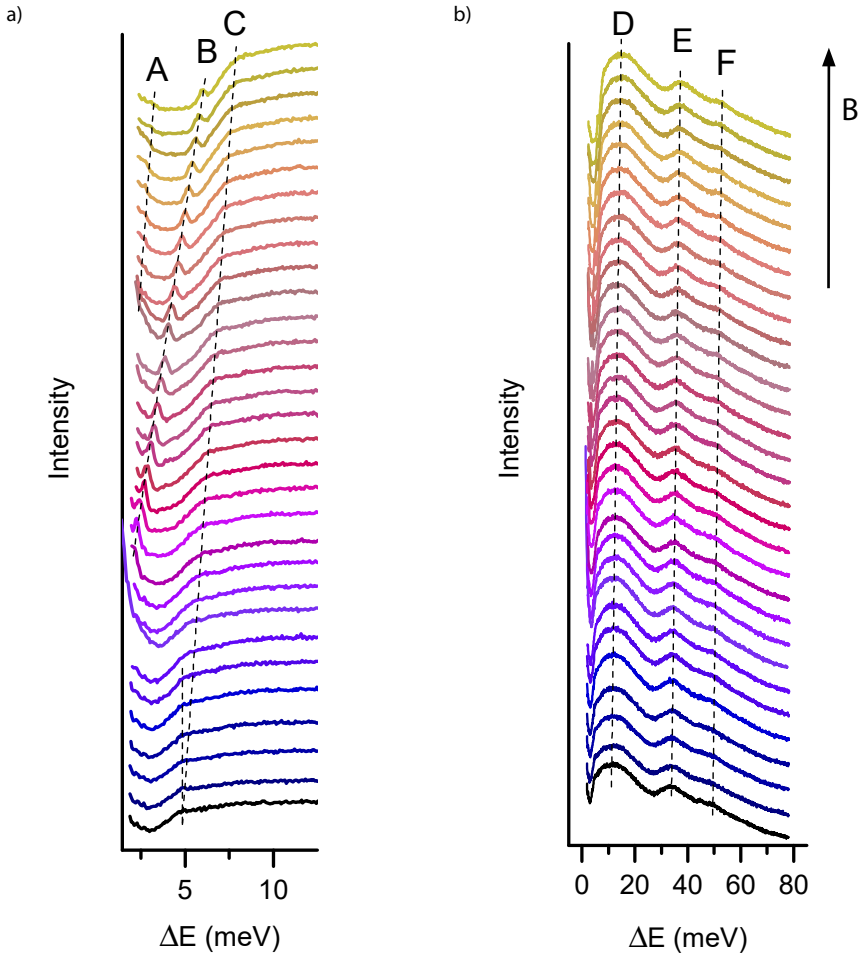

Figure A6.1: FLN spectra at low temperature (4 K) of the InP/ZnSe sample with 2.9 nm core diameter, excited with circular right polarization (σ^+) at 590 nm, at various fields from 0 T to 30 T. The resonantly excited state (2.1 eV) is taken as reference and set to 0 meV. The spectra are vertically shifted for clarity. a) Zoom-in at low energy. b) Full energy range.

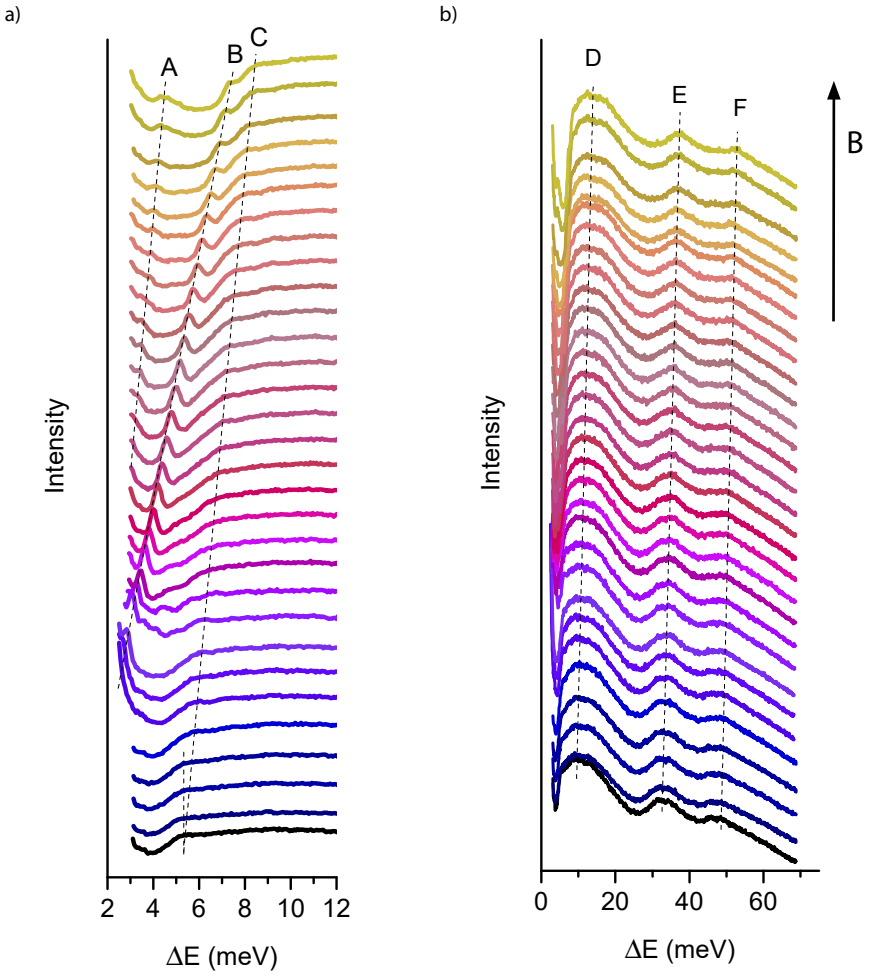

Figure A6.2: FLN spectra at low temperature (4 K) of the InP/ZnSe sample with 3.1 nm core diameter, excited with circular right polarization (σ^+) at 627 nm, at various fields from 0 T to 30 T. The resonantly excited state (2.0 eV) is taken as reference and set to 0 meV. The spectra are vertically shifted for clarity. a) Zoom-in at low energy. b) Full energy range.

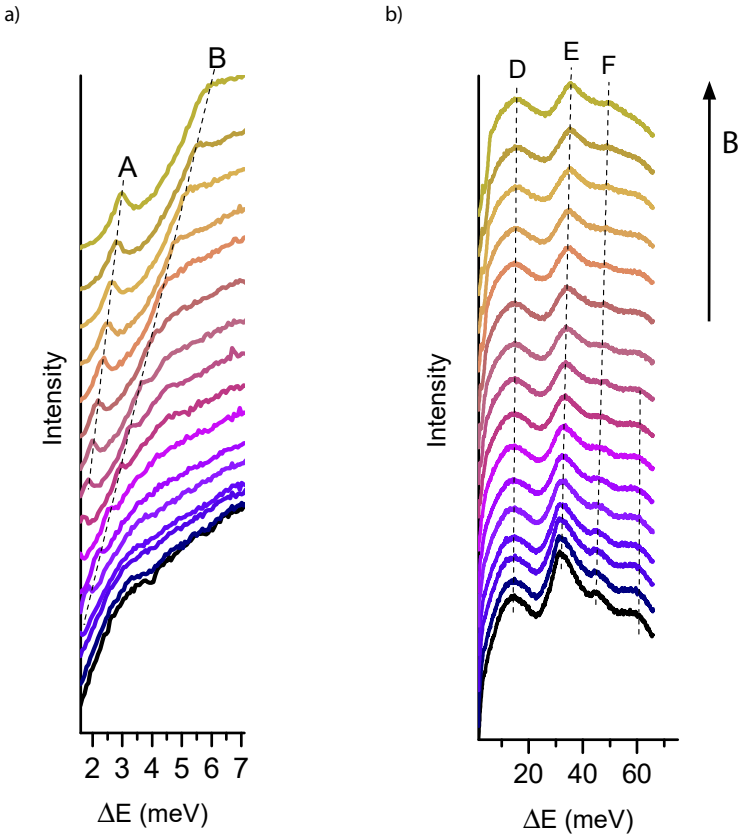

Figure A6.3: FLN spectra at low temperature (4 K) of the InP/($Cd_{0.09}Zn_{0.91}$) sample, excited with circular right polarization (σ^+) at 632 nm, at various fields from 0 T to 30 T. The resonantly excited state (2.0 eV) is taken as reference and set to 0 meV. The spectra are vertically shifted for clarity. a) Zoom-in at low energy. b) Full energy range.

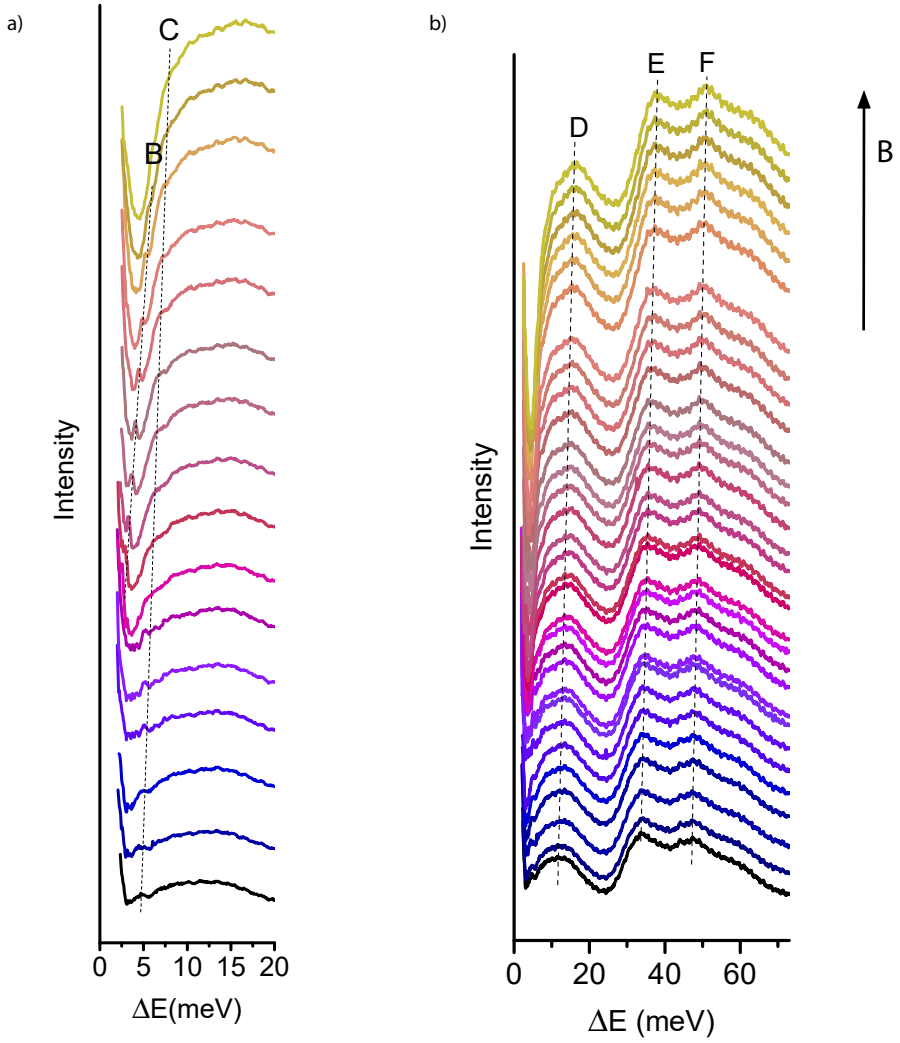

Figure A6.4: FLN spectra at low temperature (4 K) of the InP/($Cd_{0.09}Zn_{0.91}$) sample, excited with circular right polarization (σ^+) at 602 nm, at various fields from 0 T to 30 T. The resonantly excited state (2.1 eV) is taken as reference and set to 0 meV. The spectra are vertically shifted for clarity. a) Zoom-in at low energy. b) Full energy range.

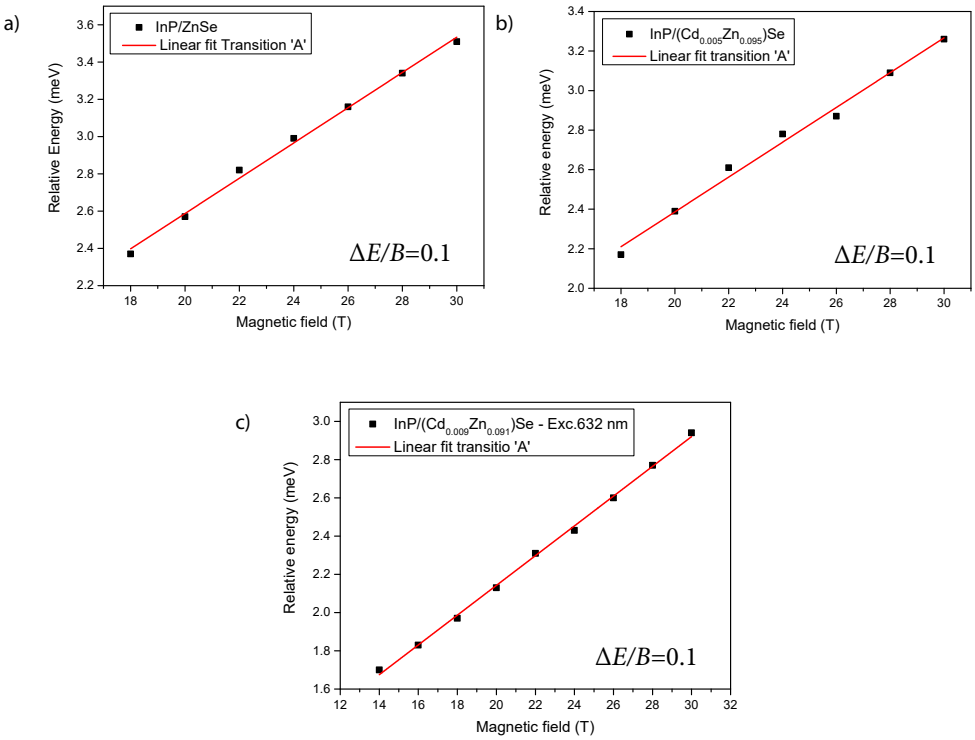

Figure A6.5: Peak energies as a function of magnetic field for the first peak, marked as 'A' in the FLN spectra. Linear fitting are shown with solid red line. a) InP/ZnSe QDs sample. b) InP/($Cd_{0.05}Zn_{0.95}$)Se QDs sample. c) InP/($Cd_{0.09}Zn_{0.91}$)Se QDs sample.

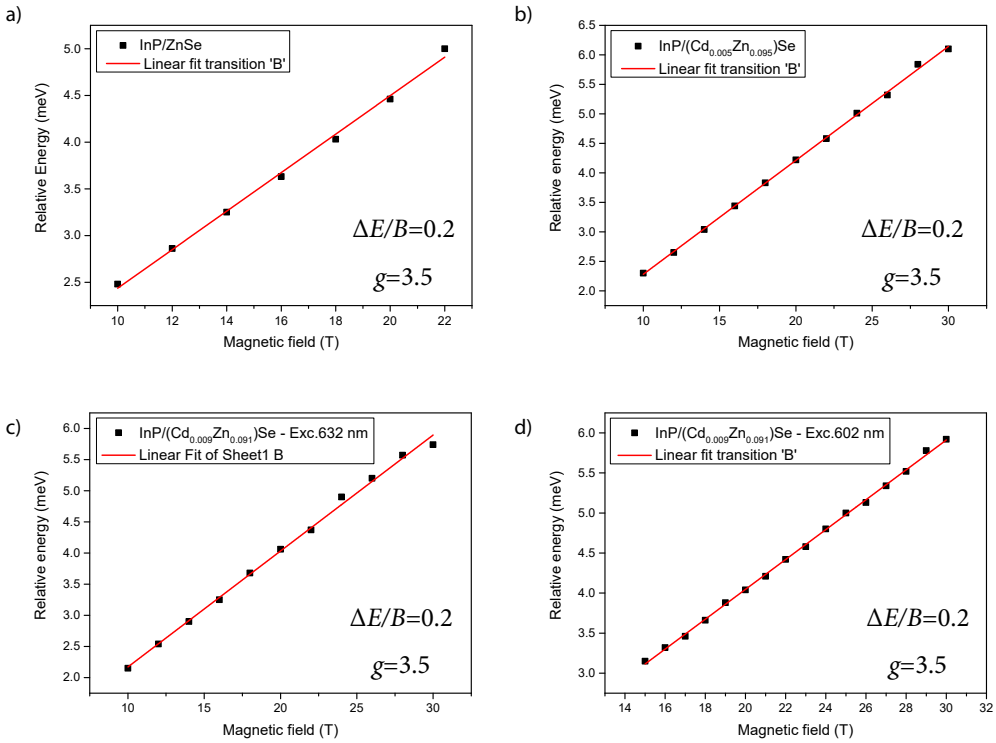

Figure A6.6: Peak energies as a function of magnetic field for the second peak, marked as 'B' in the FLN spectra. Linear fitting are shown with solid red line. a) InP/ZnSe QDs sample. b) InP/($Cd_{0.05}Zn_{0.95}$)Se QDs sample. c) InP/($Cd_{0.09}Zn_{0.91}$)Se QDs sample excited at 632 nm. d) InP/($Cd_{0.09}Zn_{0.91}$)Se QDs sample excited at 602 nm.

Chapter 7

Summary

Abstract

The work presented in this thesis has provided new insights in the physical mechanisms of the radiative emission in InP-based core/shell QDs. Specifically, it focuses on the investigation of the band-edge exciton fine structure and the related exciton recombination radiative emission, with an emphasis on the active role of the phonon coupling in the recombination process. This chapter summarizes the main results achieved in this thesis with an English, Dutch and Italian summary.

7.1 Summary in English

Colloidal quantum dots (QDs) are semiconductor nanocrystals with size- and shape-tunable optical properties, fundamentally different from those of the bulk, and of significant interest in optoelectronics. For decades, CdSe-based QDs have been the workhorses in this field and they have reached a very mature level with a bright and size-tunable photoluminescence in the visible range, making them very suitable for applications in LEDs, displays and TV screens. However, Europe's legislation does not allow the use of Cd-containing materials for opto-electronic applications. For this reason, the implementation of QDs in commercial devices requires to replace these QDs by toxicologically harmless materials, which should have a similar optical performance. In this respect, the development of III-V QDs, especially of InP, has received increasing attention in recent years. Colloidal hetero-nanocrystals composed of InP cores show a reasonable photoluminescence quantum yield, a size-tunable emission spectrum in the visible range and a good chemical stability, provided that they are coated with a suitable inorganic shell material. At present, suspensions of well-passivated InP core/shell QDs that can be scaled up to industrial production, are prepared by wet-chemical synthesis. They show bright emission ranging from the near-IR (1.5 eV) to the green (2.5 eV) spectral range with near-unity photoluminescence quantum yield.

It is thus very important to investigate the energy-level structure and optical properties of this promising class of nanocrystals. The optoelectronic properties of InP core/shell QDs are determined by the chemical nature of both the core and the shell materials, the strain induced on the core due to core/shell epitaxy, and the relative offsets between the conduction and valence band edges of the core and shell materials. The electron and hole can be both localized within the core, or one carrier can be localized in the core and the other in the shell. For all these reasons, the nature of the shell has a strong influence on the radiative processes.

This thesis aims to investigate these aspects in detail, providing a fundamental understanding of the physical mechanisms of spontaneous emission by unravelling the exciton fine-structure of InP core/shell nanocrystal quantum dots, and by studying how the exciton recombination depends on the size of the nanocrystals, the shell composition and core/shell structure.

Optical spectroscopy under high magnetic field and low temperature forms a powerful method to study the exciton fine structure in all detail. High magnetic fields are essential to obtain a considerable Zeeman splitting of the spin-degenerate fine-structure states with different total angular momentum projection F. We employed (time-resolved) photoluminescence spectroscopy at varying magnetic field with good spectral and polarization resolution, in order to characterize the exciton fine-structure states, and their interaction with the lattice phonons of the core and the shell.

The exciton fine-structure of InP/ZnSe core/shell QDs is presented in **chapter 3**. Photoluminescence (PL) decay at varying temperatures, from 10 mK to 300 K, reveals that the lowest exciton state is dark, with a bright state situated about 4–7 meV above this dark state; the bright-dark energy splitting increases with decreasing core size. Raman spectroscopy combined with circularly polarized fluorescence line-narrowing (FLN) spectroscopy at 4 K under varying magnetic field (up to 30 T), demonstrates that radiative recombination from the lowest dark $\mathrm{F} = \pm 2$ state involves acoustic and optical phonons, both from the InP core and the ZnSe shell. Furthermore, we provide evidence that the highest FLN peak is, in fact, an acoustic phonon replica of the dark state rather than a zero-phonon line. This is in marked contrast with the fine structure spectrum of CdSe QDs for which a strong zero-phonon-line signal was observed.

The effect of a different shell material on the exciton fine structure and the exciton-spin dynamics is presented in **chapter 4**, where we report a study of the time-, spectral- and polarization- resolved optical properties of InP QDs with a ZnS shell, under high magnetic field up to 30 T at 4 K. Here again, the lowest exciton state is a forbidden dark state that almost exclusively decays in a phonon-assisted process. FLN spectra and the PL decay analysis demonstrate that mixing of this dark state with the nearest allowed bright state does not occur, up to the highest magnetic fields applied. The photoluminescence decay time even increased with increasing magnetic field. This was observed in all InP-based QDs studied, independently of the surrounding shell. Furthermore, the time-resolved degree of circular polarization of the dark exciton shows a very slow spin relaxation time and saturates at values around 16%. These results show again a marked contrast with CdSe QDs and other colloidal nanocrystals.

The role of the shell composition and core/shell structure in the exciton recombination dynamics of InP-based QDs is presented in **chapter 5**, where we show how the exciton–phonon coupling in InP QDs is influenced by various shells: ZnS, ZnSe and (Zn,Cd)Se with different amounts of Cd (5%, 9%, 12%). Comparing the phonon energies extracted from Raman spectroscopy measurements with the exciton emission peaks observed in FLN spectra, we determined the position of both the bright $\mathrm{F} = \pm 1$ state and the lowest dark $\mathrm{F} = \pm 2$ exciton fine structure state in the different core/shell structures. The phonon modes involved in the radiative recombination of the dark state are both acoustic and optical. Exciton-phonon coupling enhances the radiative decay of the dark state to the ground state. The degree of exciton-phonon coupling depends on the shell material: for example, electron wavefunction delocalization into the shell increases the exciton polarizability, strengthening the coupling to polar lattice phonons through the Fröhlich interaction.

In **chapter 6**, the exciton fine structure in relation to the electron wavefunction delocalization into the shell has been studied in more detail, using shells of ZnSe or (Cd,Zn)Se with 5 and 9% Cd. The admixing of Cd into the ZnSe shell decreases the bandgap of the shell, reducing in this way the conduction-band offset of the core/shell system, thus resulting in more delocalization of the electron wavefunction into the shell with increasing Cd content. Notice that the hole wavefunction remains localized in the

core. Using FLN spectroscopy under external magnetic field up to 30 T, we found that under magnetic field the bright $F = \pm 1$ level splits into $F = +1$ and $F = -1$ states, crossing in energy a lower bright $F = 0$ level, which has not been observed previously. The exciton fine structure remains roughly unchanged with the amount of Cd (0 - 9%) incorporated in the ZnSe shell, probably due to a dominant role of the hole in determining the exciton fine structure.

In conclusion, we found that the exciton dynamics in InP-based QDs deviates substantially from that in II-VI nanocrystals. All InP core/shell systems that we studied have a dark $F = \pm 2$ state as lowest state. From this state, direct radiative recombination to the ground state is electric dipole forbidden. The observed very slow decay of this dark state is almost exclusively due to phonon-assisted processes by optical and confined acoustic phonons. The exciton-phonon coupling strength depends on the shell material, which can be understood by considering the variable degree of exciton polarizability. We notice here that we also observed emission from a bright $F = 0$ level, close in energy to the bright $F = \pm 1$ state, a process that was overlooked so far. We observe furthermore that InP-based QDs show a complete absence of field-induced mixing between the bright and the dark states. These remarkable features will be studied in follow-up research.

7.2 Nederlandse Samenvatting

Zogenaamde "quantum punten" zijn colloïdale nanokristallen met optische eigenschappen die bepaald worden door de grootte en vorm van het nanokristal, dus sterk verschillend van het overeenkomstig bulk materiaal, en van groot belang voor toepassingen in opto-elektrische componenten. Sinds tientallen jaren worden vooral nanokristallen van de halfgeleider CdSe onderzocht en gebruikt; deze materialen zijn nu behoorlijk geoptimaliseerd, en CdSe nanokristallen worden gebruikt in licht-emitterende diodes (LEDs), displays, en TV schermen. De Europese wetgeving laat echter het gebruik van Cd-bevattende materialen in opto-elektrische componenten niet toe. Daarom zijn vervangende halfgeleider samenstellingen nodig die minder schadelijk zijn voor de gezondheid. Colloïdale hetero-nanokristallen met een kernkristal van het III-V materiaal InP vertonen luminescentie met een behoorlijke quantum opbrengst, op voorwaarde dat er rond de kern een epitaxiale schil van een andere halfgeleider aanwezig is die zorgt voor elektronische passivatie. Tegenwoordig kan de synthese van deze colloïdale hetero-nanokristallen opgeschaald worden tot een niveau dat interessant is voor de industrie. InP kern/schil systemen vertonen een goede emissie die gevarieerd kan worden tussen het nabije IR (1.5 eV) tot aan het groen (2.5 eV).

Het is dus van groot belang om de energieniveaus en optische eigenschappen van deze veelbelovende klasse van hetero-nanokristallen in detail te bestuderen. De optische eigenschappen worden bepaald door de chemie van de kern en schil, de kern-schil mismatch in de kristalstructuur die een rekspanning veroorzaakt, en het energie verschil tussen de elektronen (gaten) niveaus van de kern en de schil, bepalend voor de (de)lokalisatie van de exciton golffunctie. Het is namelijk zo dat in een InP kern/schil

systeem, de absorptie van een foton kan leiden tot een elektron en gat in de kern, maar eventueel ook tot een verwijdering tussen het elektron en het gat omdat één ervan in de kern is gelokaliseerd en de andere in de schil. Vanwege deze reden -en nog verschillende andere (vide infra)- is de InP kern/schil atomaire structuur van groot belang voor de optische eigenschappen.

De thesis bestudeert deze aspecten in detail, om zo tot een begrip te komen van de fysische mechanismen van spontaan exciton verval en lichtemissie door de spin fijn-structuur van het exciton te ontrafelen, en te bestuderen hoe deze fijn-structuur afhangt van de grootte van de InP kern en van de kern/schil chemie.

Optische spectroscopie onder een variërend en sterk magneetveld en lage temperatuur is een krachtige methode voor het bestuderen van de exciton fijn-structuur. We hebben een sterk magneetveld nodig om meervoudige toestanden te splitsen in enkelvoudige toestanden, elk met een verschillend spin-hoek moment F. Wij hebben (tijdopgeloste) fotoluminescentie spectroscopie gebruikt onder een variërend magneetveld, en we hebben ook de energie en polarisatie van het uitgezonden foton met een goede resolutie gedetecteerd. Op die manier konden we de exciton fijn-structuur toestanden karakteriseren, en hun interactie met rooster vibraties van de InP kern en de schil in kaart brengen.

De exciton fijn-structuur van InP/ZnSe kern/schil nanokristallen wordt bestudeerd in **hoofdstuk 3**. Tijdopgeloste fotoluminescentie metingen zijn gedaan bij temperaturen van 10 mK tot 300 K en tonen aan dat de laagste exciton toestand donker is en dat 4-7 meV hierboven een heldere toestand aanwezig is. Deze helder-donker splitsing neemt toe met afnemende kern grootte. Raman spectroscopie in combinatie met circulair gepolariseerd fluorescentie lijn vernauwing (FLV) spectroscopie onder een variërend magneetveld (tot 30 T) bij 4 K toont aan dat stralende recombinatie vanuit de laagste donkere $F = \pm 2$ toestand gekoppeld is met akoestische en optische fononen, uit zowel de InP kern als de ZnSe schil. Verder leveren we bewijs dat de hoogste FLV piek een akoestische fonon replica is van de donkere toestand in plaats van een zero-fonon lijn. Dit is in scherpe tegenstelling met het fijn-structuur spectrum van CdSe nanokristallen, waar een sterke nulde-fonon lijn is waargenomen.

Het effect van verschillende schil materialen op de exciton fijn-structuur en de exciton spin dynamica wordt besproken in **hoofdstuk 4**. Hier bespreken we resultaten van tijd-, spectraal- en polarisatie- opgeloste optische eigenschappen van InP nanokristallen met een ZnS schil onder hoge magnetische velden (tot 30 T) bij 4 K. Opnieuw is hier de laagste exciton toestand een verboden donkere toestand die bijna alleen maar vervalt via fonon geassisteerde processen. FLV spectra en tijdopgeloste fotoluminescentie metingen tonen aan dat menging van deze donkere toestand met de meest dichtbije toegestane heldere toestand niet plaats vindt, zelfs niet bij het hoogste magnetische veld. De tijdopgeloste fotoluminescentie vervaltijd nam zelfs toe met een toename in de sterkte van het magnetische veld. Deze waarneming geldt voor alle InP-bevattende nanokristallen, onafhankelijk van het schil materiaal. Verder toont de tijdafhankelijke mate van circulaire

polarisatie van de donkere exciton toestand een hele trage spin relaxatie tijd en saturatie bij ongeveer 16%. Deze resultaten zijn wederom in tegenstelling met CdSe en andere nanokristallen.

De invloed van de compositie van de schil en de kern/schil structuur op de exciton recombinatie dynamica in InP-bevattende nanokristallen wordt gepresenteerd in **hoofdstuk 5**. Hier tonen we hoe de exciton-fonon koppeling in InP-bevattende nanokristallen beïnvloed wordt door verschillende schil materialen, namelijk ZnS, ZnSe en (Zn,Cd)Se met verschillende hoeveelheden Cd (5%, 9%, 12%). Door het vergelijken van de fonon energieën uit Raman spectroscopie metingen bij 4 K met de exciton emissie pieken waargenomen in FLV spectra konden we de positie bepalen van zowel de heldere $\mathrm{F} = \pm 1$ toestand en de laagste donkere $\mathrm{F} = \pm 2$ fijn-structuur toestanden voor de verschillende kern/schil structuren. De fonon modi betrokken bij de stralende recombinatie van de donkere toestand zijn zowel akoestisch als optisch. Exciton-fonon koppeling verhoogt het stralend verval van de donkere toestand naar de grond toestand. De mate van exciton-fonon koppeling hangt af van het schil materiaal. Een voorbeeld is dat, wanneer de elektron golffunctie gedelokaliseerd raakt naar de schil, de exciton polariseerbaarheid toe neemt, dit versterkt de koppeling met polaire rooster fononen door de Fröhlich interactie.

In **hoofdstuk 6** is de exciton fijn-structuur in relatie tot de elektron golffunctie delokalisatie naar de schil in meer detail bestudeerd, dit is gedaan door het gebruik van schillen van ZnSe of (Cd,Zn)Se met 5 en 9% Cd. De bijmenging van Cd in de ZnSe schil verlaagt de bandkloof van de schil. Door deze verlaging wordt de afstand tussen conductieband van de kern en de schil kleiner. Dit resulteert erin dat het elektron meer gedelokaliseerd raakt over de schil bij een toename van de hoeveelheid Cd, terwijl het gat gelokaliseerd blijft in de kern. Door het gebruik van FLV spectroscopie onder magnetische velden tot 30 T, ontdekten we dat onder magnetisch veld het heldere $\mathrm{F} = \pm 1$ niveau opsplitst in $\mathrm{F} = +1$ en $\mathrm{F} = -1$ toestanden, kruisend in energie een lagere helder $\mathrm{F} = 0$ niveau, wat nog niet eerder is waargenomen. De exciton fijn-structuur blijft grofweg onveranderd met verschillende hoeveelheden Cd (0-9%) opgenomen in de ZnSe schil. Dit komt hoogstwaarschijnlijk door de sterke invloed van het elektron gat op de exciton fijn-structuur.

Tot slot hebben we ontdekt dat de exciton dynamica in InP-gebaseerde nanokristallen wezenlijk afwijkt van die in II-VI nanokristallen. Alle InP kern/schil systemen die we hebben bestudeerd hebben een donkere $\mathrm{F} = \pm 2$ toestand als laagste toestand. Vanuit deze toestand is direct stralende recombinatie naar de grondtoestand verboden. Het waargenomen hele trage verval van deze donkere toestand verloopt bijna uitsluitend door fonon geassisteerde processen met optische en begrensde akoestische fononen. Dat de exciton-fonon koppeling sterkte afhangt van het schil materiaal kan worden verklaard door de variabele mate van exciton delocalisatie. Wij merken hier op dat we ook emissie van een helder $\mathrm{F} = 0$ niveau, met vergelijkbare energie als de heldere $\mathrm{F} = \pm 1$ toestand, hebben waargenomen. Dit is iets wat tot nu toe over het hoofd was gezien. Verder nemen wij waar dat InP-gebaseerde nanokristallen een volledige afwezigheid tonen van veld geïnduceerde menging tussen de heldere en donkere toestanden. Deze opmerkelijke kenmerken zullen verder worden onderzocht in de toekomst.

7.3 Riassunto in Italiano

I '*quantum dots*' (QDs) sono nanocristalli di materiale semiconduttore con proprietà ottiche dipendenti dalla loro dimensione e forma. Tali proprietà sono fondamentalmente differenti da quelle del materiale '*bulk*' e particolarmente interessanti in optoelettronica. Per decenni i *quantum dots* a base di CdSe sono stati il cavallo di battaglia in questo campo, raggiungendo alte prestazioni con fotoluminescenza variabile nello spettro del visibile, rendondoli particolarmente adatti per applicazioni come LED e monitor.

Tuttavia la legislazione europea non permette l'uso di grandi quantita di Cd nei dispositivi elettronici. Pertanto, per implementare i QDs nel mercato dell'elettronica è necessario sostituire i QDs a base di Cd con materiali non tossici, possibilmente con proprietà ottiche dello stesso livello.

A tal proposito, lo sviluppo di QDs del gruppo III-V e specialmente quelli a base di InP (ovvero con un '*core*' di InP), hanno attirato molta attenzione negli ultimi anni. Infatti, i nanocristalli colloidali di InP, se passivati con un rivestimento ('*shell')* di materiale opportuno, presentano una buona stabilità chimica e una discreta efficienza quantica, con un emissione che può essere variata nello spettro del visibile. Oggigiorno, sospensioni di QDs di InP con una oppurtuna *shell* di passivazione, possono essere preparati con sintesi chimiche che possono essere estese a livello industriale. È quindi di particolare importanza investigare le proprietà ottiche e la relativa struttura dei livelli energetici di questa promettente classe di nanocristalli. Le proprietà optoelettroniche di tali QDs sono determinate dalla natura chimica sia del *core* che della *shell*, dalla tensione della struttura del *core* indotta dalla crescita della *shell* e dal relativo offset tra la banda di conduzione e la banda di valenza del *core* e della *shell*. L'elettrone e la lacuna possono essere entrambi localizzati all'interno del *core* oppure una carica può essere localizzata nel *core* e l'altra nella *shell*. Pertanto la natura della *shell* ha una forte influenza nei processi di emissione luminosa.

Questa tesi si prefigge di investigare questi aspetti in dettaglio, fornendo un'analisi dei fondamentali processi fisici alla base dell'emissione luminosa spontanea. In particolare focalizzandoci sulla struttura fine dei livelli eccitonici nei nanocristalli di InP e studiando come la ricombinazione eccitonica dipenda dalla taglia dei nanocristalli, dalla composizione della *shell* e dalla struttura *core/shell*.

La spettroscopia ottica ad alti campi magnetici e basse temperature è un metodo molto efficace per studiare in detaglio la struttura fine eccitonica. Gli alti campi megnetici sono infatti essenziali per ottenere un considerevole *Zeeman splitting* degli stati degeneri in spin. In questo studio sono state utilizzate tecniche di spettroscopia di fotoluminescenza, studiando la polarizzazione e l'emissione luminosa risolta in tempo, al fine di caratterizzare gli stati della struttura fine eccitonica e la loro interazione con i fononi del reticolo cristallino, sia del *core* che della *shell*.

La struttura fine eccitonica dei QDs di InP/ZnSe (*core/shell*) è presentata nel **capitolo 3**. La fotoluminescenza (PL) risolta in tempo, analizzata a temperature variabili da 10 mK a 300 K, rivela che lo stato eccitonico più basso in energia è un '*dark state*' e il nome sta a indicare che l'emissione spontanea da questo stato è proibita in approssimazione di dipolo elettrico. Uno stato '*bright*' (con ricombinazione permessa in tale approssimazione) è situato a un'energia di circa 4-7 meV dallo stato *dark* e la distanza in energia tra gli stati *dark* e *bright* aumenta con la riduzione delle dimensioni del '*core*' dei QDs. La spettroscopia Raman associata a una tecnica spettroscopica chiamata '*fluorescence line-narrowing (FLN)*', utilizzate a temperature di 4 K e a diversi campi magnetici variabili fino a 30 T, dimostra che la ricombinazione radiativa dallo stato eccitonico piu basso, coinvolge fononi acustici e ottici, sia del InP (*core*) che del ZnSe (*shell*). Inoltre, dimostriamo che il picco a più alta intensità negli spetri FLN è una replica dovuta all'emissione dallo stato *dark* associata a fononi acustici. Ciò è in netto contrasto con gli spettri FLN dei QDs di CdSe, dove è stata osservata una maggiore emissione diretta dello stato *dark*.

L'effetto di una diversa *shell* sulla struttura fine eccitonica e la dinamica degli spin associata al processo di ricombinazione è presentata nel **capitolo 4,** dove viene riportato uno studio dettagliato delle proprietà ottiche dei QDs di InP con una shell di ZnS, studiati ad alti campi magnetici fino a 30 T e alla temperatura di 4 K. Anche in questo caso, lo stato eccitonico a piu bassa energia è uno stato *dark* la cui ricombinazione avviene quasi esclusivamente con processi assistiti da fononi. Gli spettri FLN e l'analisi del decadimento di fotoluminescenza dimostrano che non vi è mix tra il piu basso stato *dark* e quello *bright* più vicino. Il tempo di decadimento della fotoluminescenza persino aumenta con l'aumentare del campo magnetico. Ciò è stato osservato in tutti i QDs a base di InP analizzati, indipendentemente dalla loro *shell*. Inoltre, lo studio della polarizzazione circolare dello stato *dark* rivela un tempo di rilassamento di spin molto lento e una saturazione del grado di polarizzazione circolare (*degree of circular polarization*) intorno al 16%. Questi risultati mostrano ancora un marcato contrasto con i QDs di CdSe e altri nanocristalli colloidali.

Il ruolo giocato dalla struttura *core/shell* nella dinamica di ricombinazione dell'eccitone nei QDs a base di InP è presentato nel **capitolo 5**, dove viene mostrato come l'interazione eccitone-fonone sia influenzata dalle diverse *shell* analizzate: ZnS, ZnSe e (Zn,Cd)Se con diverse quantità di Cd (5%, 9%, 12%). Confrontando le energie fononiche estratte dalle misure di spettroscopia Raman con i picchi di emissione eccitonica osservati negli spettri FLN, abbiamo determinato sia l'energia dello stato *bright* $\mathrm{F} = \pm 1$, sia quella del più basso stato *dark* $\mathrm{F} = \pm 2$, per tutte le diverse strutture *core/shell* analizzate. I modi fononici coinvolti nella ricombinazione radiativa dello stato *dark* sono sia acustici che ottici e l'interazione eccitone-fonone favorisce il decadimento radiativo da tale stato. Il grado di interazione eccitone-fonone dipende dal materiale della *shell:* per esempio, la delocalizzazione della funzione d'onda elettronica nella *shell* aumenta la polarizzabilità eccitonica, rafforzando l'interazione con i fononi polari attraverso l'interazione di Fröhlich.

Nel **capitolo 6**, la struttura fine eccitonica è stata studiata in modo più dettagliato in relazione alla delocalizzazione della funzione d'onda elettronica nella *shell*, usando *shell* di ZnSe e di (Zn, Cd)Se con il 5 e il 9% di Cd. L'introduzione di Cd nella *shell* di ZnSe diminuisce il *band gap* di quest'ultima, riducendo quindi l'offset nella banda di conduzione del sistema *core/shell*, con conseguente aumento della delocalizzazione della funzione d'onda elettronica nella *shell* all'aumentare del contenuto di Cd. Si noti che la funzione d'onda della lacuna rimane localizzata nel *core*. Utilizzando la spettroscopia FLN in campi magnetici esterni fino a 30 T, possiamo osservare la rimozione della degenerazione del livello $\mathrm{F} = \pm 1$ che si divide in $\mathrm{F} = +1$ e $\mathrm{F} = -1$. Si osserva inoltre anche il livello $\mathrm{F} = 0$, che non era mai stato osservato in precedenza. Anche in questo caso lo stato di struttura fine eccitonico ad enegia piu bassa è uno stato *dark* con $\mathrm{F} = \pm 2$, da cui l'emissione radiativa è favorita dall'interazione eccitonica con fononi acustici e ottici. La struttura fine dell'eccitone rimane pressoché invariata con l'incorporazione di quantità di Cd tra lo 0 e il 9%, nella *shell* di ZnSe, probabilmente a causa di un ruolo dominante della lacuna nel determinare la struttura fine eccitonica.

In conclusione, è stato mostrato che la dinamica eccitonica nei QDs a base di InP si differenzia sostanzialmente da quella dei nanocristalli del gruppo II-VI. Tutti i sistemi *core/shell* analizzati hanno uno stato *dark* $\mathrm{F} = \pm 2$ come stato più basso della struttura fine. Da questo stato, la ricombinazione radiativa diretta è proibita in approssimazione di dipolo elettrico. La lenta ricombinazione osservata da questo stato *dark* è quasi esclusivamente dovuta a processi assistiti da fononi acustici e ottici. Il grado di interazione eccitone-fonone dipende dal materiale delle *shell* e al conseguente diverso grado di polarizzabilità che l'eccitone puo assumere. Inoltre è stata osservata l'emissione da un livello *bright* $\mathrm{F} = 0$, un processo che fino ad ora era stato trascurato. È stato osservato anche che i QDs a base di InP mostrano una completa assenza di mix indotto dal campo magnetico tra gli stati *bright* e quelli *dark*. Queste notevoli caratteristiche saranno studiate più approfonditamente in ricerche future.

Publications and conference contributions

This thesis is based on the following publications:

- Chapter 3
  Annalisa Brodu, Mariana V. Ballottin, Jonathan Buhot, Elleke J. van Harten, Dorian Dupont, Andrea La Porta, P. Tim Prins, Mickael D. Tessier, Marijn A. M. Versteegh, Val Zwiller, Sara Bals, Zeger Hens, Freddy T. Rabouw, Peter C. M. Christianen, Celso de Mello Donega, and Daniel Vanmaekelbergh. "*Exciton Fine Structure and Lattice Dynamics in InP/ZnSe Core/Shell Quantum Dots*". ACS Photonics, 2018, 5 (8), (pp. 3353–3362).

- Chapter 4
  Annalisa Brodu, Mickael D. Tessier Damien Canneson, Dorian Dupont, Mariana V. Ballottin, Peter C. M. Christianen, Celso de Mello Donega, Zeger Hens, Dmitri R. Yakovlev, Manfred Bayer, Daniel Vanmaekelbergh, and Louis Biadala. "*Hyperfine interactions and slow spin dynamics in InP-based core/shell colloidal nanocrystals*". Under review.

- Chapter 5
  Annalisa Brodu, Mariana V. Ballottin, Jonathan Buhot, Dorian Dupont, Mickael D. Tessier, Zeger Hens, Freddy T. Rabouw, Peter C. M. Christianen, Celso de Mello Donega, and Daniel Vanmaekelbergh. "*Exciton-phonon coupling in InP quantum dots with ZnS and (Zn,Cd)Se shells*". Submitted.

- Chapter 6
  Annalisa Brodu, Jonathan Buhot, Mariana V. Ballottin, Marion Severijnen, Dorian Dupont, Zeger Hens, Freddy T. Rabouw, Peter C. M. Christianen, Celso de Mello Donega, and Daniel Vanmaekelbergh. "*Exciton fine structure of InP/(Zn,Cd)Se core/shell quantum dots*". In preparation.

Other publications:

- Annalisa Brodu*, Vigneshwaran Chandrasekaran* (*equal contribution), Lorenzo Scarpelli, Jonathan Buhot, Francesco Masia, Mariana V. Ballottin, Marion Severijnen, Mickael Tessier, Dorian Dupont, Freddy Rabouw, Peter C. M. Christianen, Celso de Mello Donega, Daniël Vanmaekelbergh, Wolfgang Langbein, Zeger Hens. "*Fine Structure of Nearly Isotropic Bright Excitons in InP/ZnSe Colloidal Quantum Dots*". Submitted.

- Claudiu M. Iaru, Annalisa Brodu, Niels J.J. van Hoof, Stan ter Huurne, Jonathan Buhot, Federico Montanarella, Sophia Buhbut, Peter C. M. Christianen, Celso de Mello Donega, Paul M. Koenraad, Daniël Vanmaekelbergh, Andrei Y. Silov. *"Carrier trapping enhances Fröhlich interaction in lead halide perovskites"*. In preparation.

The work discussed in this thesis was presented at the following international conferences:

- DPG 2017 – Germany. "Magneto-optical study to reveal the exciton fine structure in InP/ZnSe core/shell quantum dots". (Poster)

- Nanax 2017 – Portugal. "Exciton Fine structure in InP/ZnSe core/shell quantum dots". (Oral presentation)

- NanoGe Fall Meeting 2018 – Spain. "Exciton fine-structure of InP/Cd,Zn,S,Se core/shell QDs bright and dark states and the role of phonons". (Poster) *Best poster prize, awarded by Nanomaterials* - travel grant

- Physics@Veldhoven 2019 – The Netherlands. "Role of phonons in exciton recombination for InP QDs and the effect of shells". (Poster)

About the author

Annalisa Brodu was born in Iglesias, a small city in the south of Sardinia (Italy) where she studied at the scientific high school G. Asproni.

After obtaining her BSc in physics (2010) in the Photonics and Optoelectronics Lab group at the University of Cagliari (Italy), she worked for three years as teaching assistant. During that time she supervised physics courses for students of Chemical, Biomedical, Electronic, Environmental and Civil Engineering at the University of Cagliari.

She obtained her MSc in physics (cum laude) from Univertita'degli studi di Cagliari, in 2014. During her master, Annalisa performed an Erasmus Placement at the Integrated Center for Applied Physics and Photonic Materials (IAPP) at TU Dresden (Germany), where she worked on the investigations of ultra-thin metal blend films as cost-efficient transparent electrodes for organic photovoltaic devices.

In 2015 she started a PhD in the group of Condensed Matter and Interface at the Debye Institute for Nanomaterials Science at Utrecht University (The Netherlands), where she worked on optical spectroscopic studies of InP based quantum dots. Most of the results achieved are reported in this thesis. She has collaborated with a number of different research groups and presented her work at several universities as well as international conferences.

Outside the lab, in her spare time, she likes to meet with friends, travel, play sports and dance. She had a long career at scouting and she likes to be involved in voluntary projects.

Acknowledgements

I would like to conclude my thesis thanking all the people who helped and supported me during my PhD time in Utrecht. All of you had a fundamental role, allowing me to accomplish this work and to grow personally and professionally.

At first, my thoughts go out to my supervisors; thanks for trusting me and giving me the opportunity to work on this great project.

I would like to start by thanking **Daniel** for the kind guidance with constant availability for scientific discussion and any type of advice. Your broad knowledge has always been a great source of inspiration for me. Besides the scientific interaction, I profoundly appreciate your care at the human level, and I will definitely keep very good memories of the enjoyable time during the friendly lunch meetings at the department and conferences. I'm really grateful for having you as a supervisor!

Celso, it was a great pleasure to work with you, thanks a lot for your generous support and guidance, for your patience in answering all my infinite questions and kindness to explain everything in detail. Your strong expertise and deep knowledge in the field have always been extremely valuable and useful. I strongly appreciate the way you motivated me scientifically and personally. You kindly supported and encouraged me to improve myself in taking more risk, going outside of my comfort zone and to handle challenging times with patience. Thanks!

Zeger, thanks for hosting me in your lab during my secondments where I had the chance to learn the synthesis protocol of InP-based colloidal quantum dots. Thanks also for the great lead of the 'Phonsi' program and for taking care of the projects and collaborations. I admire your scientific contributions and I'm very grateful for all your input in our collaborations.

Dear **Peter**, you have always been a perfect supervisor and mentor for me, even though this has never been official. I'm deeply grateful to you for making space for me in your lab at the Radboud University, regularly welcoming me there and kindly introducing me to the world of high magnetic fields. Our meetings help me enormously in developing this work. I feel really honoured that I had the chance to work and interact with you.

Freddy, my former colleague and unofficial 5th supervisor, you have always been incredibly kind and generous. Thank you so much for all the time you patiently spent with me sharing your profound knowledge and *helping* me any time I needed. You gave a fundamental contribution to this work with your exceptional competences and adorable work attitude. Surely, I will warmly hold the memories of our 'bonding' social activity and the kind and supporting hugs. You definitely earned all my gratitude and sincere friendship.

Thanks also to all the other professors at CMI for the nice scientific discussions and their availability. Thanks to **Harold**, **Andries**, **Ingmar** and **John**.

The work presented in this thesis is mainly based on the measurements performed at the HMFL (High Field Magnet Laboratory) at the Radboud University, where several people contributed to the results. A special thanks goes to **Mariana**, it was very nice to start the measurements at HFML together and it has been a real pleasure to collaborate with you, sharing the good and bad moments during the long days and nights of measurements. I really appreciate your care and dedication at work and in daily life. You have been not only a good and reliable collaborator but also a good friend and I will always remember our nice social activities and the amazing bike trip around the Netherlands! **Marion,** you joined in the measurement team just during my last measurement time, but that time was sufficient to appreciate you scientifically and personally, and I'm particularly grateful for the moral support you gave me! I want to also thank **Anatol** and **Jonathan**, for the valuable assistance in the lab during my measurements at HFML and for sharing your deep knowledge on the subject. And, of course, I will not forget the precious technical support of **Peter A.**, thanks for being always available for any technical needs in the lab, with your positive and friendly attitude! A sincere thanks to all the other colleagues and technicians that made my stay at HFML a very great experience!

Besides the strong collaboration at HFML, during my PhD I had the opportunity to collaborate with several other groups and there are several people that I would like to thank. **Mickael T**. I appreciated your caring during my secondment at Gent University, where you taught me how to synthesize InP-based quantum dots with the protocol you have developed. **Dorian** and **Elleke** thanks a lot for providing very high-quality QDs samples that have been essential for this work. **Sara Bals** and **Andrea**, many thank you for the structural and chemical characterization that you performed on the InP-based samples. The images you were able to achieve are amazing! **Val** and **Marijn**, thanks a lot for hosting me in your group at KTH in Stockholm, it was a great experience, I'm really grateful you gave me the opportunity to work with such a high-tech facility, being able to measure at so low temperatures! Thanks also to all the other friendly colleagues I met during the collaboration, you made my stay at KTH really enjoyable! **Louis**, thanks a lot for the measurements you performed in your lab in Dortmund and for all the work you did for our collaboration! Additionally, I want to thank **Claudiu** and **Sophia** for the nice collaborations on perovskite! It was very nice to work also on such a different but extremely interesting topic!

During my PhD I had great support from the people in my group at CMI. At first, a very special thanks goes to **Tim P.**, the 'perfect' officemate, also when you try to annoy or bully me! …but, you know, I always enjoyed your jokes in the office, and the very inspiring scientific discussions! It was a great pleasure to work and share the office with you. Many thanks also for your warm care and your precious encouragements during the hard times**.** You are an awesome person and I'm so happy to have you as *paranimf!* **Christiaan** and **Saoirsé** definitely completed the 'perfect' office! I'm really grateful for the great time we spent together and for the support you were always able to give me! I'm so glad I was

part of 'The most stylish office'! ;) **Federico**, it was a real pleasure to start together this adventure, sharing so many activities, conferences, travels and lunch breaks! Thanks a lot for the nice time and for all the suggestions you always gave me! **Chenghui**, you have been a lovely colleague, many thanks for the nice chats in the working evenings, and for your natural kindness! **Winston,** it was a real pleasure to be your *paranimph!* Another special thanks goes to **Bas**, my assistant *paranimph*, that helps me a lot in the organization of Winston defence! :) **Marlou** thanks for all the positive and smiling interactions, you are great! **Naud,** thank you so much for the Sardinia flag, the perfect way to support me at the end of my PhD! **Kelly** and **Alicia** many thanks for the nice time spent together at CMI, around Utrecht and Spain! I am sincerely happy I shared part of my PhD path with you! ;)

Another important acknowledgement goes to the supporting staff, former and current: **Hans**, **Peter**, **Stephan** and **Linda** thanks a lot for being always available and ready to help! And to all the other group members and former colleagues I have been working with during my PhD project: **Maaike**, **Annelies**, **Anne**, **Jette**, **Giuseppe**, **Liudmyla**, **Vasilii**, **Markus**, **Jesper**, **Thomas G.**, **Christa**, **Serena**, **Maryam**, **Ward**, **Jaco**, **Joep**, **Pascal**, **Thomas v.S.**, **Joost**, **Mathijs**, **Pedro**, **Peter J.**, **Pierre**, **Jacobine**, **Tim S.**, **Robin**, **Pradip**, **Nadine**, **Allan**, **Dechao**, **Rouhollah**, **Atul**, **Wenjin**, **Sergiu**, **Sebastian**, **Zachar** and all the students, thank you for all the good time spent together!

I cannot forget the people from soft condensed matter (SCM): **Giulia**, **Guido**, **Tonnishtha**, **Chris**, **Douglas, Zdenek, John**, **Ernest**, **Rama**, **Naveed**, **Nik**, **Carmine**, **Simone**, **Massimiliano**, **Gabriele**, **Nik**, **Pepijn**, **Wiebke**, **Jessi**, **Anna** and all the other members of SCM, thanks for the enjoyable activities organized together! And again from Ornsteinlaboratorium, many thanks to **Alessandro G.** for the funny and relaxing coffee breaks.

My PhD project was part of 'Phonsi', a Marie-Curie research and training program that combines universities, research institutes, companies and start-ups, forming a network full of strong interactions and collaborations. It was great to be part of such an interesting consortium! At first, I want to thank all the PI, members and organizers for the inspiring and motivating conferences and workshops. Every time it was a real pleasure to meet all of you, share our researches and being inspired by the scientific discussion and workshop activities. But not only, the time spent with all the other PhD students of the network, travelling and socializing before, during or after the 'Phonsi' meetings, was unforgettable! It was a great pleasure to share with all of you this amazing experience, thanks to **Niall**, **Lukas**, **Renu**, **Nayyera**, **Michael**, **Darius**, **Bogdan**, **Adam**, **Johanna**, **Ronan**, **Ye**, **Maryam** and **Federico**. And a special thanks to **Vignesh**, for your kindness and availability in our collaboration.

Outside the work environment, there are several friends that I would like to thank for their support and for making these years truly memorable.

The most important thanks goes to **Trusanne**, **Damaris** and **Viviana.** I don't have words to say how special you all are for me. I feel very lucky to have met you. The precious time spent all together travelling, socializing and sharing our daily life, has and will always have a place in my heart. I'm truly looking forward to our new adventures together, wishing to our friendship a long time to come! Here I don't have enough space to list everything I'm grateful for, but I would like to shortly thank each one of you personally. **Trusanne,** I'm really grateful for all your care, availability and support! Thanks a lot also for the big help in the defence organization and the amazing graphic of this thesis! You are a great person, and I'm proud to have you as *paranimf!* **Damaris**, thanks so much for all the very inspiring chats, your inestimable support, suggestions and help! Thanks also for hosting me during your stay in Paris, I really enjoyed to share that amazing time with you! I truly admire you, thanks for who you are! Last but not least, **Viviana**! I met you at the beginning of my PhD, and since then, we shared so many memorable activities and adventures together! Impossible to forget the salsa parties, the nice and relaxing days at the SPA and the supporting lunch and dinner during our thesis time! You have always been so kind, welcoming and reliable! I cannot imagine my PhD path without you! You are special, thanks a lot for everything!

Another important thought goes to my awesome 'InterNations group'. **Sergio**, **Leoni**, **Jacko** and **Essie**, thanks a lot for sharing so many great activities and making my stay in Utrecht really enjoyable! **Timon**, so many memories… thanks for the 'gezellig' time spent together, I always enjoyed our relaxing time watching movies and playing cards. You have always been very kind and willing to cheer me up with your warm hugs! Thanks for all your care! My neighbours: **Ingmar**, **Immy** and **Mitchel**, thanks for all the nice board game nights, those times were so enjoyable and funny! A big thanks to all the people from the **capoeira group**, even if I didn't join you regularly, every time I stopped by there, you always welcomed me with your contagious energy and happiness! **Francesca S.**, it was very nice to get in touch again after you moved to Rotterdam! It is always great to have an old friend around, thanks a lot for your closeness and contagious joy! And to the new entries in my path: **Hulya**, **Thomas**, **Andreas**, **Pradeep**, **Laura**, **Dimitris**, **Laurent**, **Giordano** e **Francesca** and all the other new friends to get to know better, thanks for making my life so rich and interesting!

The memories of the great time during my research project at IAPP motivated me enormously to start a new adventure abroad, this time here in Utrecht. Thanks so much **Sven**, **Sylvio**, **Ji-ling**, **Max**, **Lars** and all the other friends I meet at IAPP and in Dresden. I really enjoyed our lovely reunions here, in Belgium or in Germany! Including with the new-entry **Bernhard,** I met you at the DPG conference after I left IAPP, but I felt like I have known you for ages (maybe because the cute **Sven** already told me so much about you at that time!). Thank you all for the great time spent together!

All my friends from Sardinia, some of who now spread around Europe. A special thanks to **Antonio S.**, for the strong scientific and moral support. All the people I love to meet as soon as I'm back: **Nico**, **Carla**, **Roby**, **Olivier** (previously adopted from Sardinia), **Giammi**, **Carlo**, **Francesca**, **Roby M.**, **Marta** (with the new entry that I cannot wait to meet!), **Gianmarco**, **Giovanni**, **Alessandro**, **Valerio**, **Nicola S.**, **Davide**, **Laura**, **Stefano** and all the other friends from Sardinia! You have always been ready to meet up when I was back, and to make me feel welcome home or in your new country! A warm thank you also to **Daniele P.** for the long distance phone calls, very supporting and inspiring!

Finally, I would like to thank **my parents** and **my sister**, despite the physical distance of living in different countries, you all were able to show me your endless love. I'm deeply grateful for your patience, support and for everything you did for me. Thank you with all of my heart!

Annalisa